Material Characterization Report of EBR II Mark IV Fuel Element

INL/RPT-25-88203 rev.1

Originally for INL CRADA 11CR19

OCTOBER 2025

Cynthia Papesch,
Karen Wright,
Leah Squires,
Tammy Trowbridge,
Jameson Root,
Benjamin Cowan, and
Douglas Porter

Idaho National Laboratory

Thomas Hartmann

University of Nevada, Las Vegas

Bruce Hilton

TerraPower

Idaho National Laboratory

Battelle Energy Alliance manages INL for the U.S. Department of Energy's Office of Nuclear Energy

INL/RPT-25-88203

Material Characterization Report of EBR II Mark IV Fuel Element

Cynthia Papesch,
Karen Wright,
Leah Squires,
Tammy Trowbridge,
Jameson Root,
Benjamin Cowan, and
Douglas Porter
Idaho National Laboratory

Thomas Hartmann
University of Nevada, Las Vegas

Bruce Hilton
TerraPower

October 2025

Idaho National Laboratory
Idaho Falls, Idaho 83415

http://www.inl.gov

Work funded by TerraPower, LLC under CRADA 11-CR-19

Prepared for the
U.S. Department of Energy
Office of Nuclear Energy
Under DOE Idaho Operations Office
Contract DE-AC07-05ID14517

Page intentionally left blank

CONTENTS

FIGURES

TABLES

Page intentionally left blank

ACRONYMS

3D	three dimensional
AAF	average area fraction
BSE	backscatter election
CI	confidence interval
CT	center
EBR-II	Experimental Breeder Reactor II
EBSD	electron backscatter diffraction
EDS	energy dispersive x-ray spectroscopy
EPMA	electron probe microanalyzer
HAZ	heat-affected zone
ID	internal diameter
OD	outer diameter
SD	standard deviation
SEM	scanning electron microscope
XRD	x-ray diffraction

Page intentionally left blank

Material Characterization Report of EBR II Mark IV Fuel Element

1. INTRODUCTION

Idaho National Laboratory has established a collaboration with TerraPower LLC to perform material characterization testing on as-built unirradiated sodium-bonded metallic fuel elements as part of Cooperative Research and Development Agreement No. 11-CR-19. The data collected from this effort will contribute to a baseline characterization study of this fuel element type for comparison with the results of irradiation experiments guided by TerraPower's business development plans and funding. Funding for this work provided by TerraPower,

The focus of this report is the characterization of an unirradiated as-built fuel element from the Experimental Breeder Reactor II (EBR-II) Mark IV driver fuel design. The fuel in this element is a metallic uranium-zirconium alloy, and the cladding material is HT9 stainless steel. Both the metallic fuel and cladding materials are characterized, including chemical composition, grain size, morphology, phase composition, precipitate composition, crystallography, density, and hardness.

2. AS-BUILT FUEL ELEMENT DESCRIPTION

The fuel element used in this study is from the EBR-II Mark IV driver fuel qualification experiment number, X448, element number, G242. This as-built fuel element consists of a welded HT9 cladding tube approximately 29 inches long, containing a single fuel slug, approximately 13.5 inches long, of U-10Zr (wt%) metallic fuel with approximately 1.8 grams of Na used to bond the fuel to the inside of the cladding tube.Casting of U-10Zr for Mark IV fuels occurred in a controlled atmosphere location. Zirconium was loaded into the bottom of a graphite crucible while uranium was laid over the top of the zirconium. The reason for this approach was to allow the lower melting temperature metal (U) to melt and flow over the higher melting temperature metal (Zr), thus promoting melting. In some batches, the heel remaining from previous castings was incorporated to reduce the amount of waste produced (Wilkes et al., 1987). The melt material in the crucible was heated with a copper induction bar to 1530°C (Wilkes et al., 1987). Closed-end molds of quartz (Tm = 1667°C) were coated with a zirconia-alcohol slurry and dried (Wilkes et al., 1987). The furnace atmosphere was evacuated, and the molds were lowered into the melt. Argon gas was then used to repressurize the furnace, thus forcing the melt into the molds. The molds were quickly removed from the melt. Then the furnace was cooled to 300°C before the molds were removed from the furnace. Upon removal from the furnace, the molds were broken to remove the cast slugs and (Burkes et al., 2009). A cast fuel slug was placed into an HT9 tube and sealed at one end where the sodium had been added. The tube (cladding) was heated to melt the sodium to allow the fuel slug to settle into the molten sodium. After sealing the other end of the tube, the complete fuel pin was then impact bonded at a temperature high enough (~500°C) to allow the sodium to wet both the outer surface of the fuel slug and inner surface of the cladding.

3. ELEMENT SAMPLING METHOD

Fuel samples composed of U-10Zr were obtained from a Na-bonded fuel pin built for EBR-II. The 13.5 inch fuel slug was de-bonded from its cladding (sodium removed) prior to cutting the fuel slug into three sections for sampling. Sample "Ra" was obtained approximately 1 inch from the spade (lower end plug) end, while samples "Rb" and "Rc" were obtained approximately 7.125 and 13.25 inches from the spade end, respectively. Table 1 gives the specific range of measurements.

Note that the as-cast slugs were never marked before loading into the cladding as to the relative position in the quartz mold when casting. This is important because, although the quartz mold was coated with a ZrO_2 slurry and dried prior to casting, the interaction with the mold appears, in this study, to be greatest near one end. We theorized that this interaction was caused by being at the end closest to the melt. At that location, it would be at an elevated temperature longer than at the end furthest from the melt.

Each sample removed from the rod was sectioned into multiple pieces, a transverse section and a longitudinal section for phase and microstructure characterization and other sizes for chemical analysis. Longitudinal and transverse sections of each sample were mounted in epoxy (Figure 1) and polished to the finishes necessary for each of the performed tests. These sample preparation methods are described in each of the respective sections of this report.

Table 1. Sample locations for fuel and cladding from the EBR-II fuel element.

Region of Interest	Location from the Spade End of Element
Ra (fuel)	1/4 in. to 1 in.
Rb (fuel)	6-3/8 in. to 7-1/8 in.
Rc (fuel)	12-1/2 in. to 13-1/4 in.
Fuel (cladding)	6-3/8 in. to 7-1/8 in.
Plenum (cladding)	21-5/16 in. to 22-1/16 in.
TOP (top end weld)	36 in.
SPD (spade end weld)	0 in.

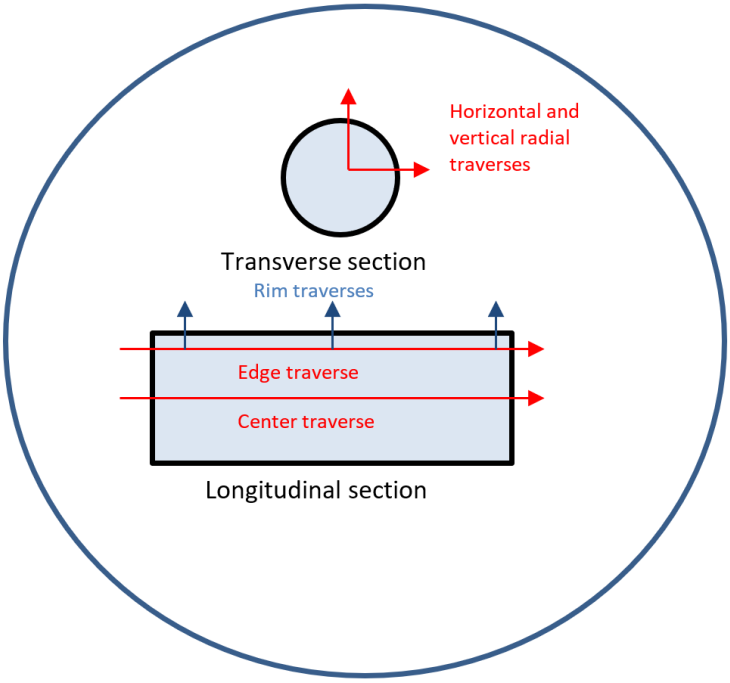

Figure 1. Schematic showing geometry of samples mounted into the metallography mount. 'Traverse' lines relate to the X-ray determined phase analyses.

Cladding samples were also sectioned and mounted in epoxy in a similar fashion to the fuel samples. See Table 1 for the locations and sample internal diameters (IDs) of the cladding samples.

4. FUEL SLUG PHYSICAL PROPERTIES

4.1. Dimensions

The total mass of the as-built element (including fuel, sodium, and HT9 cladding components) was 130.79 grams, including the spacer wire wrap. Table 2 gives the physical dimensions of the fuel slug (without cladding) used in documentation of the G242 fuel element fabrication. This fuel slug came from casting batch number, MKIV IC001.

Table 2. Physical dimensions and density of Fuel Slug 69 from Fuel Element G242.

Fuel Slug ID	Length (in.)	Avg. Dia. (in.)	Max. Dia. (in.)	Min. Dia. (in.)	Volume (cc)	Mass (g)	Density (g/cc)
69	13.502	0.1690	0.1708	0.1656	4.963	77.31	15.58

4.2. Chemical Composition

4.2.1. U-10Zr Fuel

The chemical composition of the casting batch was determined at the time of fuel slug casting by inductively coupled plasma-atomic emission spectroscopy and thermal ionization mass spectroscopy. A sample slug was randomly selected from the casting batch of ~100 slugs, and top, center, and bottom segments were sheared from the sample slug. These segments were dissolved and analyzed. The resulting chemical composition is given in Table 3.

Table 3. Chemical and isotopic composition of a sample slug from the casting batch MKIV-IC001.

Chemical Composition (wt%)			
	Top	Center	Bottom
U	90.12	90.7	90.35
Zr	9.83	9.5	9.78
C	0.0366	0.0194	0.0086
Fe	0.0081	0.0091	0.01
N	0.001	0.001	0.001
O	0.0024	0.0021	0.0026
Y	0.0019	0.0021	0.0019
Si	0.0097	0.0089	0.0099
Ta	0.0014	0.0018	0.0018
Isotopic Composition (percent of total U)			
U-234	0.7550	0.7580	0.7600
U-235	69.56	69.56	69.65
U-236	0.3340	0.3330	0.3330
U-238	29.35	29.36	29.36

The chemical composition of Fuel Slug 69 from Fuel Element G242 was measured during this current study using inductively coupled plasma mass spectroscopy. The resulting chemical and isotopic composition is given in Table 4. These results come from only one fuel slug taken from the batch given in Table 2. Samples for analysis were taken at 95%, 50% and 5% of the total length of the fuel slug, starting at the end of the slug closest to the spade end of the fuel element, labeled top, center, and bottom in Table 4, respectively. Reminder that this does not necessarily reflect the orientation of the casting. Two samples were taken from each of the three locations, and the average value is reported.

Table 4. Chemical and isotopic composition of Fuel Slug 69 from Fuel Element G242.

Chemical Composition (wt%)			
	Top	Center	Bottom
U	91.35	91.25	89.8
Zr	9.79	9.58	10.35
Y	0.0022	0.0022	0.0031

Chemical Composition (wt%)			
	Top	Center	Bottom
Ni	0.0028	0.0029	0.0029
Nb	0.00005	0.00005	0.00008
Cd	0.00002	0.00002	0.00013
Hf	0.0007	0.0006	0.0009
W	0.0025	0.0025	0.0025
Cr	0.0007	0.0008	0.0006
Al	0.0054	0.0127	0.0077
Fe	0.0238	0.0077	0.0206
Si	0.0131	0.0205	0.076
Isotopic Composition (percent of total U)			
U-234	0.7725	0.776	0.7765
U-235	69.65	69.7	69.75
U-236	0.3395	0.337	0.341
U-238	29.2	29.15	29.1

4.2.2. HT9 Cladding Chemistry

A certification of chemical composition for the HT9 cladding for this batch of material was recovered from archived data (Table 5). The chemical composition of the HT9 was not measured again as part of this study.

Table 5. Chemistry for Mk-V HT9 cladding.

Element	C	Mn	Si	P	S	Cr	Ni	Mo	Cu	Co	Ti	Nb	Ta	W	Al
Composition, ppm	0.21	0.63	0.29	0.013	0.002	11.90	0.56	1.09	0.03	0.02	<.01	<.01	<.01	0.05	<.01

4.2.3. U-10Zr Fuel Density

Density was measured at the ambient temperature using the Archimedes method for water displacement for both the U-10Zr fuel slug and the cladding tube. Multiple fuel samples were collected from the fuel pin at locations corresponding to 95%, 50%, and 5% of the length of the fuel pin with the spade end being the bottom. The calculated results and summary statistics are given in Table 6. Note that the theoretical density should be ~16.2 g/mL^3 by simple 'Rule of Mixtures'. Porter has proposed that casting defects are the major reason for the reduced density in the cast product[a] Table 6 shows the results of the fuel density measurements. Cladding samples were also collected and their densities measured. The results are presented later in this report in the HT9 section (6.0).

[a] Journal article in draft.

Table 6. Room temperature density of the U-10Zr fuel slug.

Sample ID	Density (g/mL^3)
Ra1 Rod End	16.1647
Ra	15.6967
Rb	15.5182
Rb1 Rod End	15.5459
Rc	15.7851
Rc1 A Rod End	15.5569
Rc1 B Rod End	15.6112
Average	15.7000
Standard Deviation (SD)	0.2270
95% Confidence Interval (CI)	0.2100

4.2.4. U-10Zr Fuel Hardness

Ten Vicker's hardness tests were performed on each of the three fuel samples using a LECO microhardness tester across the transverse sample at 250 μm intervals with a 100 g load. Table 7 shows the average hardness values as well as the relevant statistics. Measurements were consistent throughout the samples with the exception of the Rb sample. During the examination of Rb, two data points were measured that were discarded because they were located too close to a void (119) and a precipitate (539). These points were not included in the summary statistics.

Table 7. Microhardness data on U-10Zr fuel samples.

	Ra2	Rb2	Rc2
Hardness Values	404	119	429
	415	367	426
	436	400	433
	424	404	422
	417	409	407
	424	411	392
	445	415	409
	427	422	420
	394	429	436
	409	539	413
Average	419	407	419
SD	15.1	18.7	13.5
95% CI	10.8	15.6	9.7

4.3. Fuel Phase Composition (XRD)

Phase composition was determined using x-ray diffraction (XRD) methods. The XRD sample analysis for the EBR-II fuel samples was performed on a Bruker D8 Discover x-ray diffractometer equipped with microfocus capabilities. Bulk analysis data was acquired from each specimen using a 300 μm microfocus snout and obtaining data from six locations on each transverse specimen and eight locations on each longitudinal specimen from 20° to 90° 2-

theta at a scan rate of 2 sec/step. The data from all locations on each sample was then compiled and analyzed as bulk. This method of bulk analysis was necessary due to the relative position of the longitudinal and transverse specimens mounted in the metallography mount. Microfocus analysis was performed using a 50 μm microfocus snout, and data was obtained at 150 μm steps on the transverse samples and 350 μm steps on the longitudinal samples from 35° to 90° 2-theta at a scan rate of 2 sec/step. During the microfocus analysis, the samples were oriented as shown in Figure 2 except for the cross section of Scan B, where the sample was analyzed at a 90° degree angle to the orientation shown. The purpose of the orientation was to limit beam broadening effects to within the line of analysis. Scan A for each sample was a cross-section analysis of the transverse specimen from bottom to top at 150 μm steps, and Scan B was a cross-section analysis of the transverse specimen from left to right at 150 μm steps (in the orientation shown in Figure 2). Scan C was a cross section of the left-most edge of the longitudinal specimen from bottom to top at 350 μm steps. However, in all cases the data obtained from Scan C was impossible to interpret due to noise interference, which was attributed to obtaining the data too close to the edge of the sample, allowing part of the x-ray beam spot to drop off the sample. Thus, data were collected slightly further in from the edge of the sample. This is represented by Scan D, which was a cross-section analysis of the longitudinal specimen from bottom to top at 350 μm steps. Scan E was a cross-section analysis of the center of the longitudinal specimen from bottom to top at 350 μm steps. Scan F was a cross-section analysis halfway between the center and right edge of the longitudinal specimen from bottom to top at 350 μm steps.

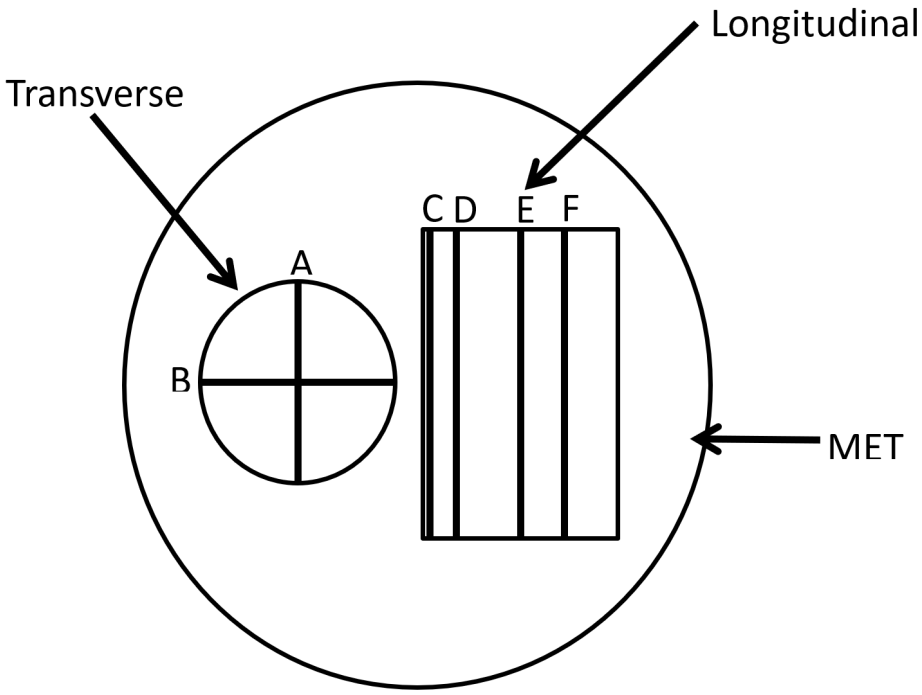

Figure 2. Diagram of transverse and longitudinal samples as mounted in the analysis orientation for Scans A, C, D, E, and F. The analysis of Scan B was performed 90° to this orientation.

All data were analyzed using EVA (Bruker AXS) for phase identification and TOPAS (Bruker AXS) for pattern refinement. All of the following fuel compositions were cast as 90 wt% U and 10 wt% Zr. Based on the room-temperature phase diagram for this binary system and assuming no Zr solubility within the α-uranium phase, the theoretical resulting phase composition is 76.7 wt% α-uranium and 23.3 wt% δ-UZr_2.

4.3.1. Ra (5% length from spade end)

The results of bulk analysis of the transverse and longitudinal cross sections for composition and lattice parameters are given in Table 8. Figure 3 shows the compiled bulk analysis scans for each of these samples along with the residuals (in gray) from data refinement using TOPAS.

Table 8. Bulk XRD analysis of Ra.

Transverse Direction (Ra2)						
Phase	Space Group	Composition (wt%)	Unit Cell Volume (Å^3)	Lattice parameters (Å)		
				a	b	c
α-Uranium	CmCm	86.63 (±0.69)	83.3950 (±0.0039)	2.857868 (±0.000084)	5.86412 (±0.00018)	4.976171 (±0.000097)
δ-UZr_2	P6/mmm	13.37 (±0.69)	68.574 (±0.052)	5.0691 (±0.0015)	—	3.0804 (±0.0014)
Longitudinal Direction (Ra5a)						
Phase	Space Group	Composition (wt%)	Unit Cell Volume (Å^3)	Lattice Parameters (Å)		
				a	b	c
α-Uranium	CmCm	72.35 (±0.89)	83.3963 (±0.0051)	2.85723 (±0.00011)	5.86490 (±0.00021)	4.97669 (±0.00014)
δ-UZr_2	P6/mmm	25.08 (±0.89)	68.16 (±0.10)	5.0387 (±0.0029)	—	3.10000 (±0.0030)
ZrC	Fm3m	2.57 (±0.30)	102.097 (±0.083)	4.6738 (±0.0013)	—	—

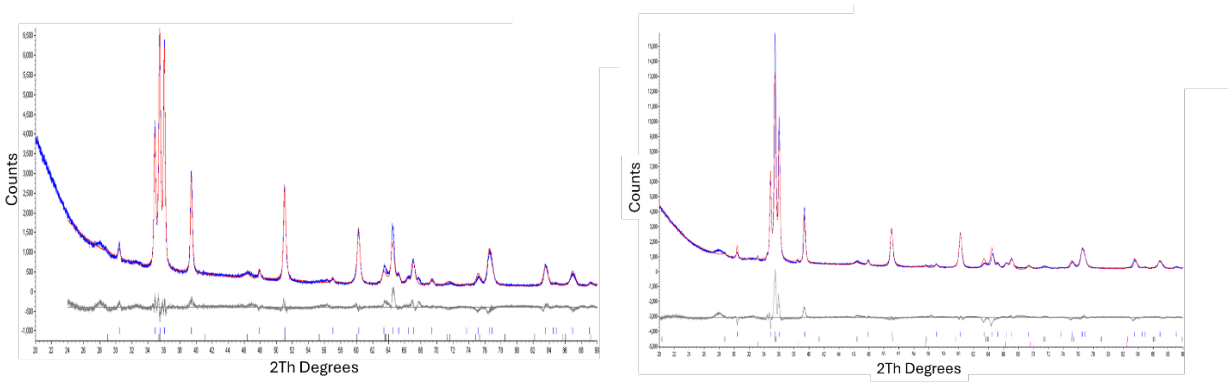

Figure 3. Rietveld refinement of the bulk XRD analysis of the Ra2 (left) and Ra5a (right) fuel matrix samples, where blue represents the measured pattern and red represents the calculated pattern with residuals shown below in gray.

The first microfocus cross-section scan of the transverse sample showed a relatively consistent phase composition of α-uranium ranging from 75 to 95 wt% and δ-UZr_2 ranging from 5 to 25 wt% across the width of the sample, as shown in Figure 4. The three-dimensional (3D) representation of the first microfocus XRD scan of the transverse Ra2 sample shows 2-theta angle on the x-axis, relative intensity on the z-axis, and translation across the sample surface on the y-axis. The circle to the right of the 3D plot shows the cross section of the sample analyzed. A Rietveld analysis of each individual scan determined the phase composition at each 150 µm step across the sample and was plotted.

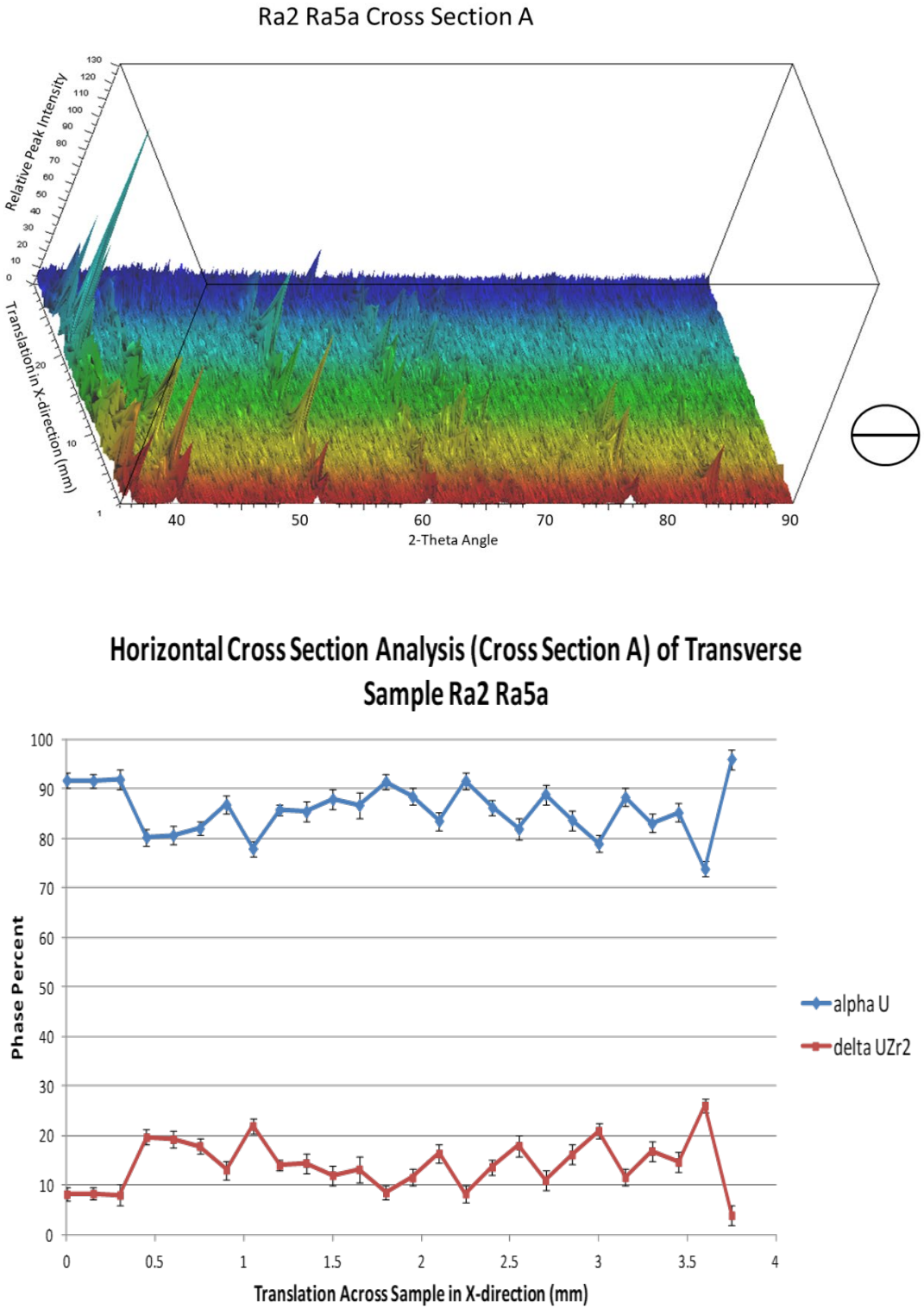

Figure 4. (top) The 3D representation of the first microfocus XRD scan of the transverse Ra2 sample; (bottom) Rietveld analysis of each individual scan.

The perpendicular microfocus cross-section scan of the transverse sample showed similar results with relatively consistent phase composition of α-uranium ranging from 79 to 91 wt% and δ-UZr_2 ranging from 9 to 21 wt%. The results from this scan are shown in Figure 5. The 3D representation of the second microfocus XRD scan of the transverse Ra2 sample shows 2-theta angle on the x-axis, relative intensity on the z-axis, and translation across the sample surface on the y-axis. The circle to the right of the 3D plot shows the cross section of the sample analyzed. A Rietveld analysis of each individual scan determined the phase composition at each 150 µm step across the sample and was plotted.

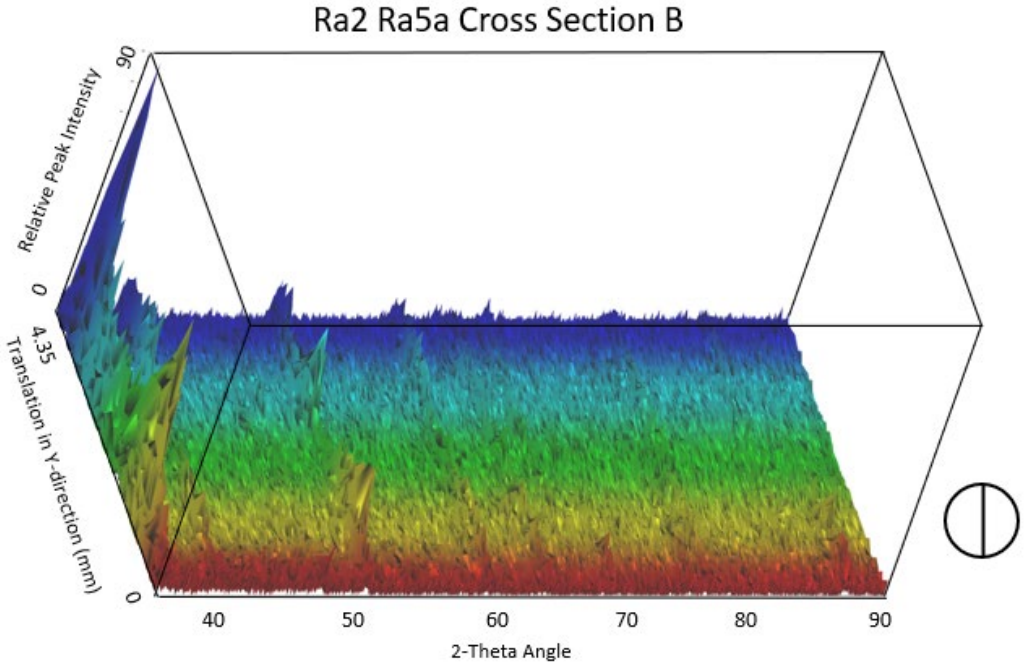

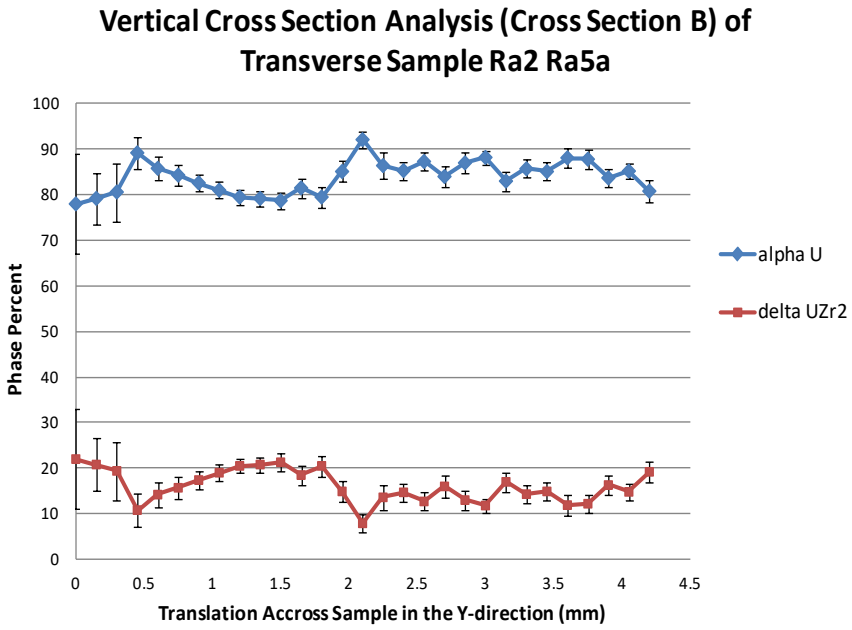

Figure 5. (top) The 3D representation of the second microfocus XRD scan of the transverse Ra2 sample; (bottom) Rietveld analysis of each individual scan.

The cross section near the edge of the Ra5a longitudinal sample showed the α-uranium fluctuating from 60 to 93 wt% and δ-UZr_2 ranging from 7 to 35 wt%, with inclusions of ZrC found at some points along the cross section ranging from 7 wt% in one location to 20 wt% in another. The results from this scan are shown in Figure 6. The 3D representation of the microfocus XRD scan nearest the edge of the longitudinal Ra5a sample shows 2-theta angle on the x-axis, relative intensity on the z-axis, and translation across the sample surface on the y-axis. The rectangle to the right of the 3D plot shows the cross section of the sample analyzed. A Rietveld analysis of each individual scan determined the phase composition at each 350 μm step across the sample and was plotted.

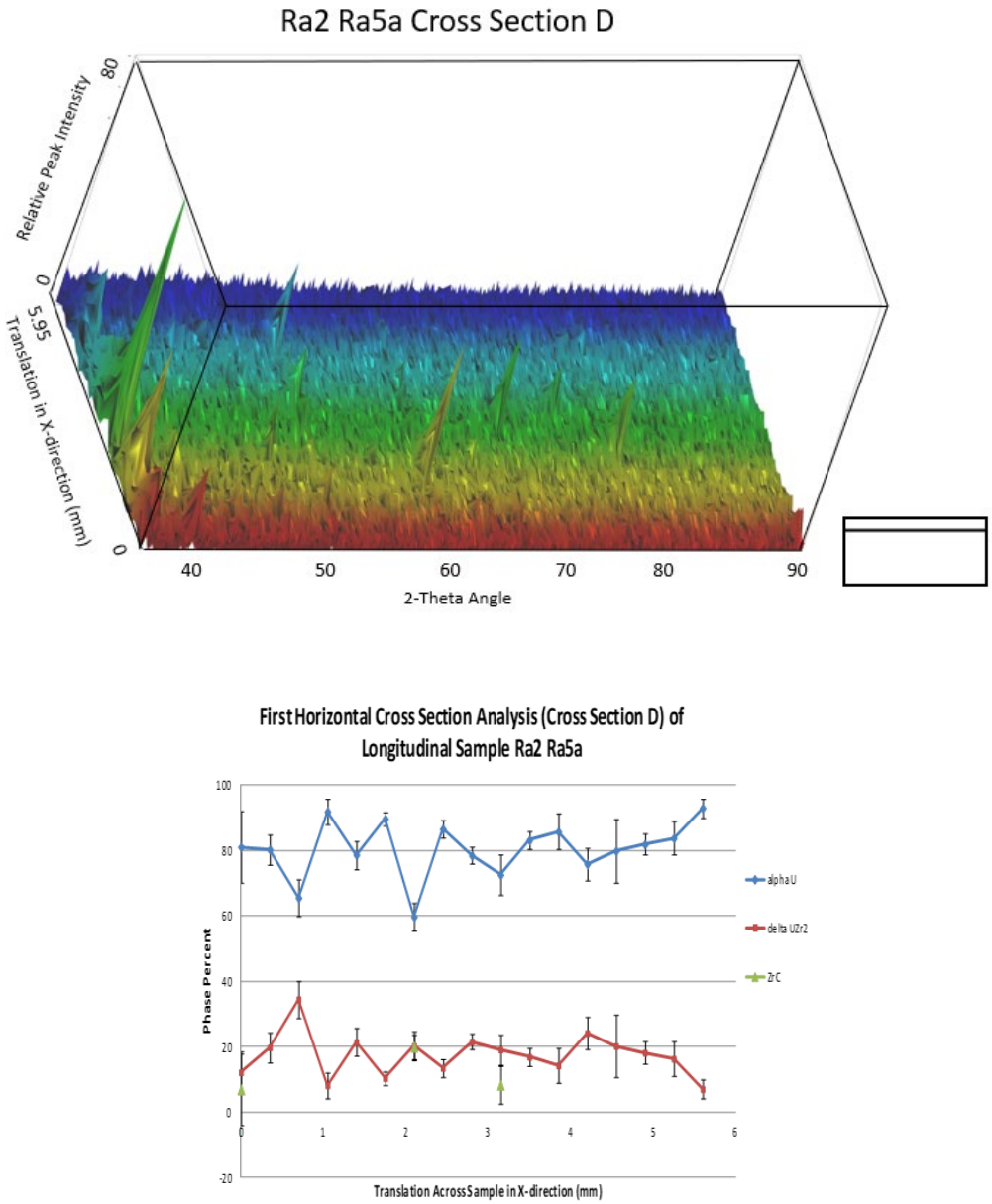

Figure 6. (top) The 3D representation of the microfocus XRD scan nearest the edge of the longitudinal Ra5a sample; (bottom) Rietveld analysis of each individual scan.

The cross-section scan of the center of the Ra5a longitudinal sample showed α-uranium ranging from 77 to 96 wt% and δ-UZr_2 ranging from 4 to 20 wt%, with inclusions of ZrC found at some points along the cross section ranging from as little as 1 wt% up to 5 wt%. The results from this scan are shown in Figure 7. The 3D representation of the microfocus XRD scan at the center of the longitudinal Ra2 Ra5a sample shows 2-theta angle on the x-axis, relative intensity on the z-axis, and translation across the sample surface on the y-axis. The rectangle to the right of the 3D plot shows the cross section of the sample analyzed. A Rietveld analysis of each individual scan determined the phase composition at each 350 μm step across the sample and was plotted.

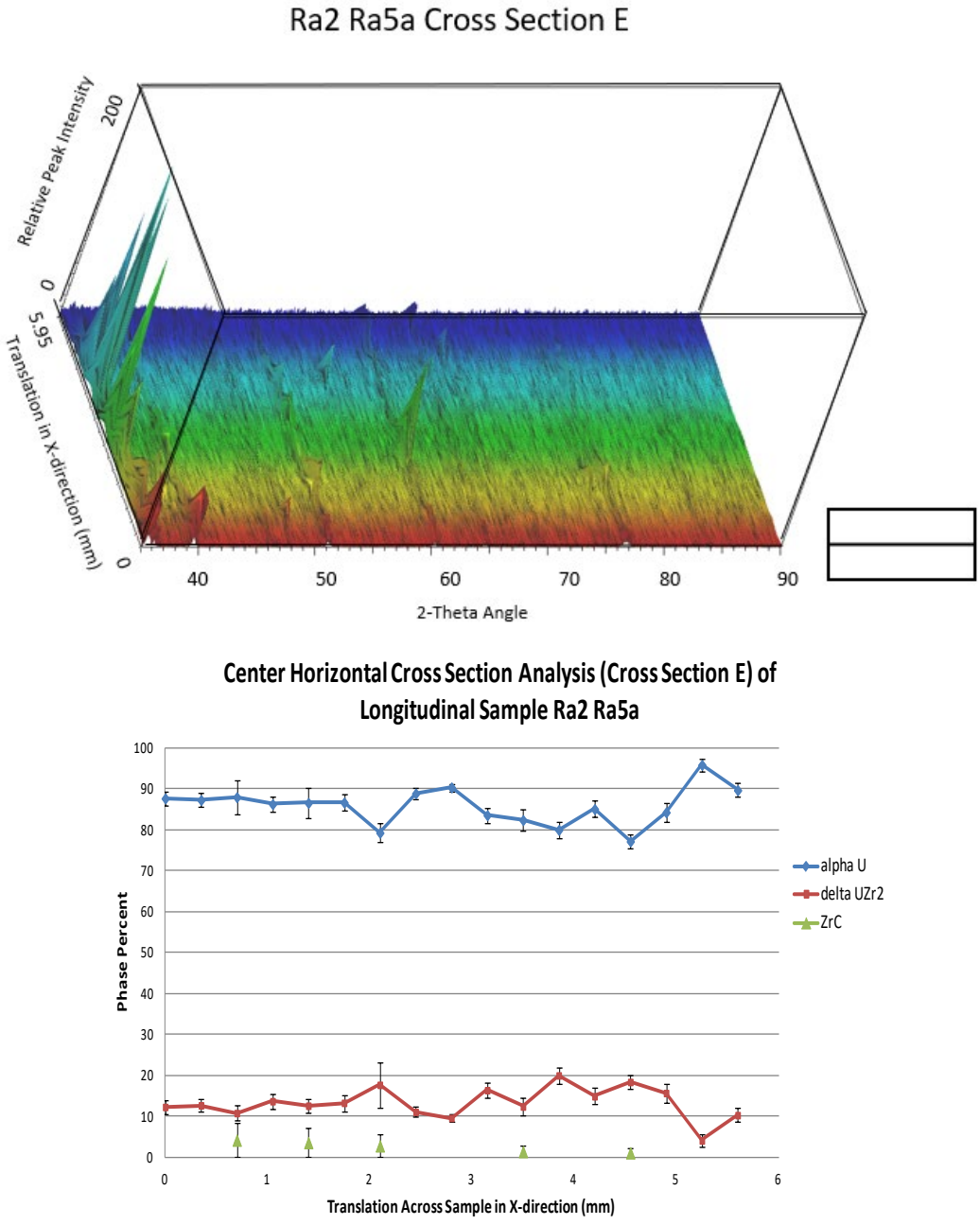

Figure 7. (top) The 3D representation of the microfocus XRD scan at the center of the longitudinal Ra2 Ra5a sample; (bottom) Rietveld analysis of each individual scan.

The cross-section scan of the longitudinal Ra5a sample halfway between the sample center and the sample edge showed α-uranium ranging from 73 to 97 wt% and δ-UZr_2 ranging from 3 to 20 wt%, with inclusions of ZrC at two points along the cross section: at 1 wt% and at 10 wt%. The results from this scan are shown in Figure 8. The 3D representation of the microfocus XRD scan halfway between the edge and the center of the longitudinal Ra5a sample shows the 2-theta angle on the x-axis, relative intensity on the z-axis, and translation across the sample surface on the y-axis. The rectangle to the right of the 3D plot shows the cross section of the sample analyzed. A Rietveld analysis of each individual scan determined the phase composition at each 350 μm step across the sample and was plotted.

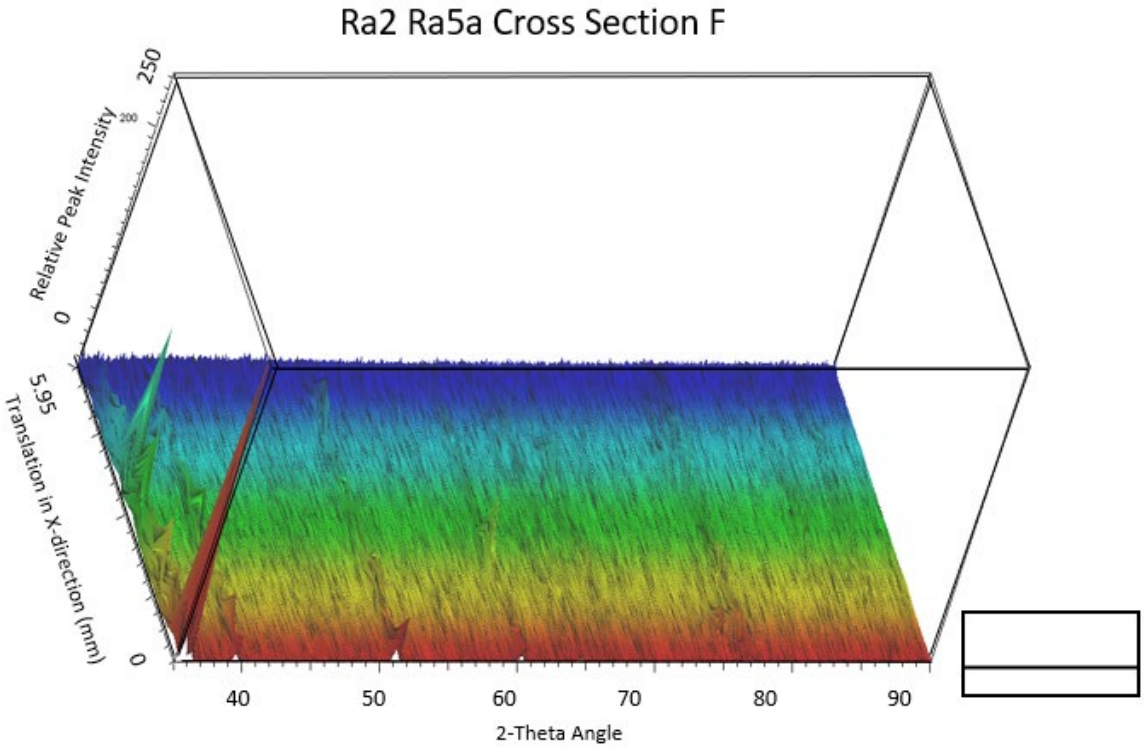

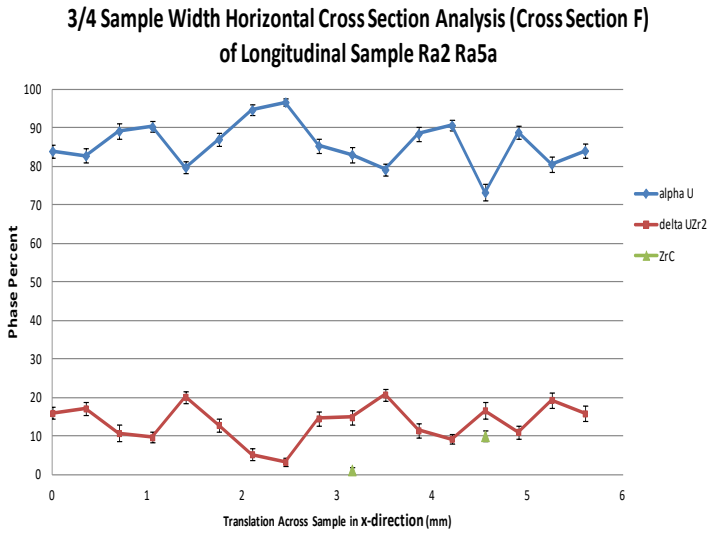

Figure 8. (top) The 3D representation of the microfocus XRD scan of the longitudinal Ra5a sample; (bottom) Rietveld analysis of each individual scan.

4.3.2. Rb (50% length from spade end)

The results of the bulk analysis of the transverse and longitudinal cross sections for composition and lattice parameters are given in Table 9. Figure 9 shows the compiled bulk analysis scans for each of these samples along with the residuals (in gray) from data refinement using TOPAS.

Table 9. Bulk XRD analysis of Rb.

Transverse Direction (Rb2)						
Phase	Space Group	Composition (wt%)	Unit Cell Volume (Å^3)	Lattice parameters (Å)		
				a	b	c
α-Uranium	CmCm	81.40 (±0.60)	83.3370 (±0.0035)	2.857871 (±0.000074)	5.85929 (±0.00016)	4.976796 (±0.000085)
d-UZr_2	P6/mmm	14.61 (±0.45)	68.581 (±0.030)	5.06671 (±0.00083)	—	3.08477 (±0.00092)
ZrC	Fm3m	1.02 (±0.19)	102.44 (±0.10)	4.6791 (±0.0015)	—	—
UO_2	Fm3m	2.98 (±0.46)	163.09 (±0.22)	5.4635 (±0.0024)	—	—
Longitudinal Direction (Rb5a)						
Phase	Space Group	Composition (wt%)	Unit Cell Volume (Å^3)	Lattice parameters (Å)		
				a	b	c
α-Uranium	CmCm	78.06 (±0.54)	83.2984 (±0.0031)	2.857405 (±0.000059)	5.85883 (±0.000059)	4.975698 (±0.000091)
d-UZr_2	P6/mmm	14.52 (±0.37)	68.586 (±0.039)	5.0640 (±0.0010)	—	3.0882 (±0.0012)
UO_2	Fm3m	7.42 (±0.50)	164.15 (±0.13)	5.4754 (±0.00144)	—	—

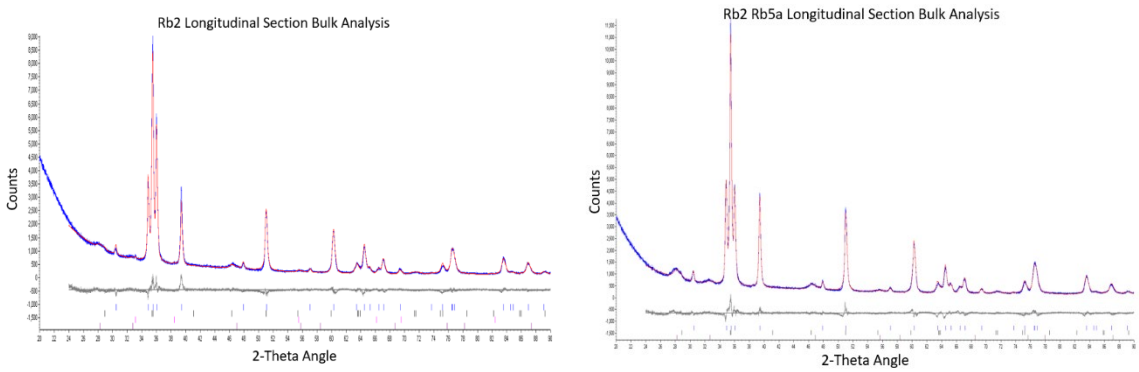

Figure 9. Rietveld refinement of the bulk XRD analysis of the Rb2, Rb5a fuel matrix sample. Blue represents the measured pattern and red represents the calculated pattern with residuals shown below in gray.

The first microfocus cross section scan of the transverse Rb2 sample showed a phase composition of α-uranium ranging from 80 to 100 wt% and δ-UZr_2 ranging from 0 to 19 wt % across the width of the sample. Additional residual peaks were identified as cubic ZrC (Fm-3m) ranging from 1 to 19 wt% and γ-uranium at very low weight percent

ranging from 0.7 to 0.6 wt%. A summary of the data from this cross section of the transverse specimen is shown in Figure 10 below. The 3D representation of the first microfocus XRD scan of the transverse Rb2 sample shows 2-theta angle on the x-axis, relative intensity on the z-axis and translation across the sample surface on the y-axis. The circle to the right of the 3D plot shows the cross section of the sample analyzed. Rietveld analysis of each individual scan was done to determine the phase composition at each 150 μm step across the sample and plotted.

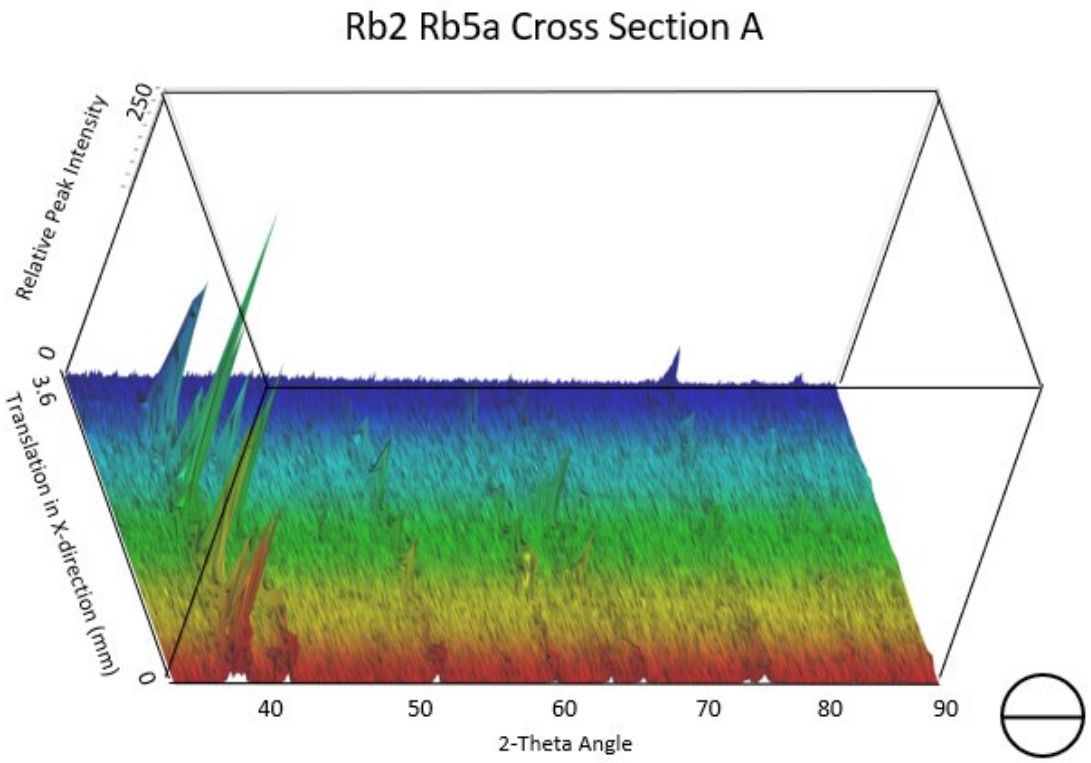

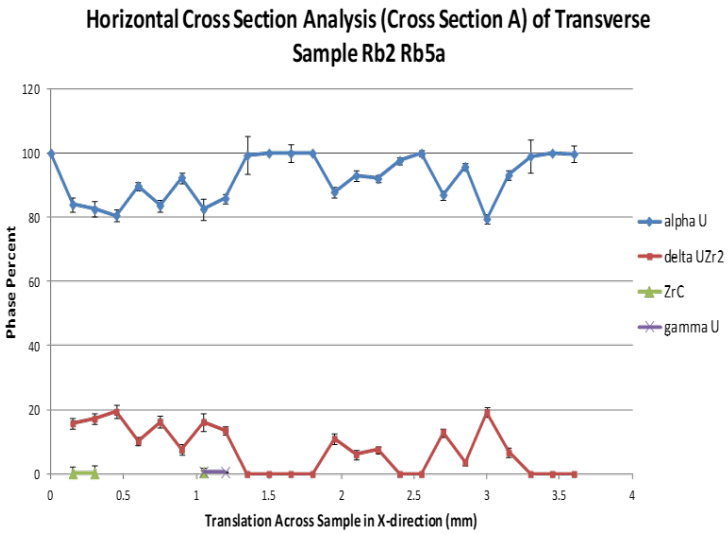

Figure 10 (top) The 3D representation of the first microfocus XRD scan of the transverse Rb2 sample; (bottom) Rietveld analysis of each individual scan.

The perpendicular microfocus cross section scan of the transverse sample showed almost 100% of the sample to be α-uranium with some variance in weight percent ranging from 82 to 100 wt% with lower than expected δ-UZr_2 ranging from 0 to 5 wt%. Two analysis locations also showed very small amounts of ZrC. The results from this scan are shown in Figure 11 below. The 3D representation of the perpendicular microfocus XRD scan of the transverse Rb2 sample shows 2-theta angle on the x-axis, relative intensity on the z-axis and translation across the sample surface on the y-axis. The circle to the right of the 3D plot shows the cross section of the sample analyzed. Rietveld analysis of each individual scan was done to determine the phase composition at each 150-µm step across the sample and plotted.

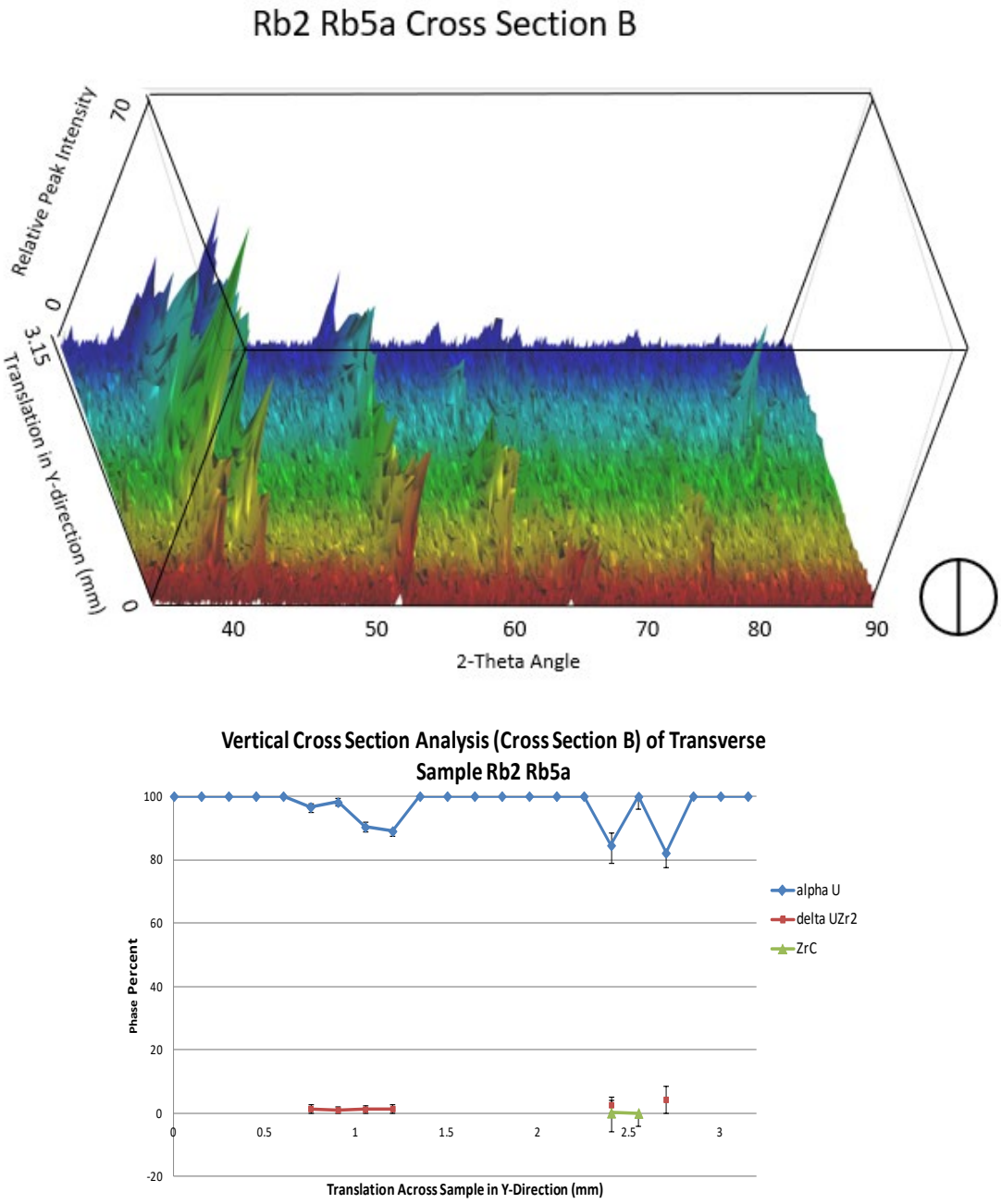

Figure 11. (top) The 3D representation of the perpendicular microfocus XRD scan of the transverse Rb2 sample; (bottom) Rietveld analysis of each individual scan.

The cross section near the edge of the Rb5a longitudinal sample showed the α-uranium composition fluctuating from 57 to 97 wt% and δ-UZr_2 ranging from 3 to 41 wt% with inclusions of ZrC found at three analysis points ranging from 1 to 3 wt% and UO_2 from 6 to 8 wt%, likely from surface oxidation. The results from this scan are shown in Figure 12. The 3D representation of the microfocus XRD scan nearest the edge of the longitudinal Rb5a sample shows 2-theta angle on the x-axis, relative intensity on the z-axis and translation across the sample surface on the y-axis. The rectangle to the right of the 3D plot shows the cross section of the sample analyzed. Rietveld analysis of each individual scan was done to determine the phase composition at each 350 µm step across the sample and plotted.

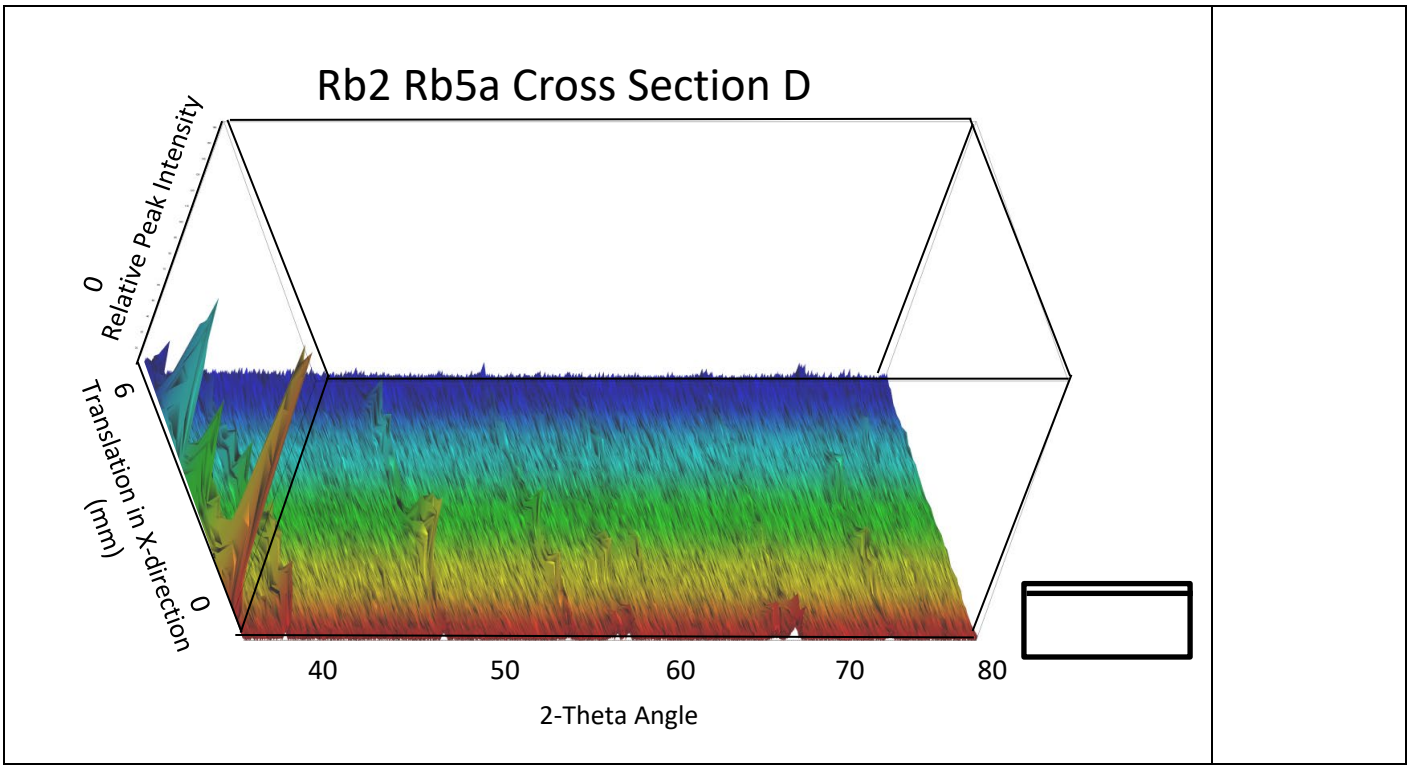

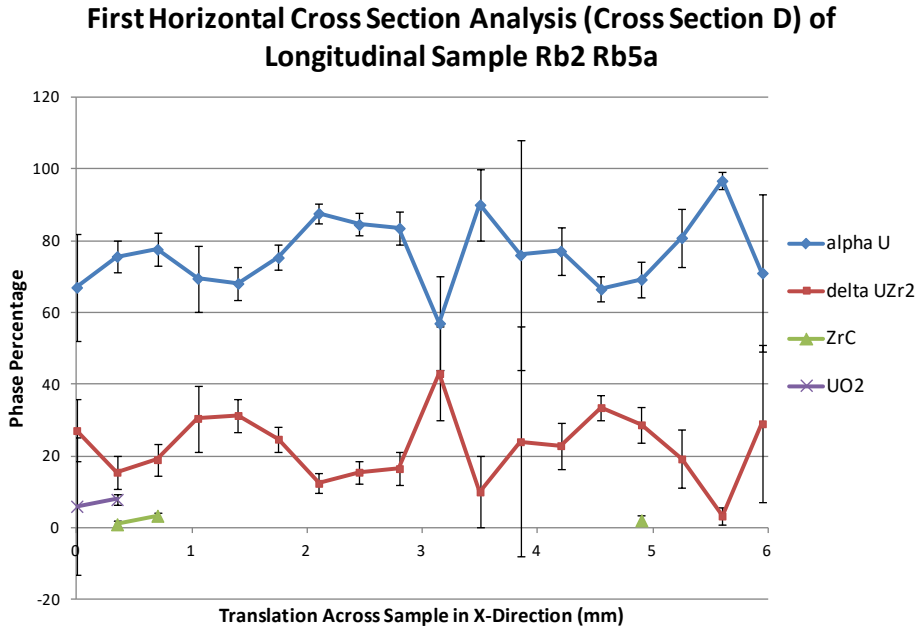

Figure 12. (top) The 3D representation of the microfocus XRD scan nearest the edge of the longitudinal Rb5a; (bottom) Rietveld analysis of each individual scan.

The cross-section scan of the center of the Rb5a longitudinal sample showed α-uranium ranging from 58 to 95 wt% and δ-UZr_2 ranging from 5 to 40 wt% with inclusions of ZrC found at two points along the cross section ranging from as little as 0.7 wt% in one spot to 7 wt% in the other. The results from this scan are shown in Figure 13 below. The 3D representation of the microfocus XRD scan at the center of the longitudinal Rb5a sample shows 2-theta angle on the x-axis, relative intensity on the z-axis and translation across the sample surface on the y-axis. The rectangle to

the right of the 3D plot shows the cross section of the sample analyzed. Rietveld analysis of each individual scan was done to determine the phase composition at each 350 μm step across the sample and plotted.

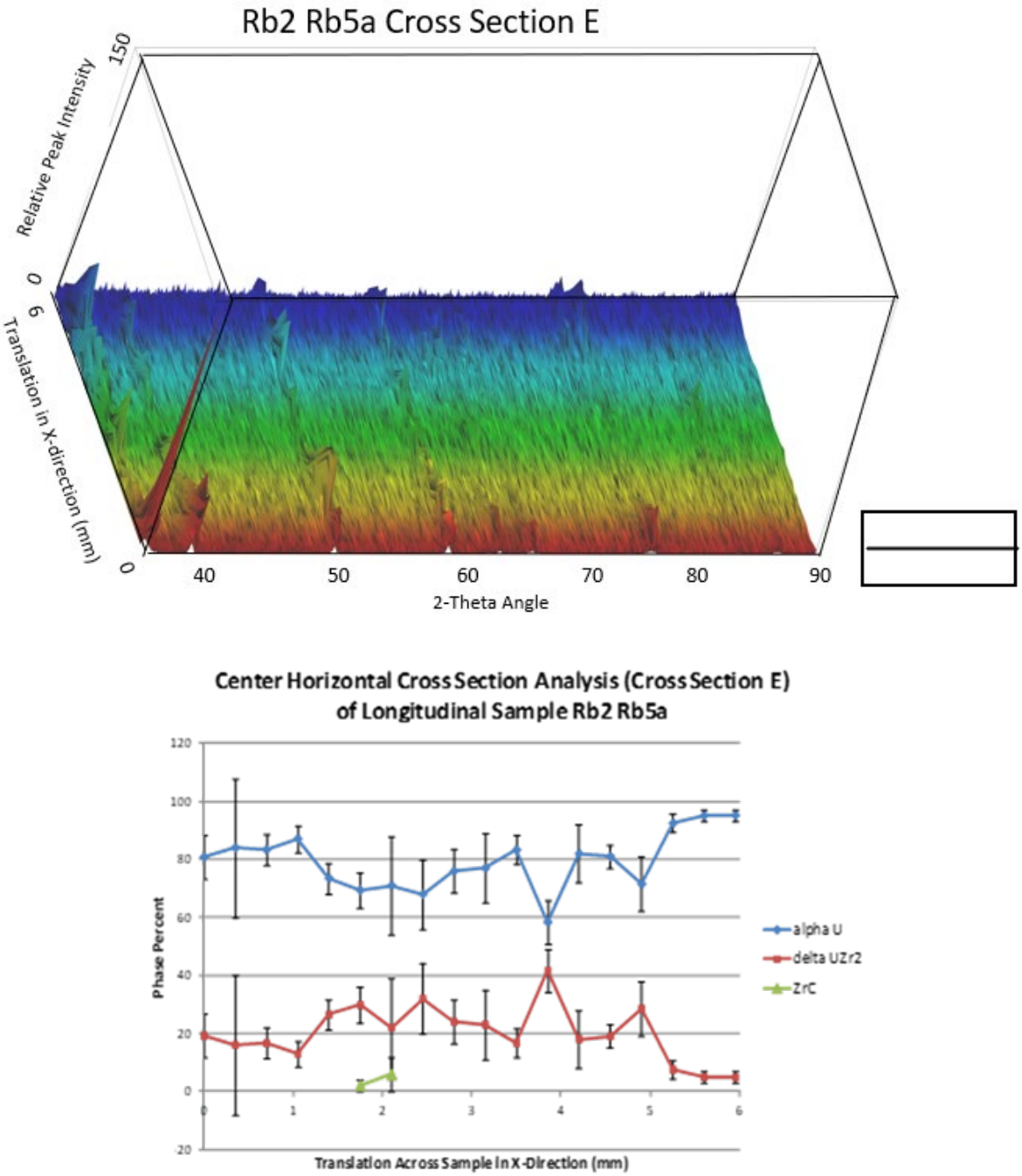

Figure 13. (top) The 3D representation of the microfocus XRD scan at the center of the longitudinal Rb5a; (bottom) Rietveld analysis of each individual scan.

The cross-section scan of the longitudinal Rb5a sample halfway between the sample center and the sample edge showed α-uranium ranging from 61 to 92 wt% and δ-UZr_2 ranging from 5 to 39 wt% with inclusions of ZrC at two points along the cross section, one at 1 wt% and the other at 5.5 wt%. The results from this scan are shown in Figure 14

below. The 3D representation of the microfocus XRD scan halfway between the edge and the center of the longitudinal Rb5a sample shows 2-theta angle on the x-axis, relative intensity on the z-axis and translation across the sample surface on the y-axis. The rectangle to the right of the 3D plot shows the cross section of the sample analyzed. Rietveld analysis of each individual scan was done to determine the phase composition at each 350 µm step across the sample and plotted.

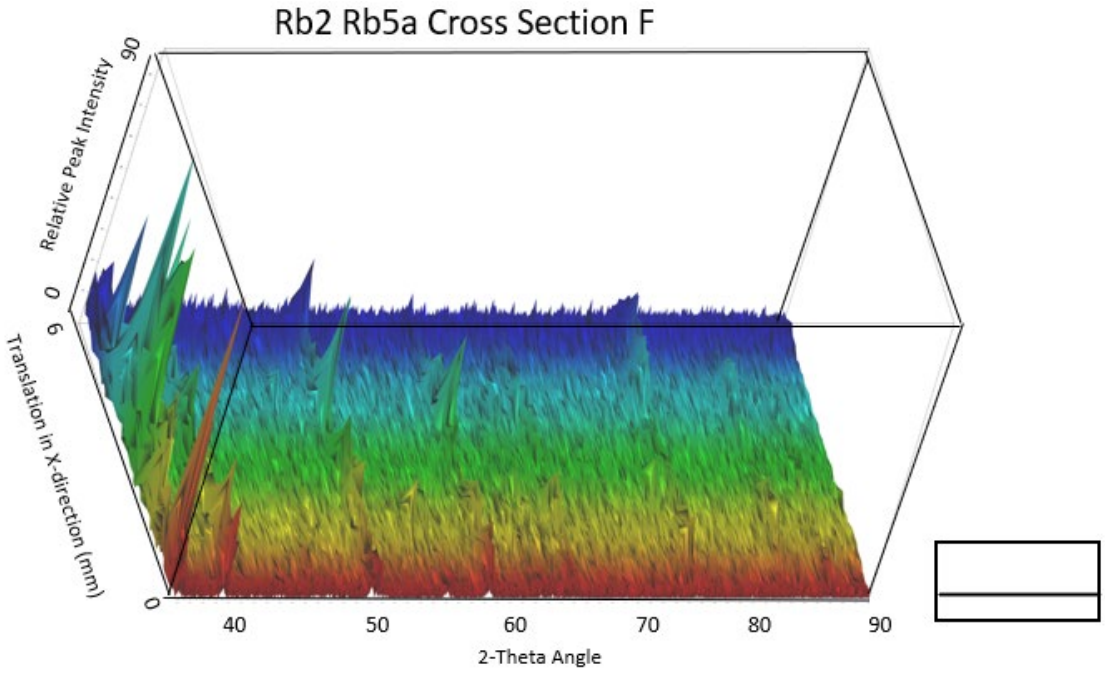

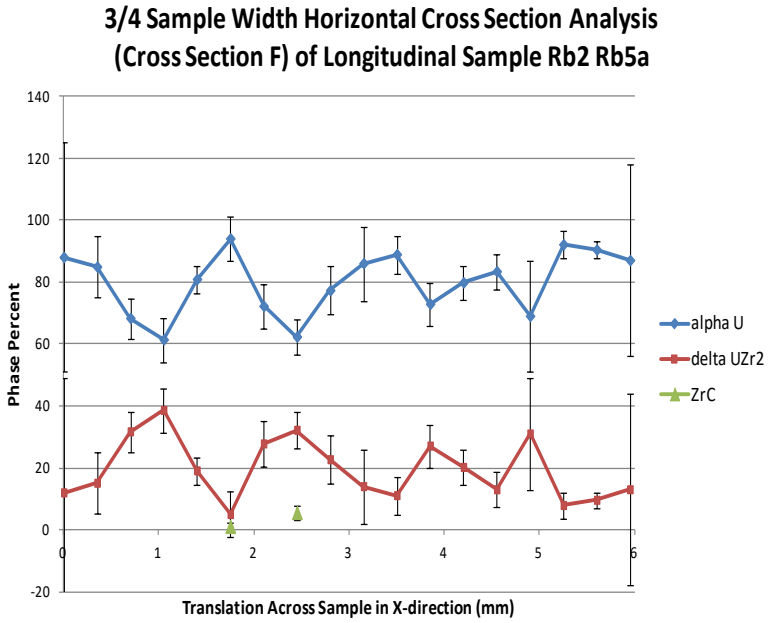

Figure 14. 3D representation of the microfocus XRD scan halfway between the edge and the center of the longitudinal Rb5a sample; (bottom) Rietveld analysis of each individual scan.

4.3.3. Rc (95% length from spade end)

The results of bulk analysis of the transverse and longitudinal cross sections for composition and lattice parameters are given in Table 10. Figure 15 below shows the compiled bulk analysis scans for each of these samples along with the residuals (in gray) from data refinement using TOPAS.

Table 10. Bulk XRD analysis of specimen, Rc.

Transverse Direction (Rc2)						
Phase	Space Group	Composition (wt%)	Unit Cell Volume (Å^3)	Latice parameters (Å)		
				a	b	c
α-Uranium	CmCm	84.93 (±0.53)	83.3142 (±0.0042)	2.856740 (±0.000089)	5.86111 (±0.00016)	4.97586 (±0.00014)
δ-UZr_2	P6/mmm	15.07 (±0.53)	68.096 (±0.070)	5.0399 (±0.0022)	—	3.0957 (±0.0017)
Longitudinal Direction (Rc5a)						
Phase	Space Group	Composition (wt%)	Unit Cell Volume (Å^3)	Lattice parameters (Å)		
				a	b	c
α-Uranium	CmCm	84.93 (±0.53)	83.3142 (±0.0042)	2.856740 (±0.000089)	5.86111 (±0.00016)	4.97586 (±0.00014)
δ-UZr_2	P6/mmm	15.07 (±0.53)	68.096 (±0.070)	5.0399 (±0.0022)	—	3.0957 (±0.0017)

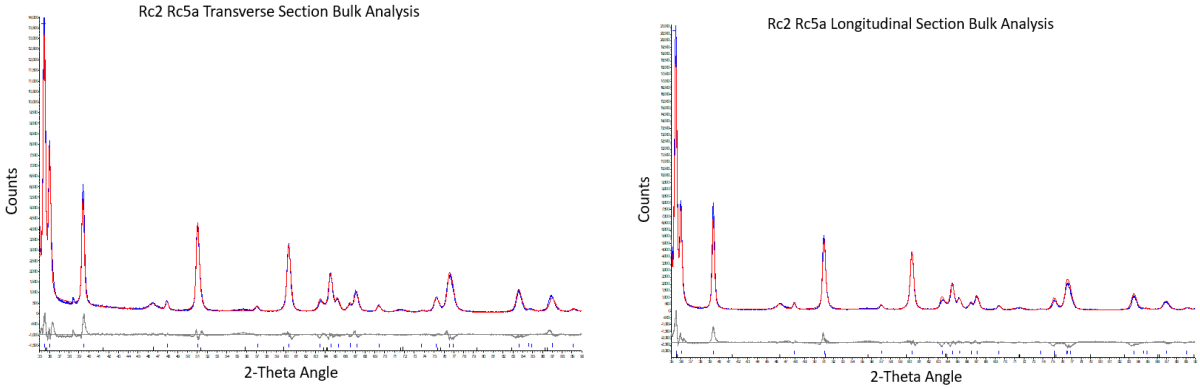

Figure 15. Rietveld refinement of the bulk analysis of the Rc2 Rc5a fuel matrix sample, where blue represents the measured pattern and red represents the calculated pattern with residuals shown below in gray.

The first microfocus cross-section scan of the transverse Rc2 sample showed a phase composition of α-uranium ranging from 81 to 95 wt% and δ-UZr_2 ranging from 5 to 17 wt% across the width of the sample. Additional residual peaks were identified as γ-uranium at a very low weight percent ranging from 0.4 to 1.0 wt%. A summary of the data from this cross section of the transverse specimen is shown in Figure 16. The 3D representation of the first microfocus XRD scan of the transverse Rc2 sample shows 2-theta angle on the x-axis, relative intensity on the z-axis, and translation across the sample surface on the y-axis. The circle to the right of the 3D plot shows the cross section of the sample analyzed. A Rietveld analysis of each individual scan determined the phase composition at each 150 µm step across the sample and was plotted.

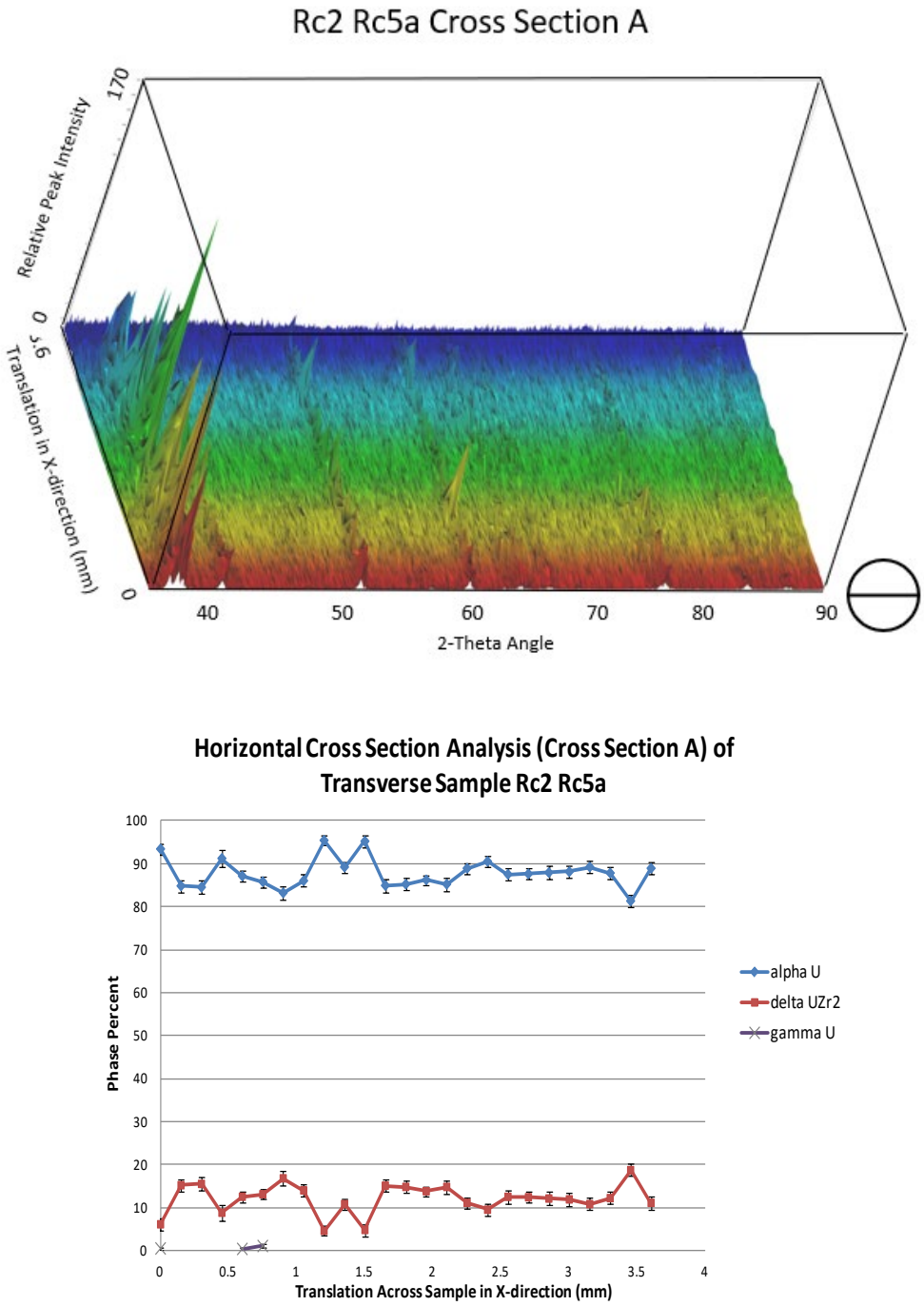

Figure 16. (top) The 3D representation of the first microfocus XRD scan of the transverse Rc2 sample; (bottom) Rietveld analysis of each individual scan.

The perpendicular microfocus cross-section scan of the transverse Rc2 sample showed the phase composition of 73–94 wt% α-uranium and 4–22 wt% δ-UZr_2. Additional ZrC was detected in five of the analysis locations ranging from 2 to 13 wt%. The results from this scan are shown in Figure 17. The 3D representation of the perpendicular microfocus XRD scan of the transverse Rc2 sample shows 2-theta angle on the x-axis, relative intensity on the z-axis, and translation across the sample surface on the y-axis. The circle to the right of the 3D plot shows the cross section of

the sample analyzed. A Rietveld analysis of each individual scan determined the phase composition at each 150 µm step across the sample and was plotted.

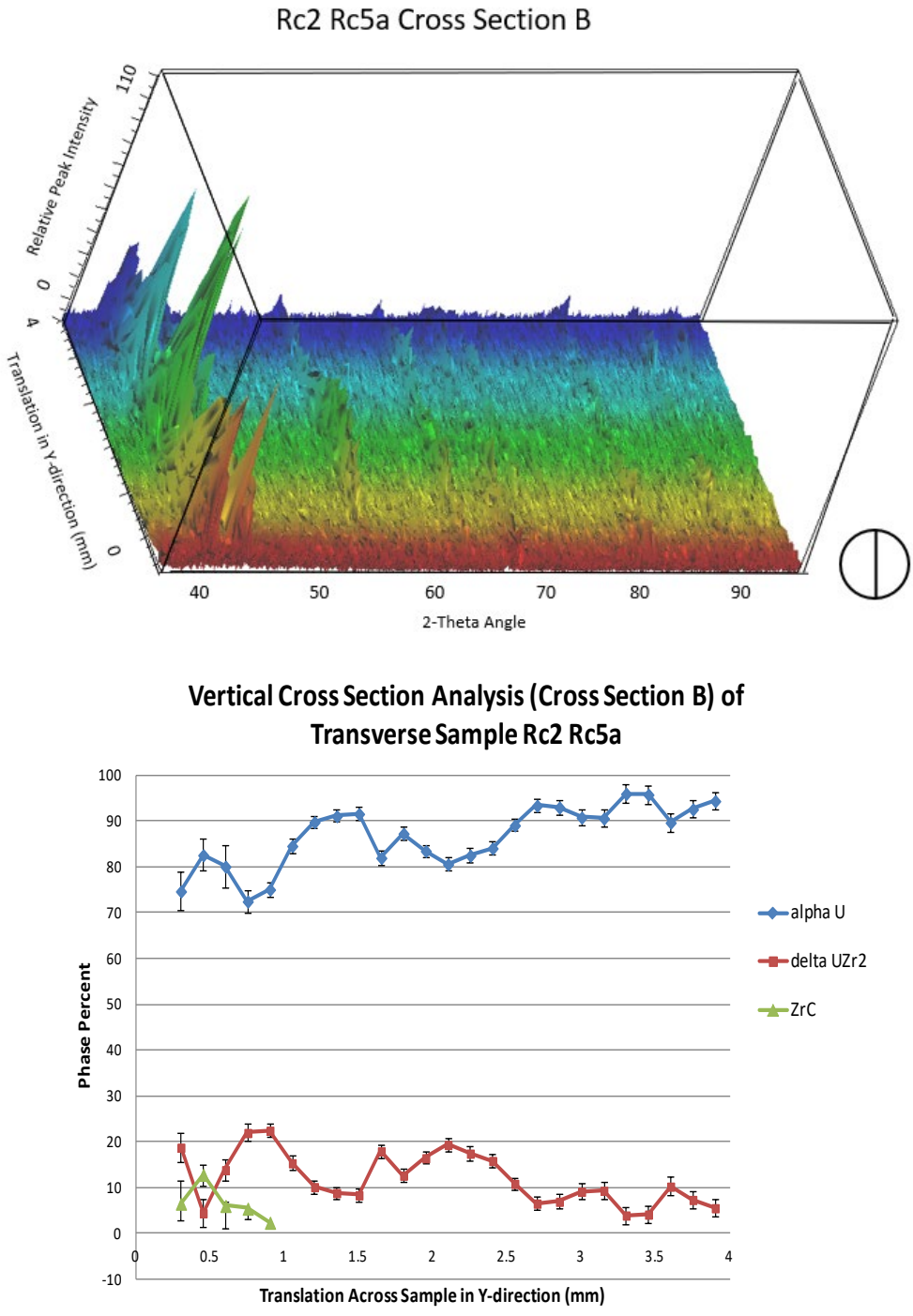

Figure 17. (top) The 3D representation of the perpendicular microfocus XRD scan of the transverse Rc2 sample; (bottom) Rietveld analysis of each individual scan.

The cross section near the edge of the Rc5a longitudinal sample showed the α-uranium (CmCm) composition ranging from 75 to 99 wt% and δ-UZr_2 (P6/mmm) ranging from 1 to 25 wt%. No additional phases were identified.

The results from this scan are shown in Figure 18. The 3D representation of the microfocus XRD scan nearest the edge of the longitudinal Rc5a sample shows 2-theta angle on the x-axis, relative intensity on the z-axis, and translation across the sample surface on the y-axis. The rectangle to the right of the 3D plot shows the cross section of the sample analyzed. A Rietveld analysis of each individual scan determined the phase composition at each 350 µm step across the sample and was plotted.

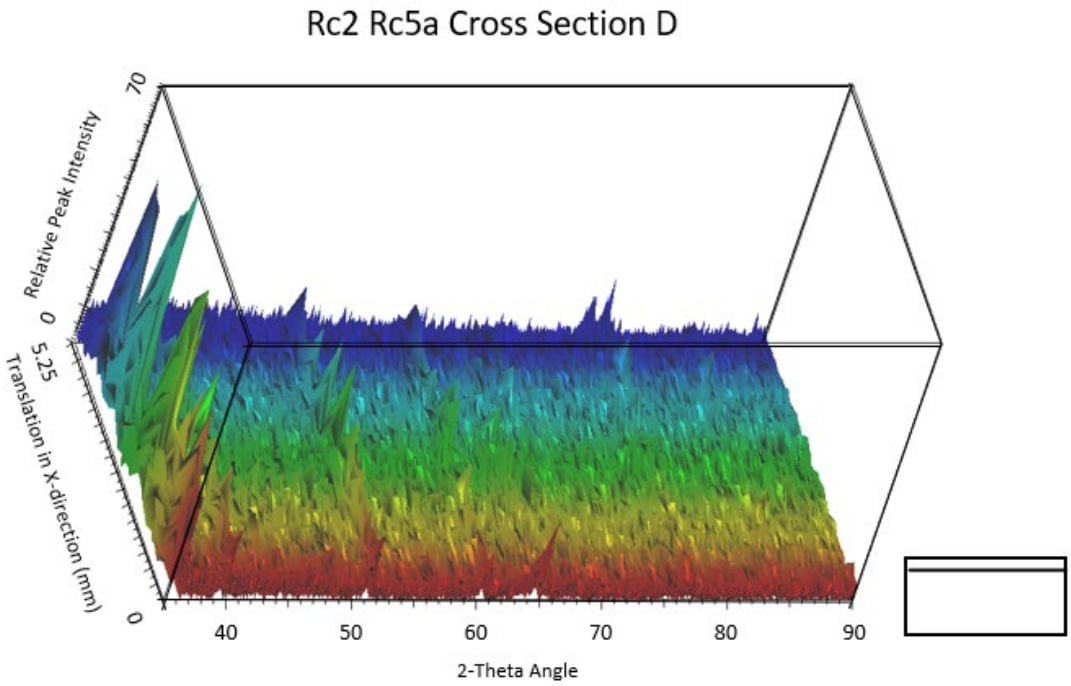

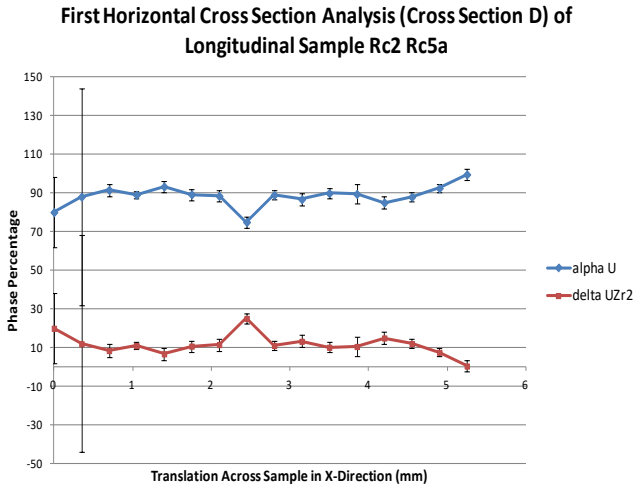

Figure 18. (top) The 3D representation of the microfocus XRD scan nearest the edge of the longitudinal Rc5a sample; (bottom) Rietveld analysis of each individual scan.

The cross-section scan of the center of the Rc5a longitudinal sample showed α-uranium ranging from 81 to 93 wt% and δ-UZr_2 ranging from 7 to 20 wt%. The results from this scan are shown in Figure 19. The 3D representation of the microfocus XRD scan at the center of the longitudinal Rc5a sample shows 2-theta angle on the x-axis, relative intensity

on the z-axis, and translation across the sample surface on the y-axis. The rectangle to the right of the 3D plot shows the cross section of the sample analyzed. A Rietveld analysis of each individual scan determined the phase composition at each 350 µm step across the sample and was plotted.

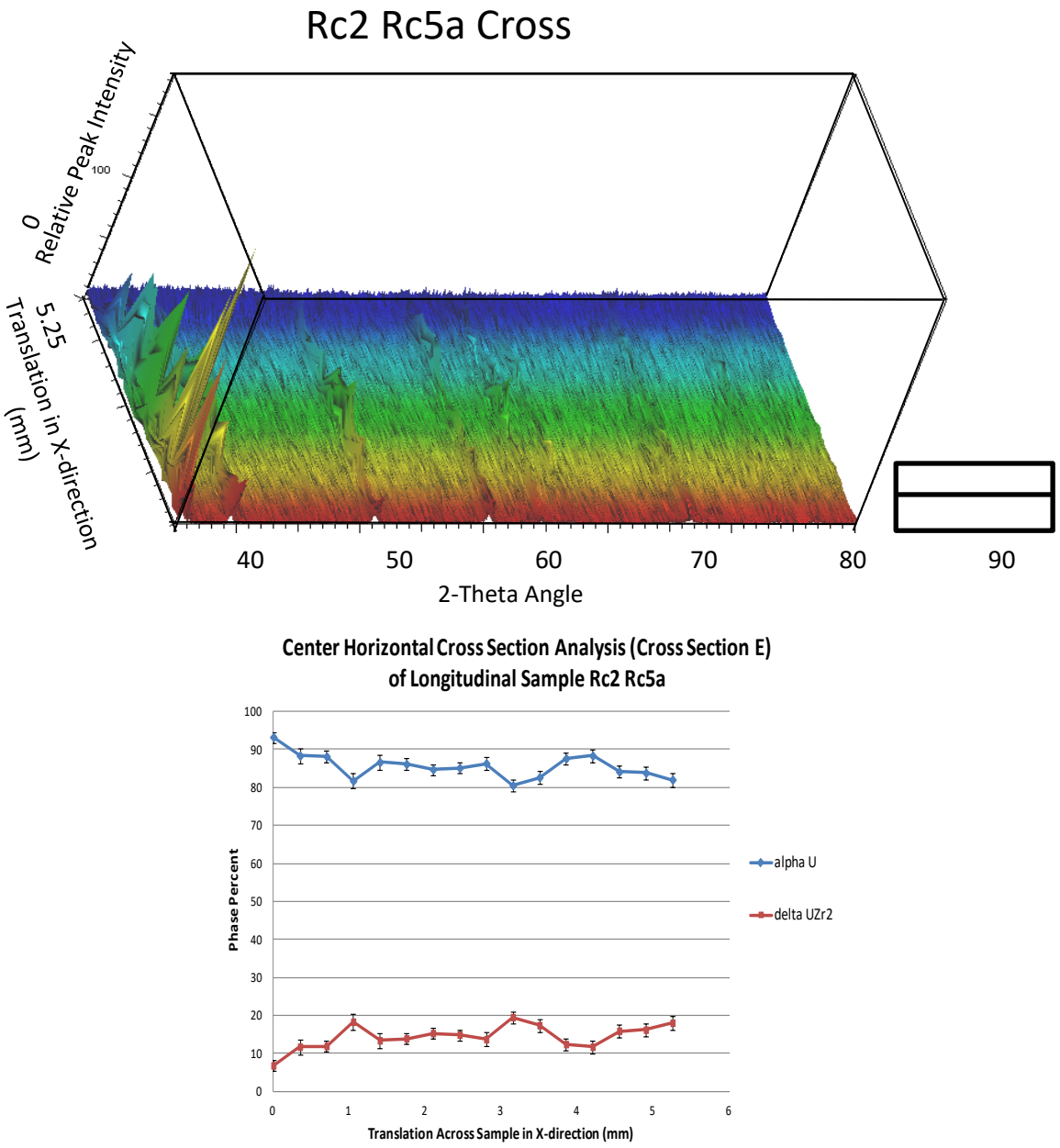

Figure 19. (top) The 3D representation of the microfocus XRD scan at the center of the longitudinal Rc5a sample; (bottom) Rietveld analysis of each individual scan.

The cross-section scan of the longitudinal Rc5a sample halfway between the sample center and the sample edge showed α-uranium ranging from 78 to 88 wt% and δ-UZr_2 ranging from 12 to 22 wt%. The results from this scan are shown in Figure 20. The 3D representation of the microfocus XRD scan halfway between the edge and the center of the longitudinal Rc5a sample shows 2-theta angle on the x-axis, relative intensity on the z-axis, and translation across the sample surface on the y-axis. The rectangle to the right of the 3D plot shows the cross section of the sample

analyzed. A Rietveld analysis of each individual scan determined the phase composition at each 350 µm step across the sample and was plotted.

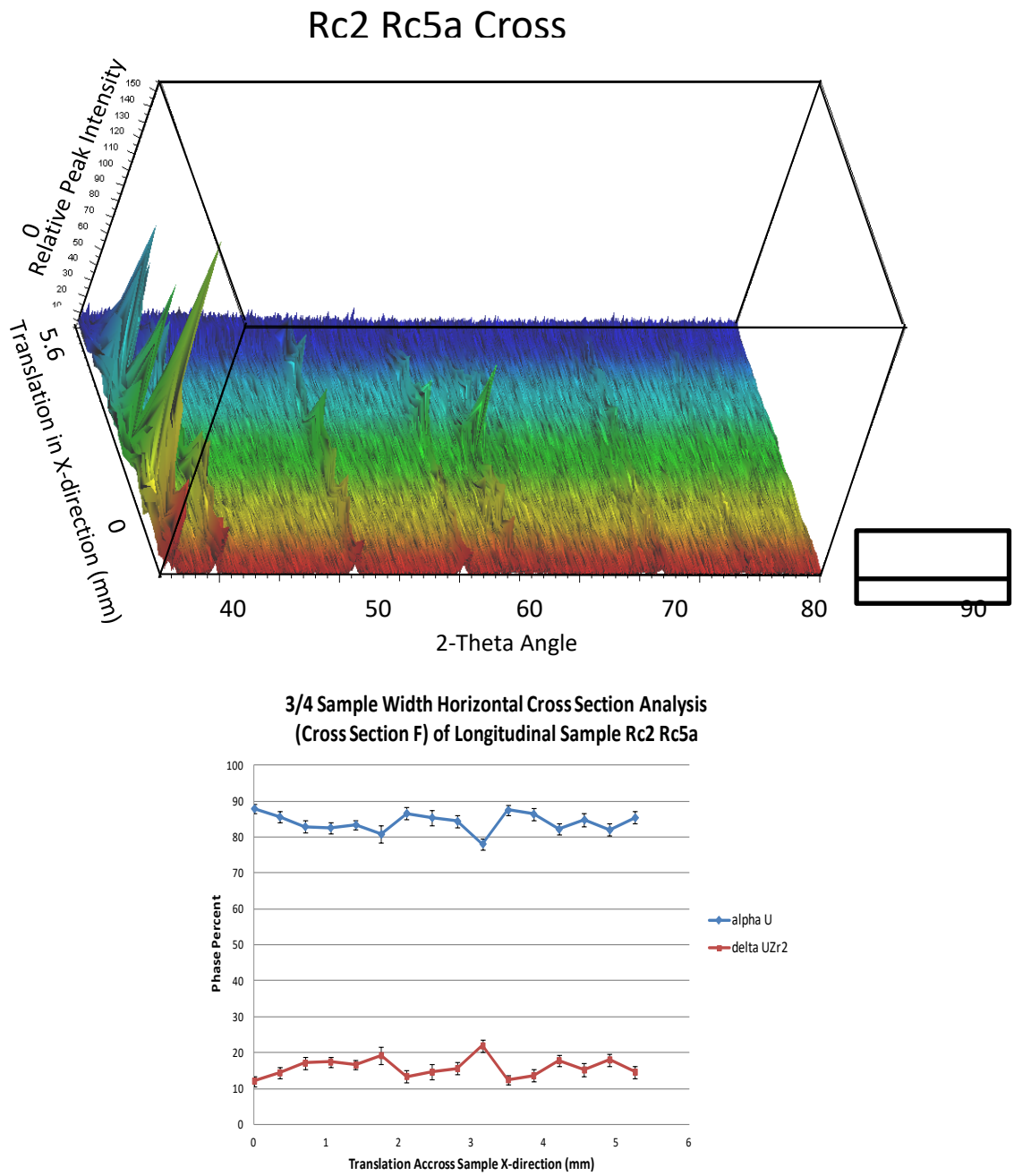

Figure 20. (top) The 3D representation of the microfocus XRD scan halfway between the edge and the center of the longitudinal Rc5a sample; (bottom) Rietveld analysis of each individual scan.

5. FUEL MICROSCOPY AND MICROSTRUCTURE

5.1. SEM

5.1.1. Matrix Description

The U-10 Zr matrix of the EBR-II fuel specimens examined has a fine lamellar bainitic/martensitic structure (see Figure 21 and Figure 22). The lamellae are under 100 nm in thickness and cannot be resolved by x-ray spectroscopy. However, uranium has a higher atomic number (Z = 92) than Zr (Z = 40), so phases with more U scatter more electrons than those with more Zr and subsequently appear brighter in backscatter electron (BSE) images.

Recall that the slugs were not marked before being loaded into the cladding as to the relative position in the quartz mold when casting. This is important because, although the quartz mold was coated with a ZrO_2 slurry and dried prior to casting, the interaction with the mold appears, in this study, to be greatest near one end. We theorized that this was caused by being at the end closest to the melt. At that location, it would be at an elevated temperature for longer than at the end furthest from the melt pool. It appears that Ra is that section for the slug retrieved. Note below, the "rind" description, showing the outer radius of the fuel slug samples.

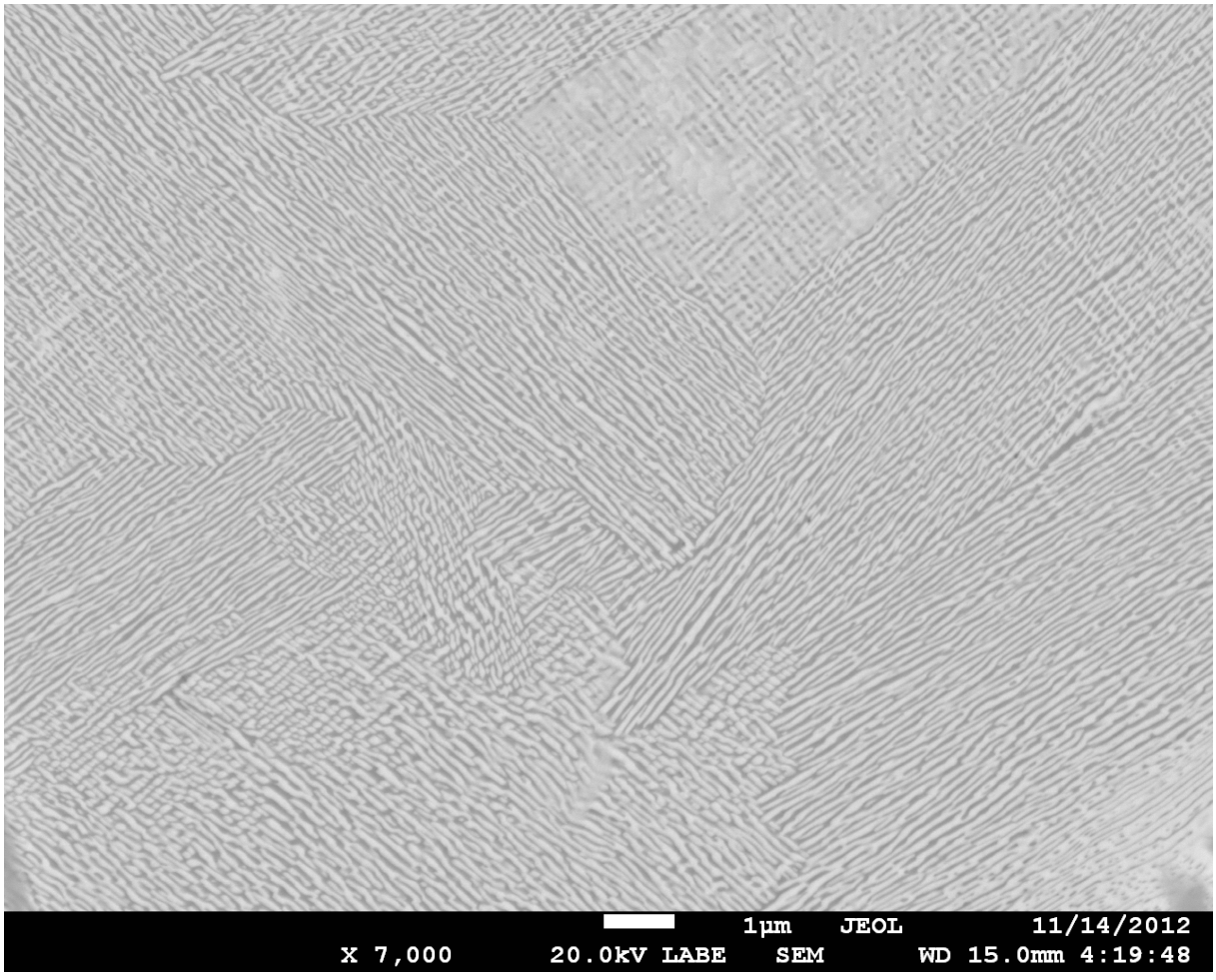

Figure 21. BSE image of the lamellar U-10 Zr matrix structure of Ra.

There is significant porosity present in Ra and Rb along the fuel pin from the spade end of the assembly (see Figure 23, Figure 24, and Figure 25). Porosity near the center axis of Ra (see Figure 23) is considerably less than that near the rind (see Figure 24). However, porosity in Rb is limited to near the center of the pin and is not present near the rind. Very minimal porosity was observed in Rc. The porosity all has the appearance of shrinkage during solidification.

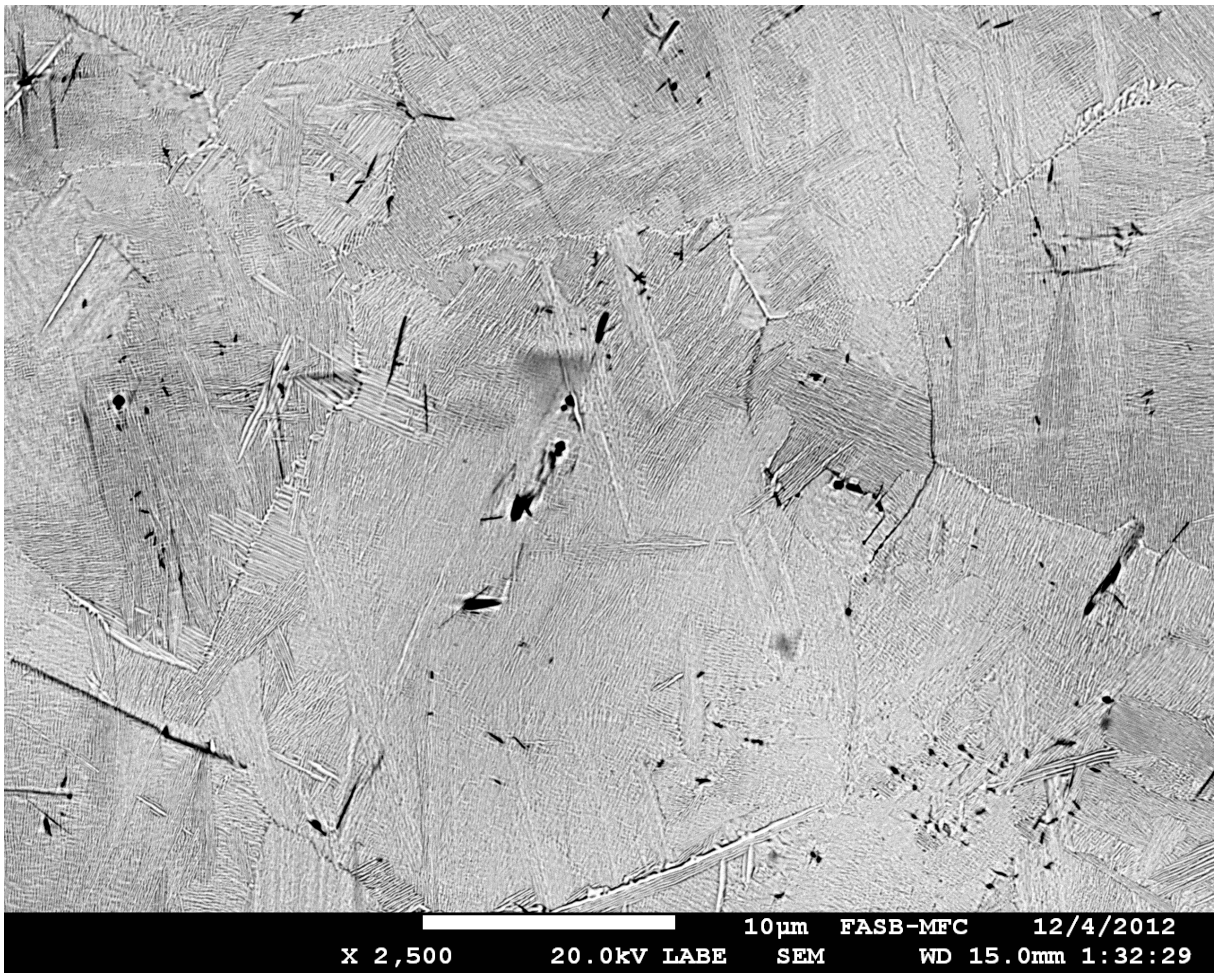

Figure 22. BSE image of the lamellar U-10 Zr matrix structure of Rc.

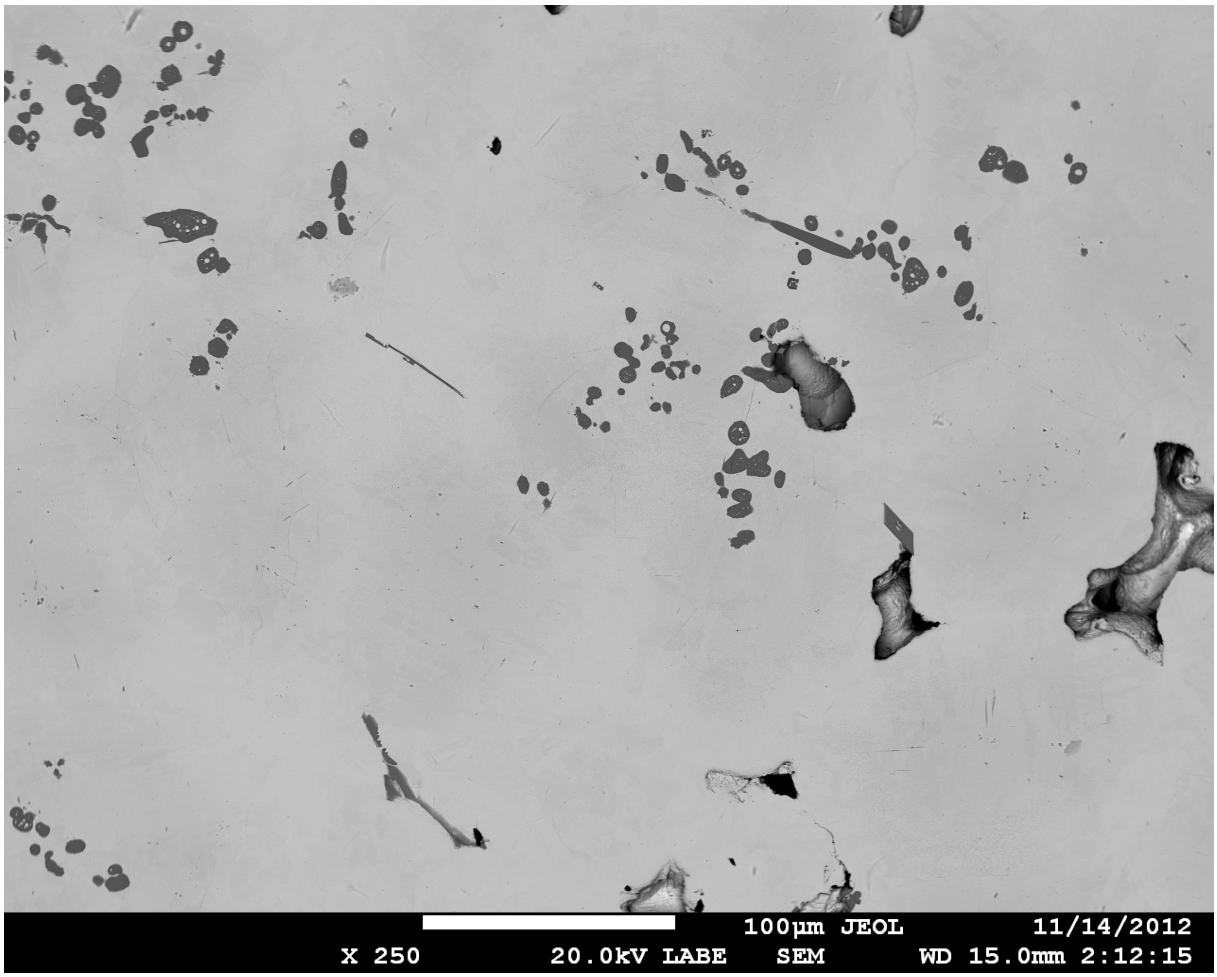

Figure 23. BSE image of porosity near the center axis of the Ra pin.

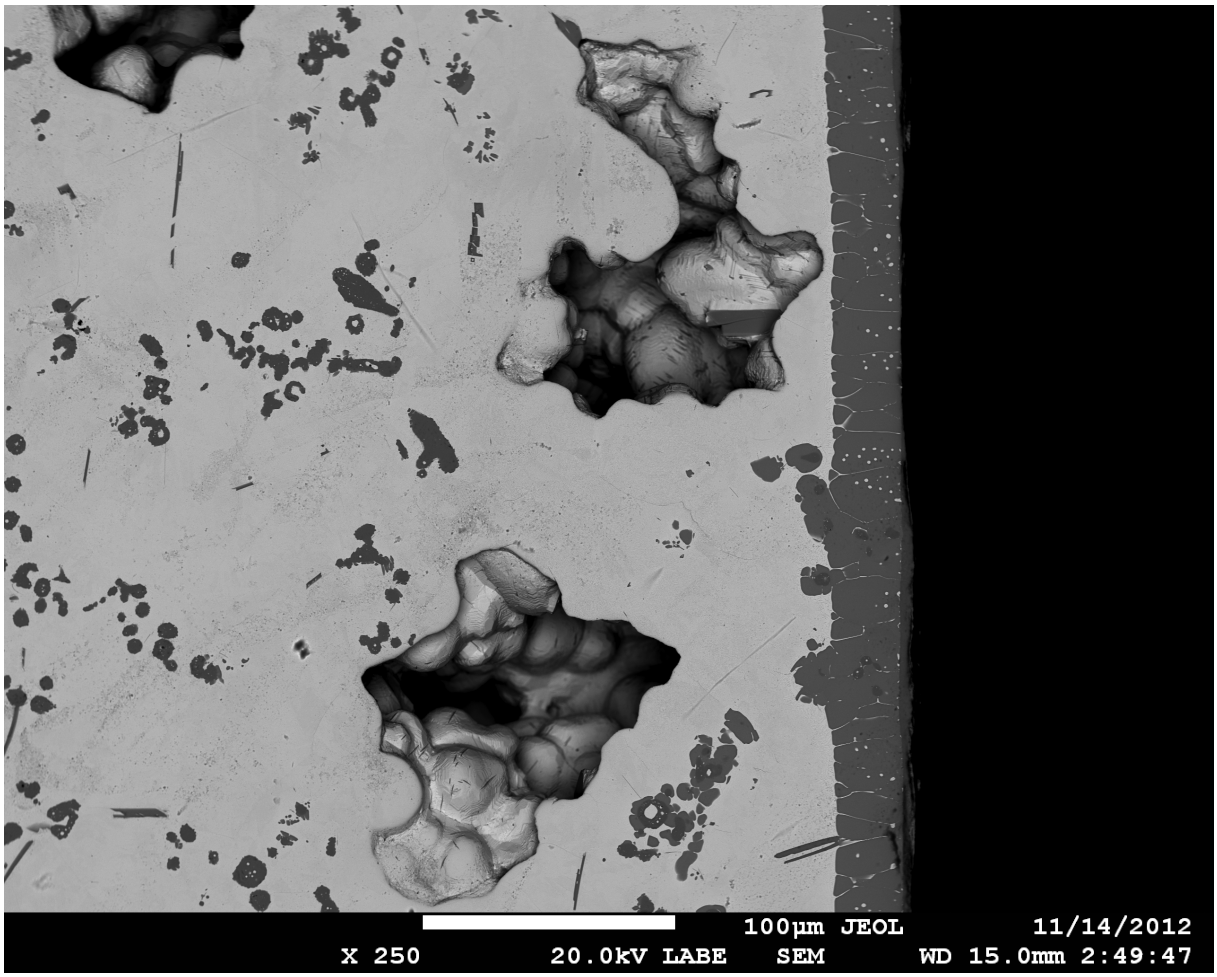

Figure 24. BSE image of porosity at the Zr rind of the Ra pin.

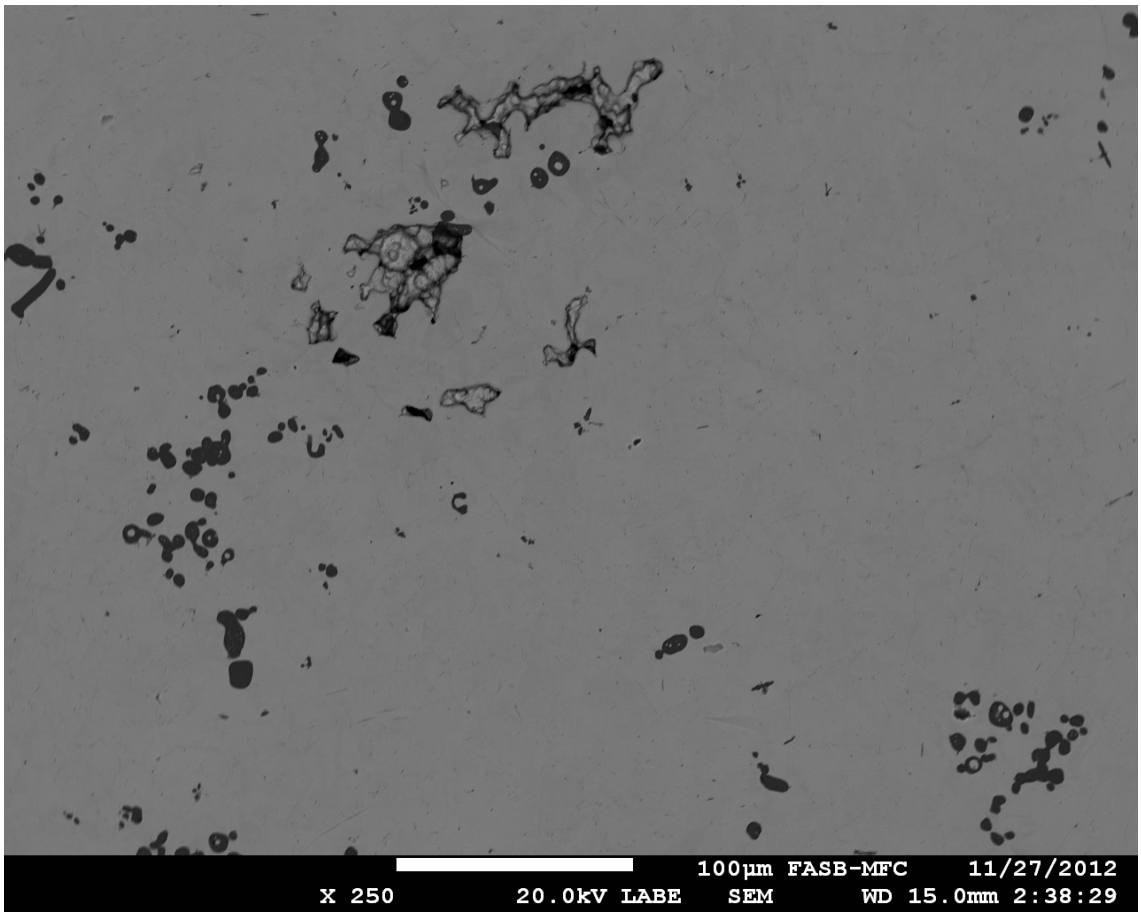

Figure 25. BSE image of porosity near the center axis of the Rb pin.

5.1.2. Rind Description

Rind structure and thickness varies significantly between EBR-II fuel specimens (see Table 11 and Figure 26). The Ra specimen has a clearly visible rind present (see Figure 26 and Figure 27). The rind consists of a Zr layer (see Section 5.2; this is actually Zr carbide; the carbon could not be measured using the EDS on the SEM), with a Zr-Si outer layer several microns thick (see Figure 27). The Rb and Rc specimens have little to no rind present. What rind is there is the Zr carbide (see Section 5.2.2). There appears to be fractured remnants of the rind near the specimen surface (see Figure 28).

The U lamellae coarsen near the interface with the Zr rind (see Figure 28). It is possible this coarsening is due to Zr migration into the Zr rind, depleting the Zr-bearing lamellae between the U layers. This apparent depletion of Zr and coarsening of the U lamellae has been observed at the interface between coarse Zr-bearing particles and the matrix throughout the specimen, including particles near the rind (see Figure 28).

Table 11. Average rind thickness in EBR-II specimens.

Specimen	Average Width [µm]	SD
Ra	33.48	5.18
Rb	2.55	1.33
Rc	1.18	0.78

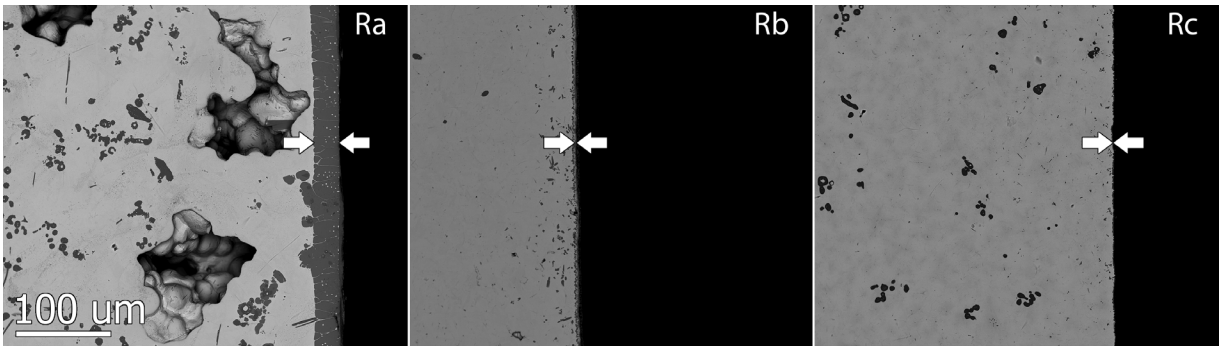

Figure 26. BSE image comparison of the Zr rind in Ra, Rb, and Rc.

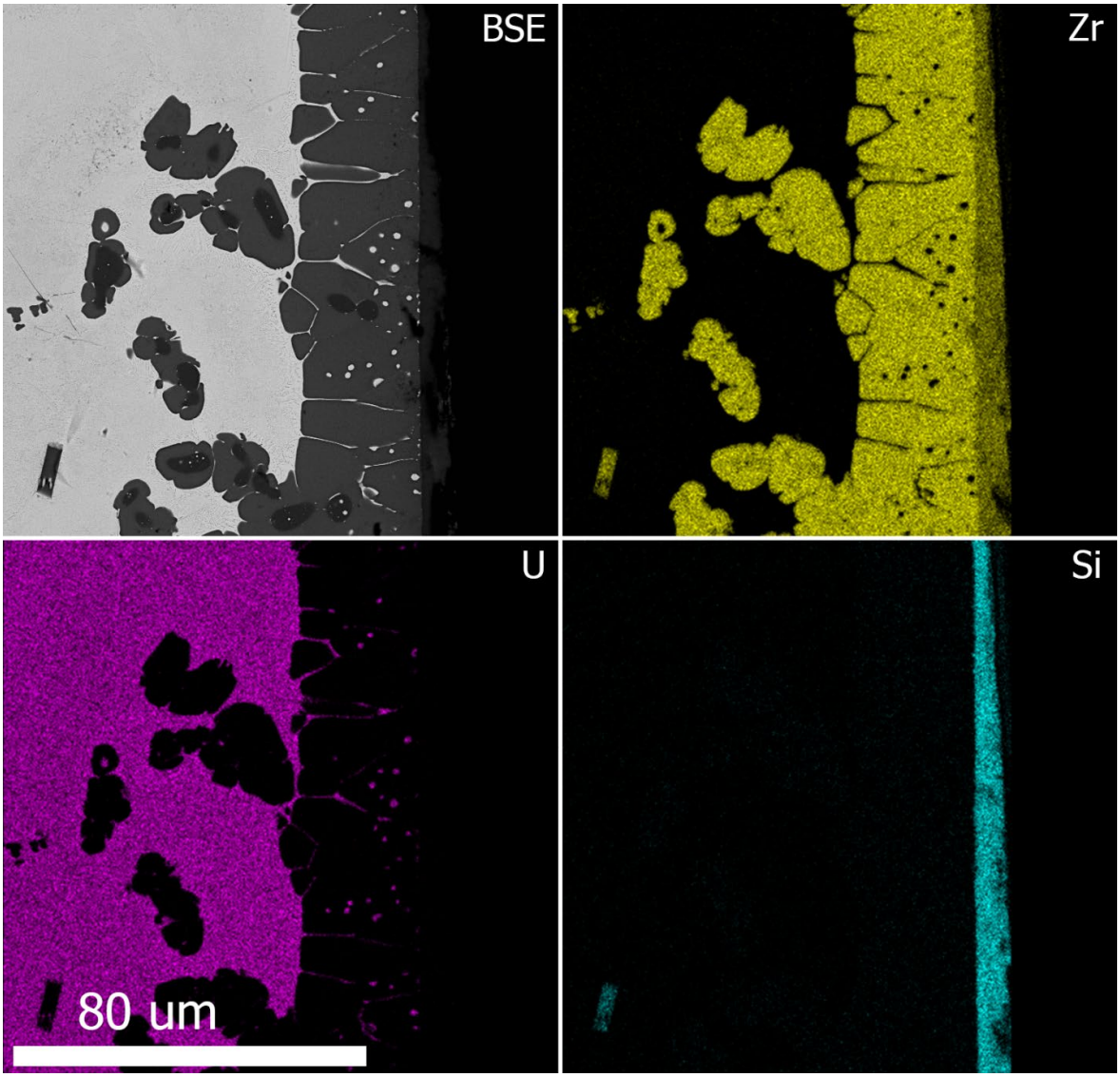

Figure 27. BSE image and U, Zr, and Si energy dispersive x-ray spectroscopy (EDS) element mapping of the Ra Zr rind.

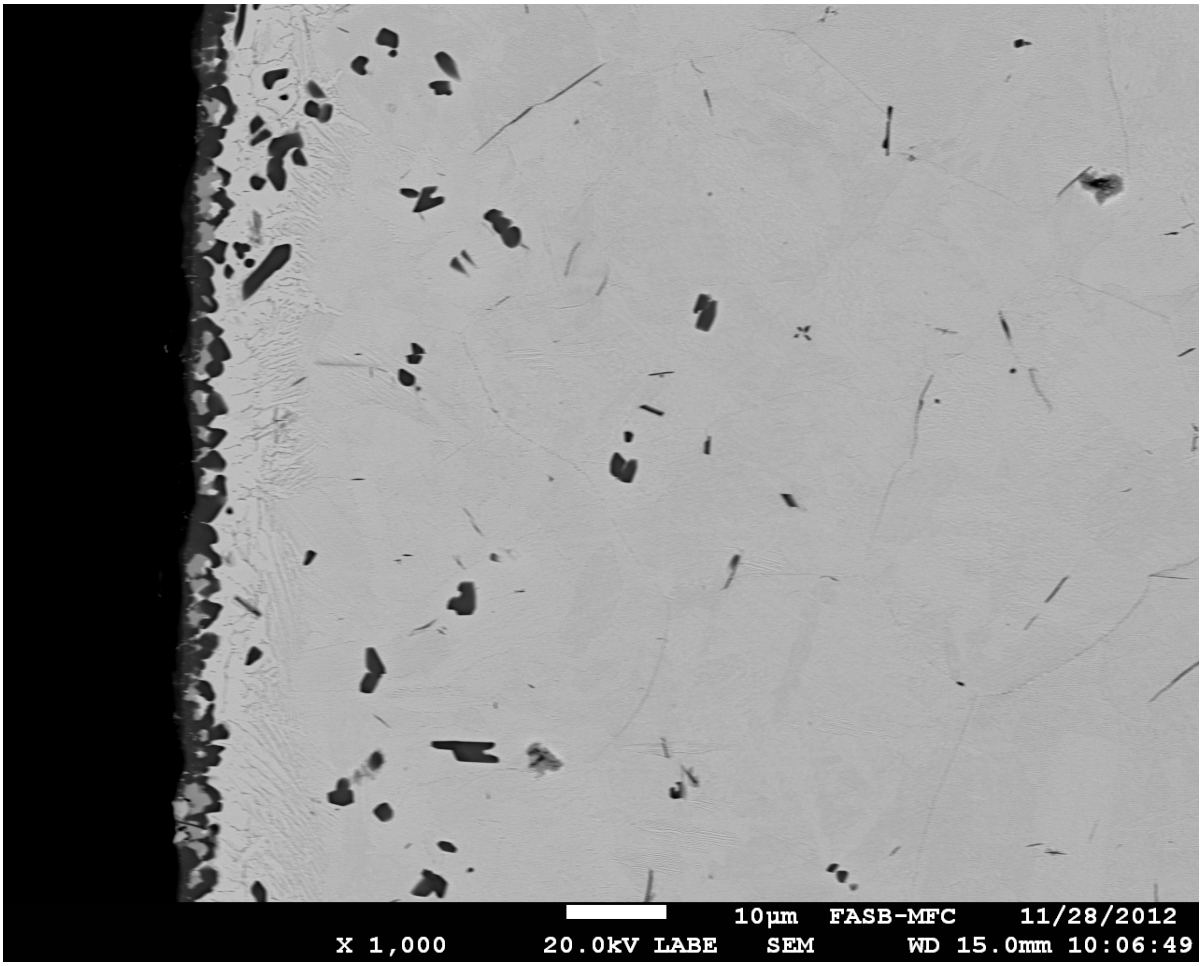

Figure 28. BSE image of the Zr rind in Rb.

5.1.3. Second Phase Particles

Particle size and fraction data was collected at 250× across the diameter (transverse cross section) at 500 µm intervals and down the length of the fuel pin central axis (longitudinal cross section), also at 500 µm intervals. No statistically significant variation in second phase particle properties as a function of radial position was observed. The bulk properties for particle size and fraction were calculated from the longitudinal images (collected at r = 0).

Images were converted to binary (black and white) files for automated quantitative analysis with ImageJ software. Care was taken to ensure the binary conversions were as accurate as possible (pixels properly assigned to either replace particles with black pixels or the matrix with white pixels). Particles were manually identified as Zr (identified as Zr carbide by EPMA) and Zr-Si based on morphology and converted to separate files for analysis (see Figure 29).

The particles observed are distinguishable by morphology and fall into two general categories: Zr particles and Zr-Si particles. The rounded, globular Zr particles are typically coarse (approximately 10 µm diameter) and cluster in groups. The coarse Zr particles frequently have U inclusions in the middle of the particle. The Zr-Si particles are either geometric (rectangular, rhombohedral, rod-like) or very long and thin and are identifiable by shape alone (confirmed by comparing with x-ray spectroscopy, see Figure 30).

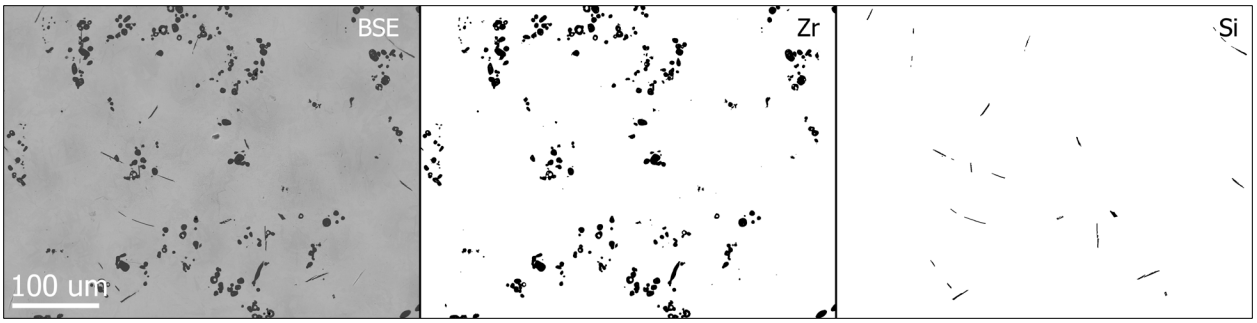

Figure 29. BSE image of particles in Ra and example binary images for identified Zr (carbide) and Zr-Si particles. Some relatively pure Zr particles are also present, along with the carbides.

The Ra EBR-II specimen has the largest Zr-type particles and highest fraction of second phase particles. Rb has slightly smaller Zr particles, on average, and a smaller fraction of particles than Ra. Rc has the smallest size and fraction of Zr particles. The particle morphology and composition appears to be uniform between all three EBR-II fuel specimens. The particle size and fraction data are summarized in Table 12. Variation in particle size and fraction are illustrated graphically in Figure 31 and Figure 32, respectively.

Table 12. Summary of second phase particle data.

Specimen	Particle Type	Average Size (µm2)	SD	Area Fraction (%)	SD
Ra	Total Zr-type	28.97	3.58	4.30	0.81
	Si-Zr	9.35	3.64	0.12	0.06
Rb	Total Zr-type	24.19	7.72	1.85	0.82
	Si-Zr	3.31	1.91	0.01	0.00
Rc	Total Zr-type	12.70	7.07	0.57	0.37
	Si-Zr	N/A	—	N/A	—

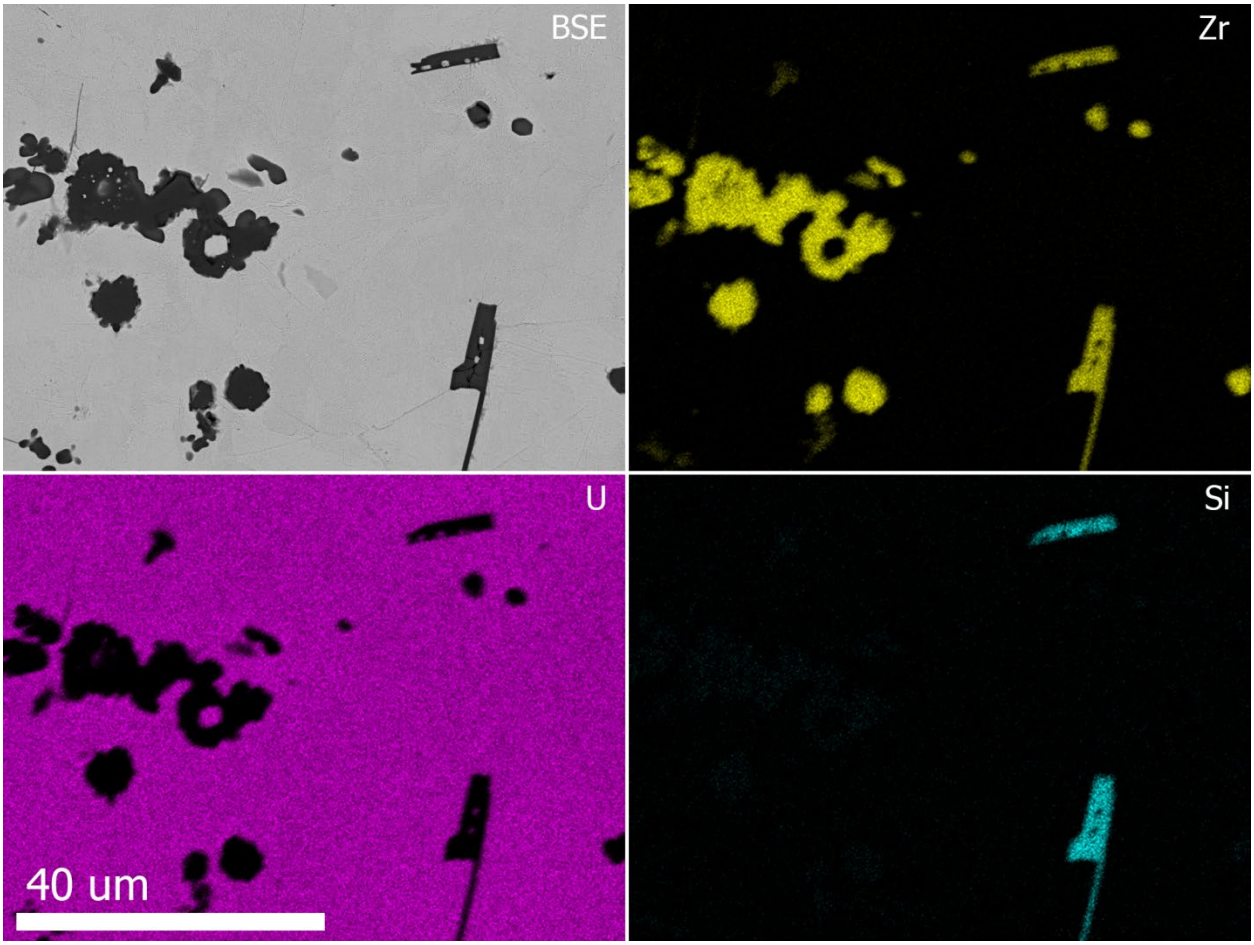

Figure 30. BSE image and U, Zr, and Si EDS element mapping of coarse, globular Zr (or Zr carbide) and Zr-Si particles in Ra.

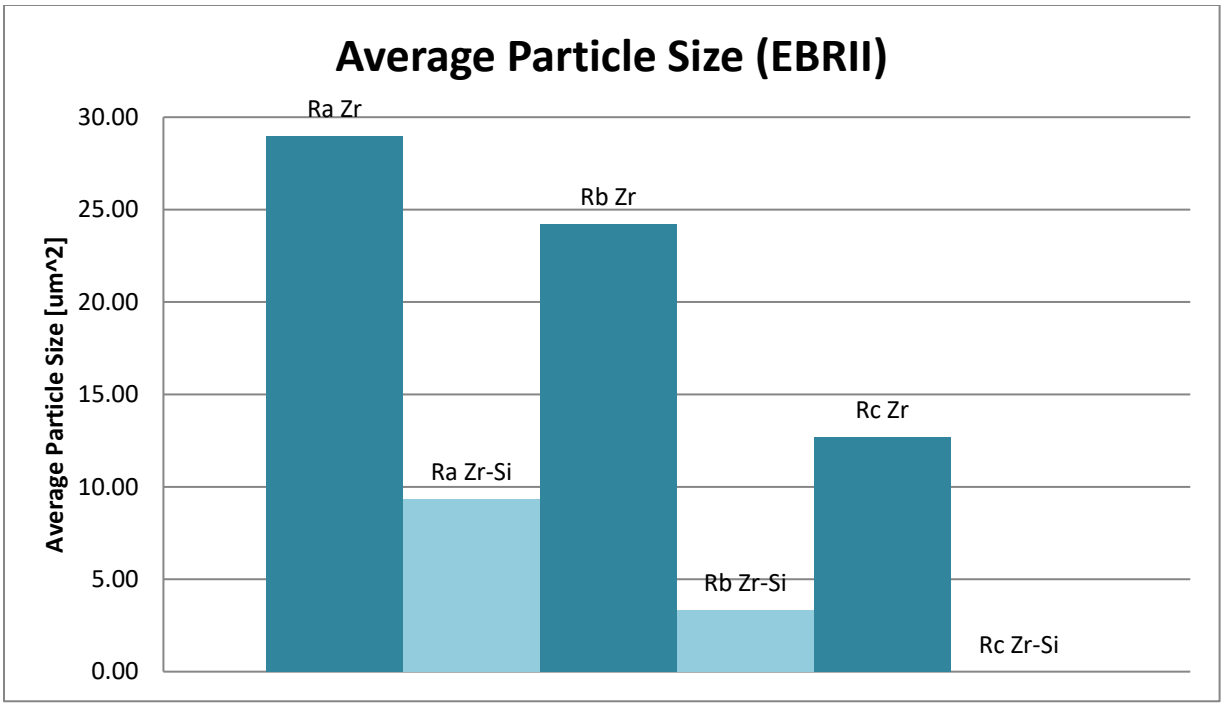

Figure 31. Average second phase particle size of Zr and Zr carbides, identified by SEM as Zr, and Zr-Si particles in Ra, Rb, and Rc EBR-II specimens. Henceforth, in the SEM section, the Zr is actually a mixture of Zr carbides and some Zr particles, called Zr-type.

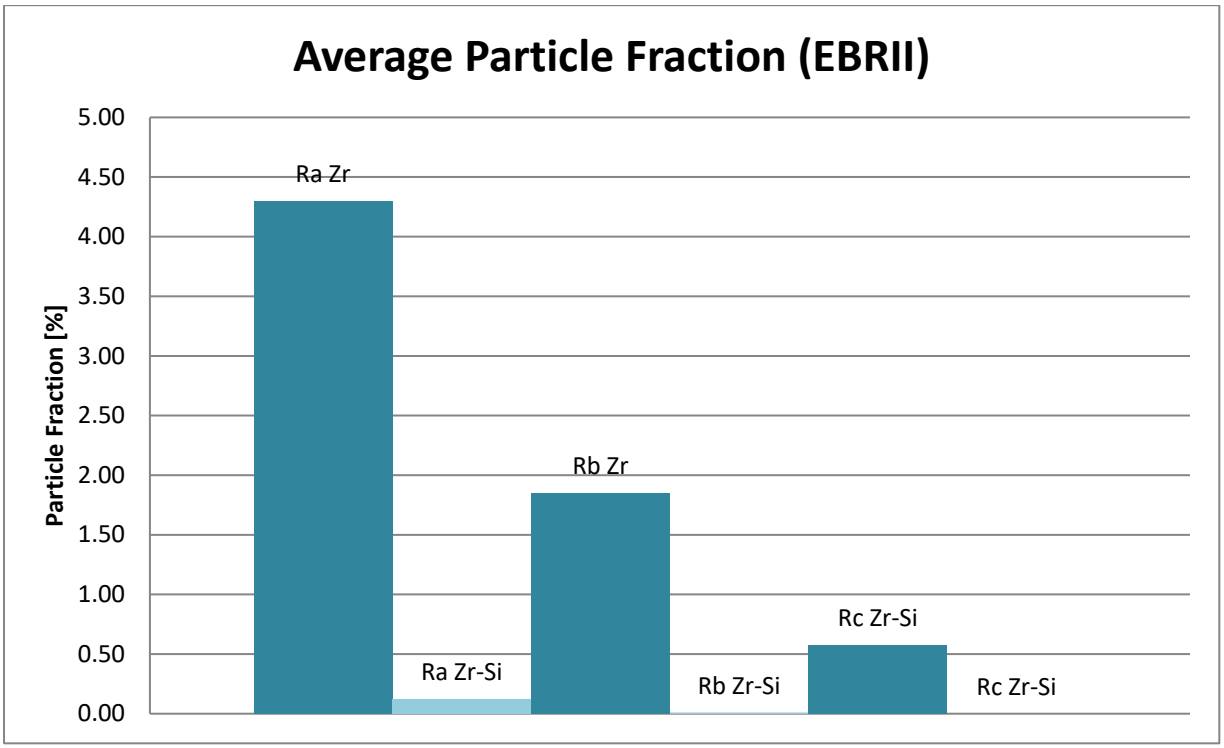

Figure 32. Average second phase particle fraction (area fraction) of Zr-type and Zr-Si particles in Ra, Rb, and Rc EBR-II specimens.

5.1.3.1. Ra (5% length from spade end)

Second phase particles in Ra are primarily rounded globular Zr-type particles with frequent U inclusions. These coarser particles are present in clusters. Rod-like and other geometrically shaped Zr-Si particles are also present (see Figure 33).

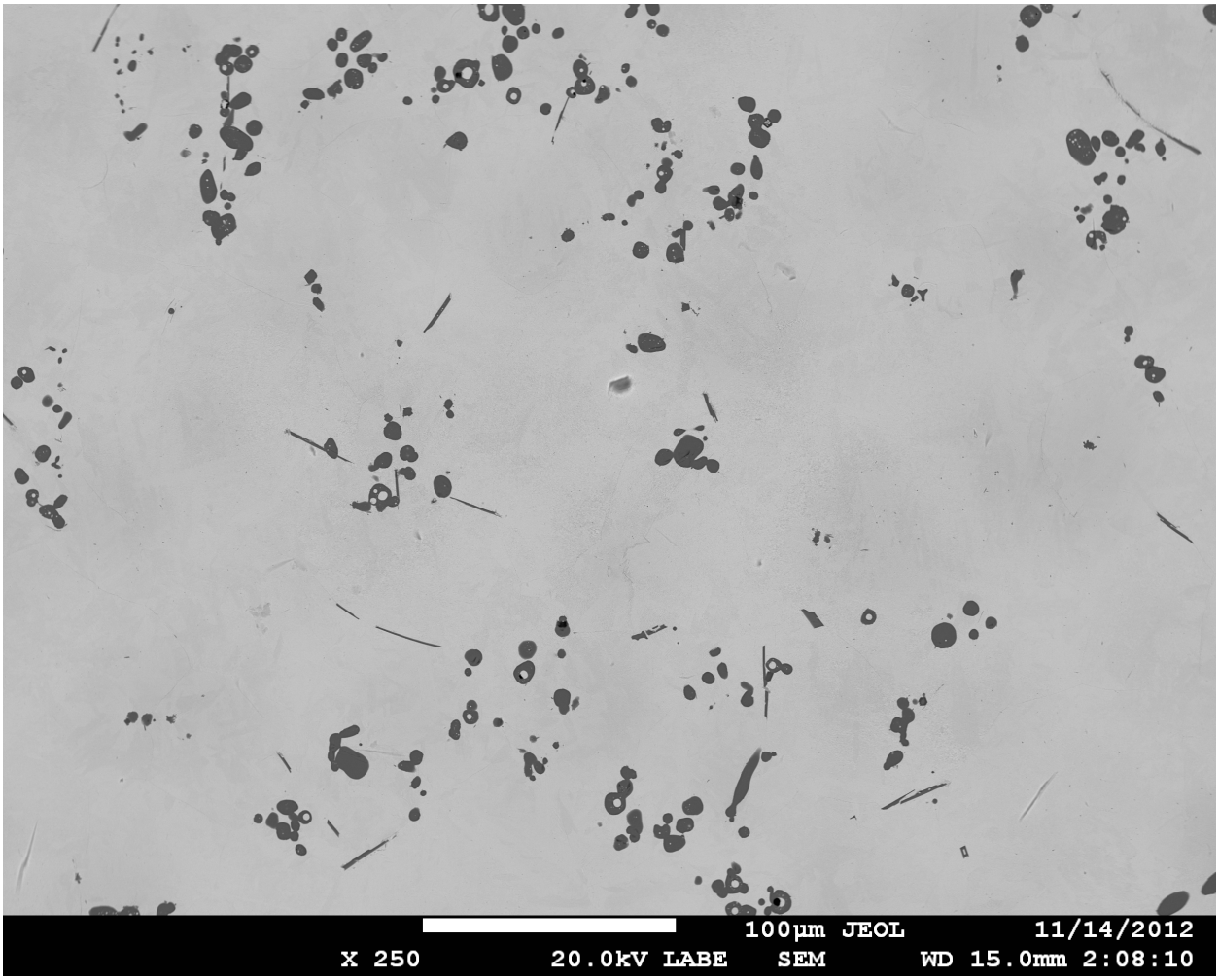

Figure 33. BSE image of second phase particles in Ra.

5.1.3.2. Rb (50% length from spade end)

Globular Zr-type particles in Rb are similar in size to those in Ra and appear in clusters, but with less than half the fraction present in Ra. Like Ra, inclusions of U in the Zr-type particles are common. Very few Zr-Si particles are present (see Figure 34).

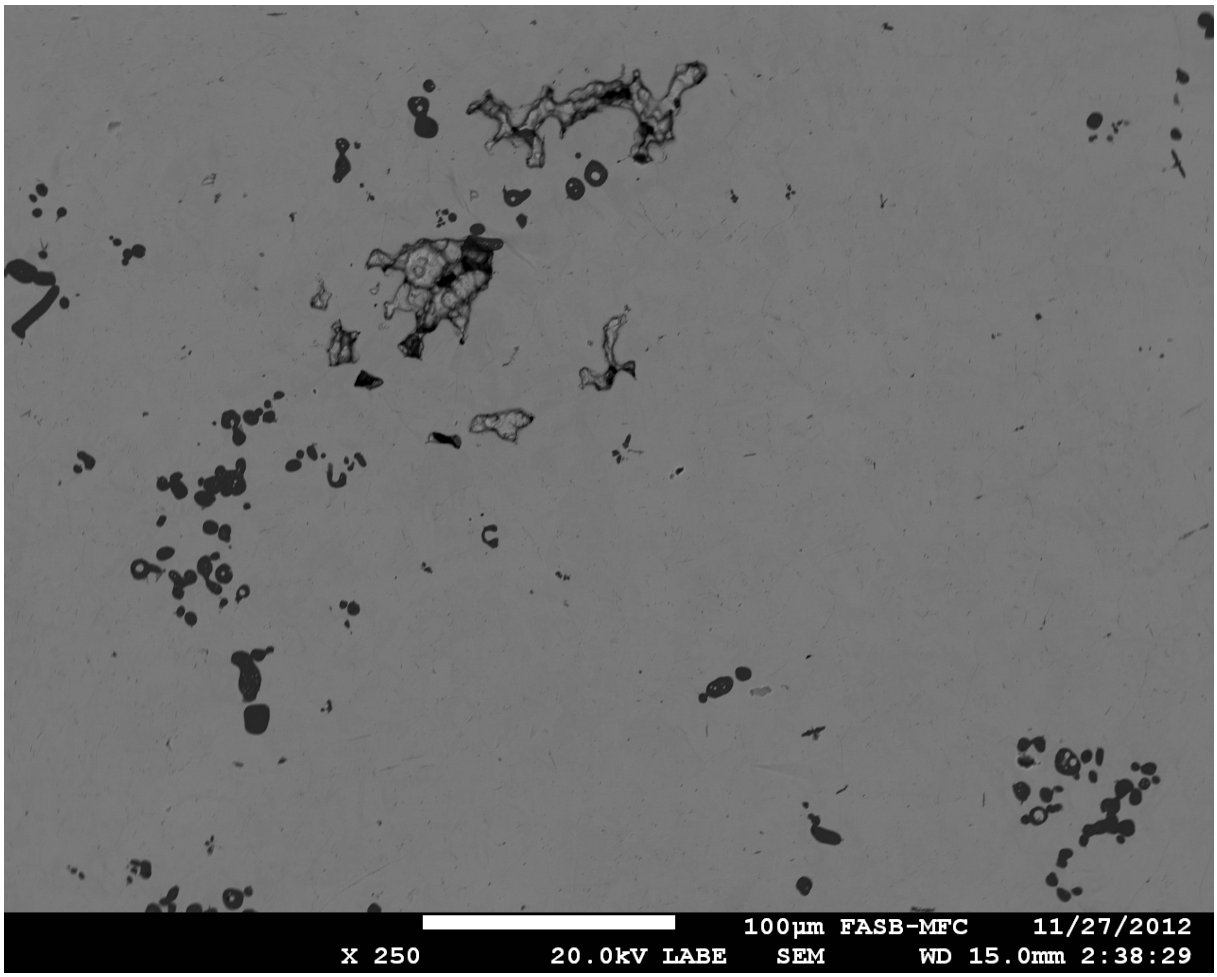

Figure 34. BSE image of second phase particles in Rb.

5.1.3.3. Rc (95% length from spade end)

The average Zr-type particle size in Rc is smaller than both Ra and Rb (approximately half the average area) and the fraction of particles is less than Rb (see Table 12 and Figure 35). In the particles present, U inclusions are present. There are very few fine Zr-type particles. Those that are present appear to have regions of Zr concentration immediately around the particles (see Figure 36). This gradient corresponds to the dark and light contrast in the matrix (see Figure 35); however, very few fine particles are present. This gradient of Zr in the matrix does not appear around the coarse, globular particles (see Figure 37). There are no Zr-Si particles present.

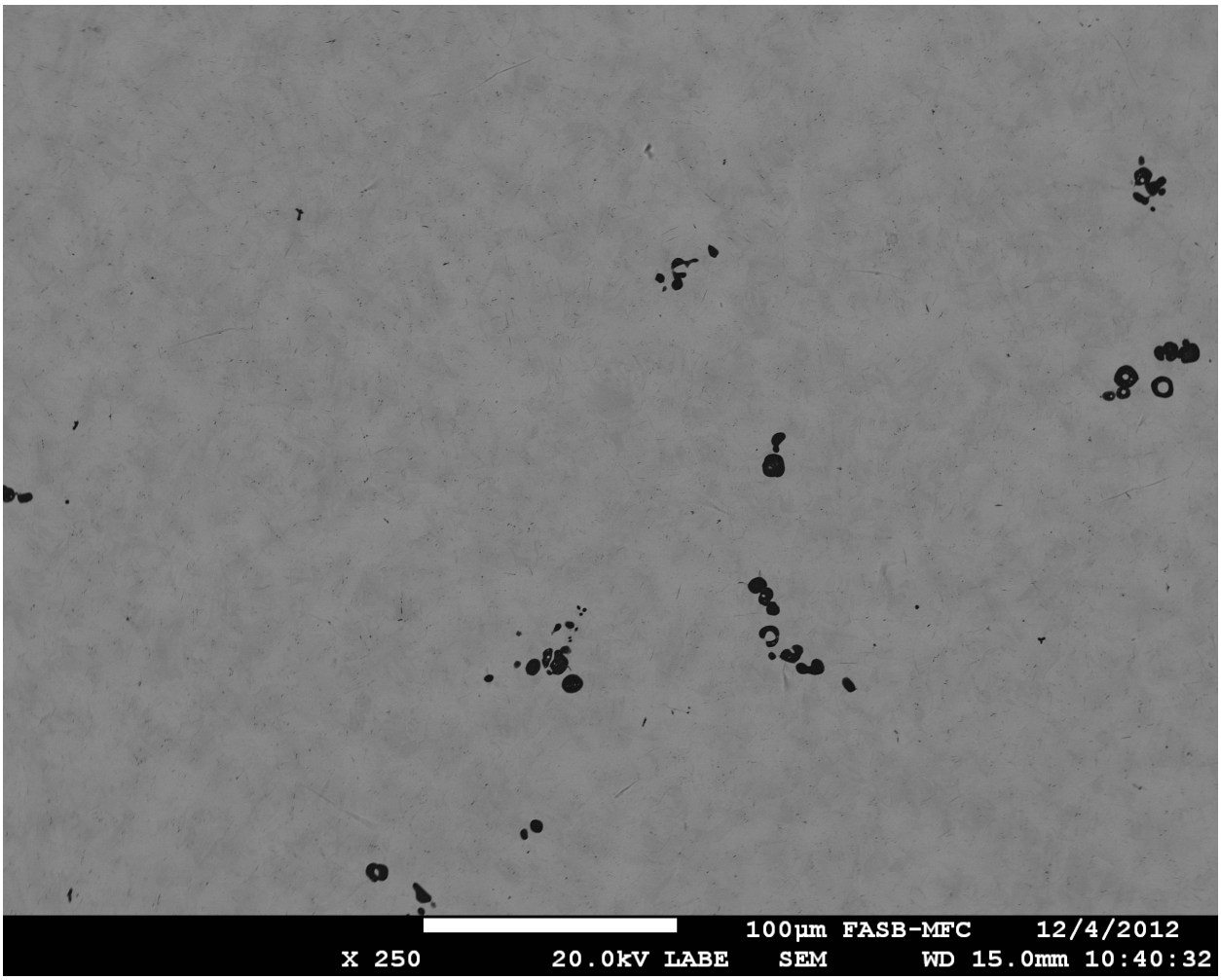

Figure 35. BSE image of second phase particles in Rc.

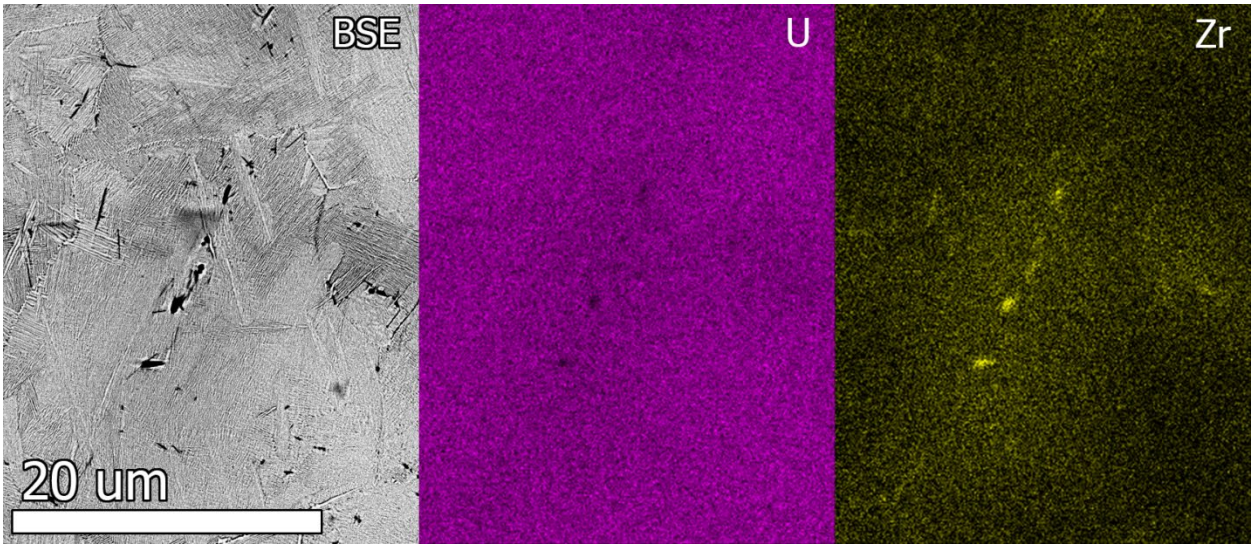

Figure 36. BSE image and U and Zr EDS element mapping of fine Zr-type particles and the surrounding matrix in Rc.

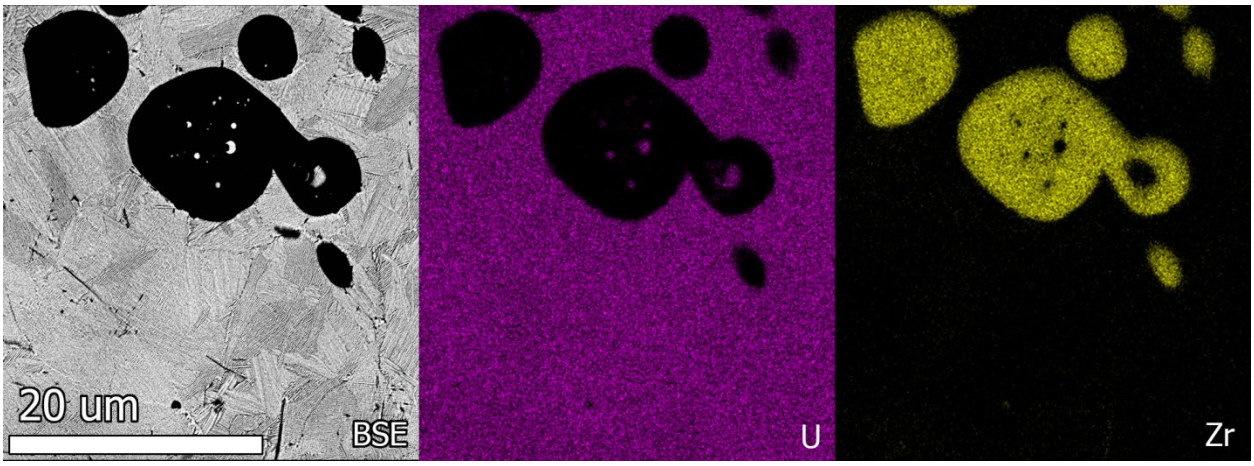

Figure 37. BSE image and U and Zr EDS element mapping of coarse Zr-type particles and the surrounding matrix in Rc.

5.2. Chemical and Phase Composition (EPMA)

One purpose of the EPMA characterization is to identify the nature (carbide, silicide, etc.) of the 'rind' layers or of the particles/precipitates using EPMA methods where carbon, etc. could also be measured. This enhances the analysis done with SEM.

Samples were analyzed on a Cameca SX-100R electron probe microanalyzer (EPMA) after being coated with a 15 nm layer of aluminum. Until the analysis, samples were stored under an argon atmosphere. Samples were analyzed on the EPMA using Probe for EPMA v. 8.86 for quantitative analysis and PeakSight for gathering x-ray maps. Each quantitative point was measured at 15 kV and 20 nA with a focused beam. Peaks were measured for 30 seconds while backgrounds were counted for 20 seconds. The mass absorption coefficients employed were those of Chantler et al. (2005), while phi-rho-z corrections used were those of Love and Scott (1978). X-ray maps generally employed a beam raster, with an integration time of 80 ms. Additional analytical parameters are shown in Table 13.

Table 13. X-ray lines, standards and crystals used in EPMA analysis.

Element	Line	Standard	Crystal
Si	kα	SiC	TAP
U	mβ	U	PET
Zr	lα	Zr	PET
C	kα	SiC	PC2

Where practical, two perpendicular radial traverses were measured on the transverse section, as shown in Figure 38, and one center, one edge, and three rim traverses were measured on the longitudinal section. In addition, features of interest were measured.

5.2.1. Data Quality

For ease of interpretation, quantitative data in figures is generally presented in atomic percent; however, the data is collected in weight percent. All measurements made in weight percent are contained in separate project files so that the quality of the data can be evaluated. In general, the weight percent total of all analytes should be expected to be in the range of 98%–102%. Summations far outside this range should be considered inaccurate. Several reasons exist for inaccurate data, including not all elements are measured, irregular topography, and matrix corrections or mass absorption coefficients that are a poor match for the matrix.

There is a possibility that oxygen could be a minor element in some phases or locations within a sample. However, because samples could not be completely isolated from oxygen, it cannot be readily determined whether measured oxygen is on the surface or incorporated within the material.

With regard to matrix corrections, in most instances, the Love–Scott (1978) correction yielded reasonable results. However, when both Zr and U were in high concentrations, this correction algorithm tended to yield very high analytical totals (i.e., >105 wt%). Such analytical results should be approached with caution. Similarly, very low analytical totals were observed in very high carbon areas.

5.2.2. Results

5.2.2.1. Radial Transverses

A grid of approximately 60 quantitative spots (in the form of three rows of 20 each) was set up for each radial traverse. The analyses of each of three to four adjacent spots (see Figure 38) were averaged across the traverse to obtain an average compositional gradient across the radius of the sample. Results are shown in Figure 39.

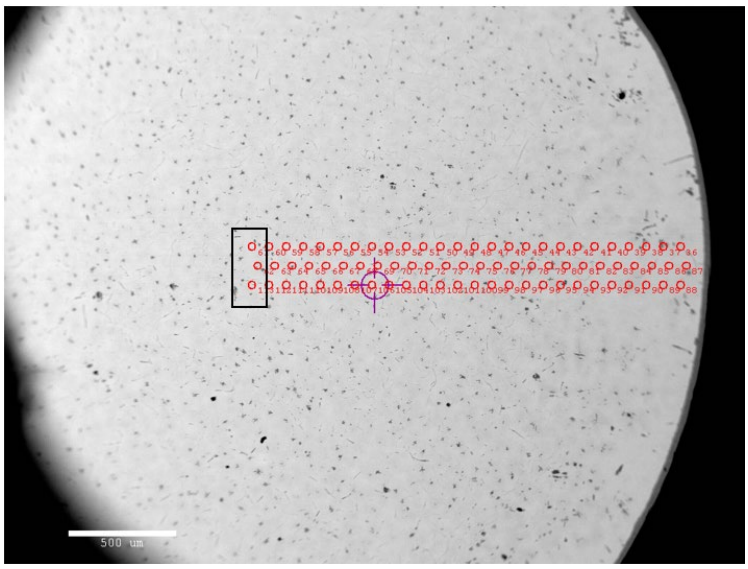

Figure 38. Radial traverse analysis map for EBR-II sample Ra. The box illustrates the three points that were averaged to form a single compositional point. Similar averaging took place across the radius.

Several observations can be made concerning the data in Figure 39. Firstly, there is no significant compositional difference between the horizontal and vertical radial traverses within any given sample. Secondly, with respect to samples Rb and Rc, there is very little compositional difference or variation from the center toward the rim; however, this is not the case with sample Ra. Sample Ra shows variation in U content from approximately 48 to 80 at%, compensated primarily by changes in Zr content (Figure 39, a and b). Such variations do not appear to be systematic and are likely dominated by Zr-rich phases common in this sample. Silicon is generally in very low concentrations (<<1 at%) in all three samples, except in sample Ra when the traverse crosses a Si-rich phase. While carbon was not measured in sample Rb, it was measured in samples Ra and Rc. Carbon content in transverse samples Ra and Rc averages approximately 5 and 13 at%, respectively. Since carbon was not measured in sample Rb, the normalization process necessary to create atomic percents will exaggerate the concentration of U and Zr in that sample.

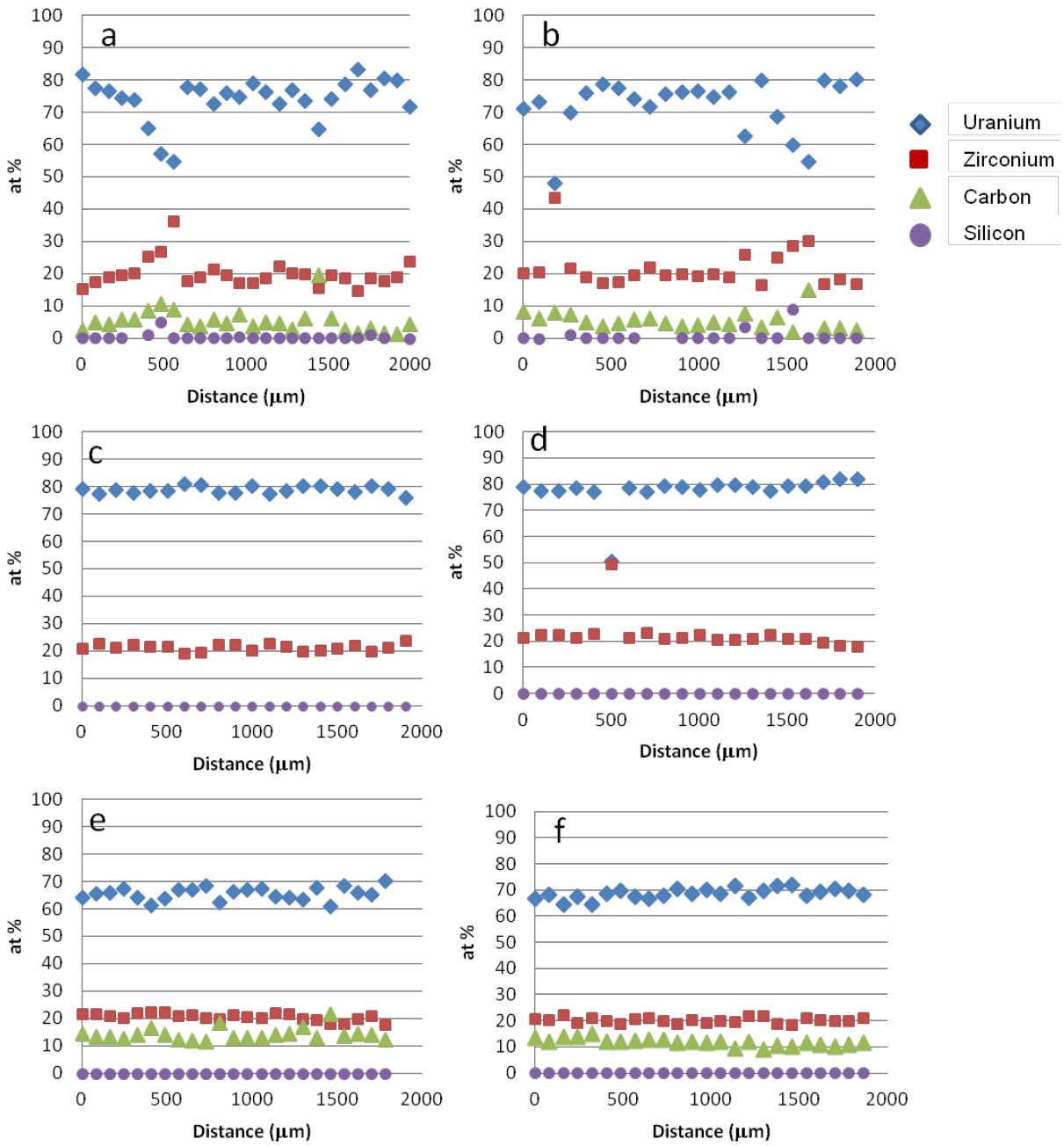

Figure 39. The compositional variability across the radius of transverse samples from the center toward the rim: (a and b) EBR-II Ra horizontal and vertical traverse, (c and d) EBR-II Rb horizontal and vertical traverse, and (e and f) EBR-II Rc horizontal and vertical traverse.

5.2.2.2. Longitudinal Traverses

Results of compositional traverses along the long axis of longitudinal samples Ra, Rb, and Rc are shown in Figure 40. These compositional points were not averaged but rather represent individual locations 40–80 µm apart. Note that carbon was not measured in sample Rb due to an unknown interference with carbon that was later discovered to be U $N_{IV}O_{IV}$ and subsequently corrected in later analyses. As a result of not measuring carbon in Rb, atomic percentages of measured elements are artificially elevated in that sample.

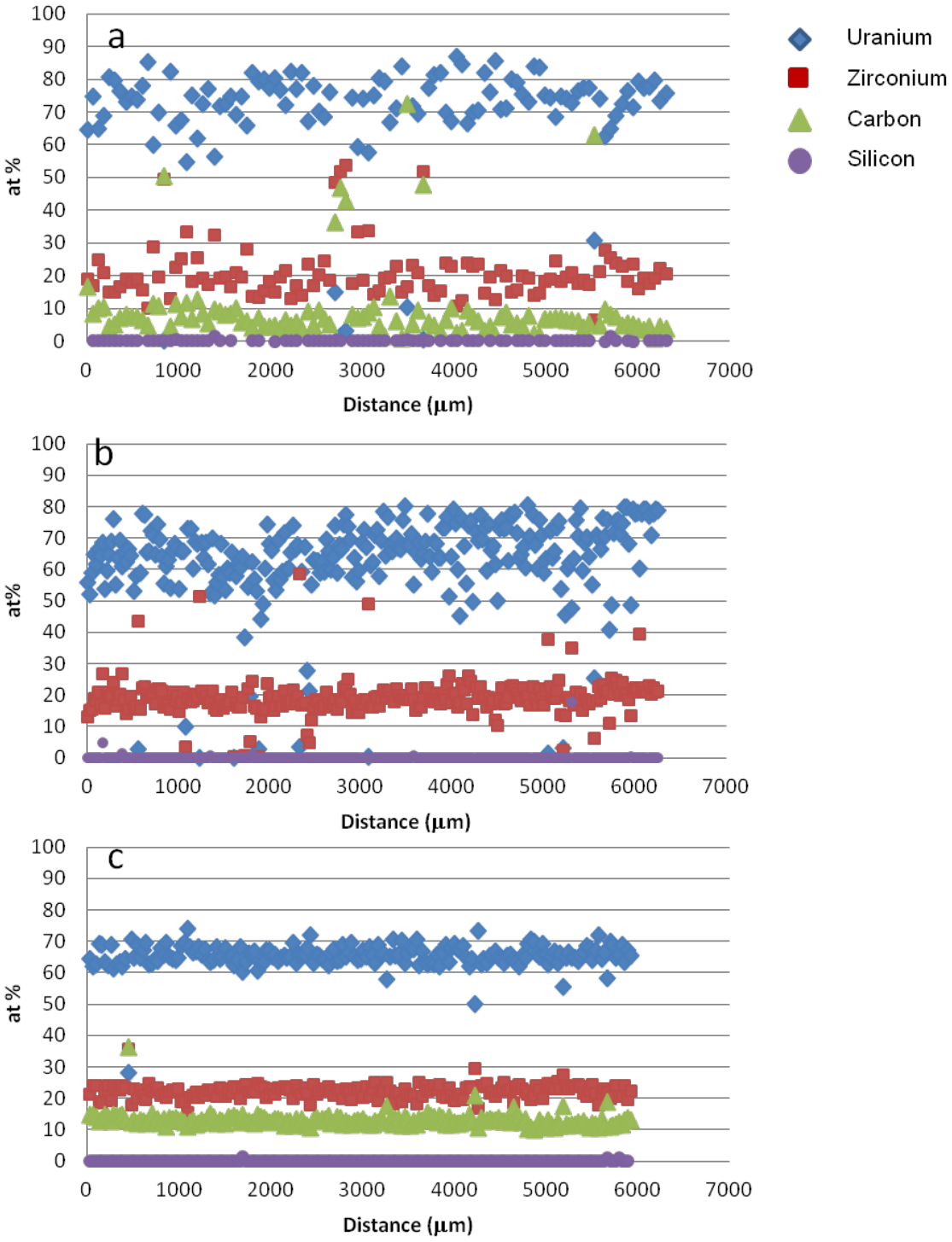

Figure 40. Traverses down the center (long) axis of longitudinal specimens: (a) Ra, (b) Rb, and (c) Rc.

Major element variation is considerably greater in Ra than in Rb or Rc. The one-sigma standard deviation for U at% concentration in Ra is 17.7, whereas it is 11.3 for Rb and 4.0 for Rc. Trends for Zr variation are similar. If the casting is viewed as a continuous process and the rod composition is considered in its entirety, we can see that average U concentration is relatively elevated toward the spade while Zr and C concentrations are consequently depressed. As distance from the spade increases, U concentration decreases while Zr and C increase (see Figure 41).

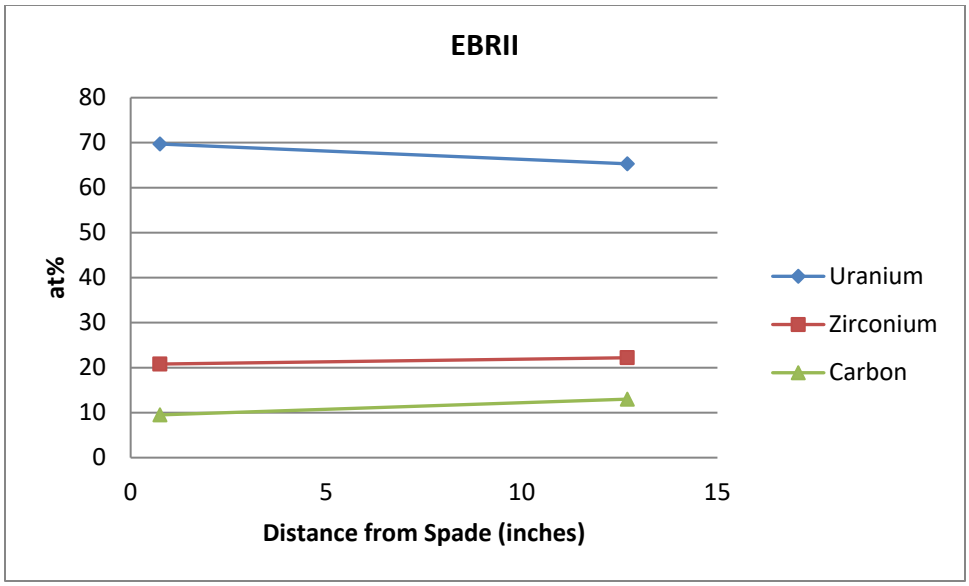

Figure 41. Average atomic percent concentration of U, Zr, and C as a function of distance from the spade. Two-sigma analytical error bars are smaller than the symbol.

5.2.2.3. Rim Chemistry

Examples of rim geometry and chemical variations exhibited in transverse-mounted samples are shown in Figure 42. As can be seen in Figure 42, sample Ra has a rim approximately 40 μm thick, while sample Rb and Rc have a much thinner rim at ~5 and ~2 μm, respectively. Much of the outer 10–15 μm perimeter of sample Ra consists of material with a composition of ZrSi. Inward of the outer perimeter is a 25–30-μm-thick zone composed of Zr_xC, where X varies between 5 and 6. Sample Rb's rim consists of material with a composition of ZrC, while sample Rc's outer perimeter is characteristic of gradual diffusion toward the surrounding epoxy material (Figure 42 c). Similar rim morphology and chemistry for all three samples can be seen in the longitudinally mounted sections.

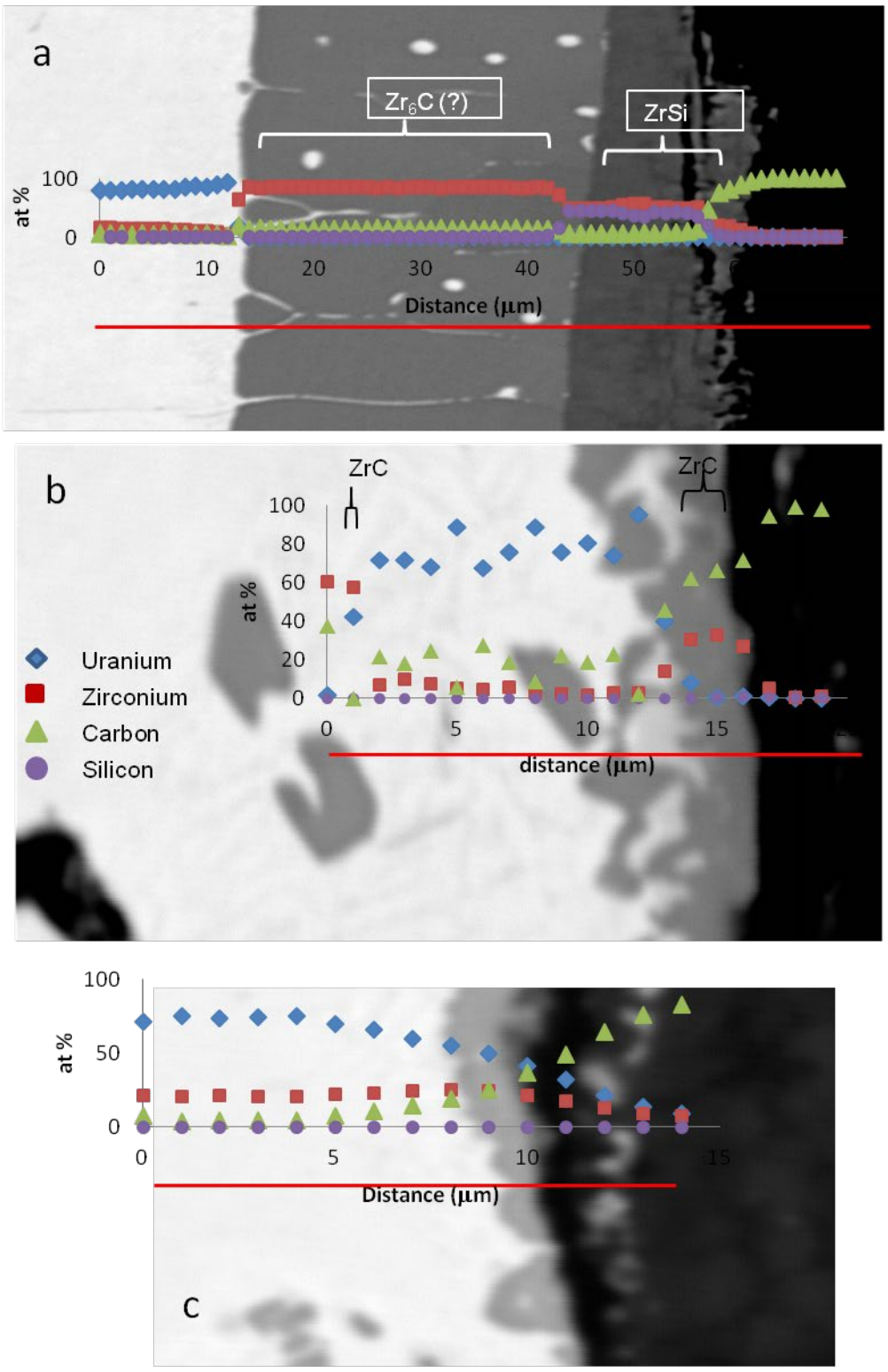

Figure 42. Shows rim geometry and composition for the rims of (a) Ra, (b) Rb, and (c) Rc (transverse mounts).

5.2.2.4. *Phase Morphologies and Compositions*

Several different phase compositions and morphologies appear in EBR-II fuel samples. Sample Ra contains abundant euhedral (well-faceted) tabular to equiaxed crystals whose composition is consistent with Zr_2Si (Figure 43, Table 14). These crystals are generally 5–20 µm along the longest dimension, but in some cases can be up to 70 µm (Figure 44). Crystals are often present along apparent grain boundaries but can also occur within grains (Figure 43). They frequently exhibit a skeletal texture, with openings subparallel to crystal faces (Figure 44).

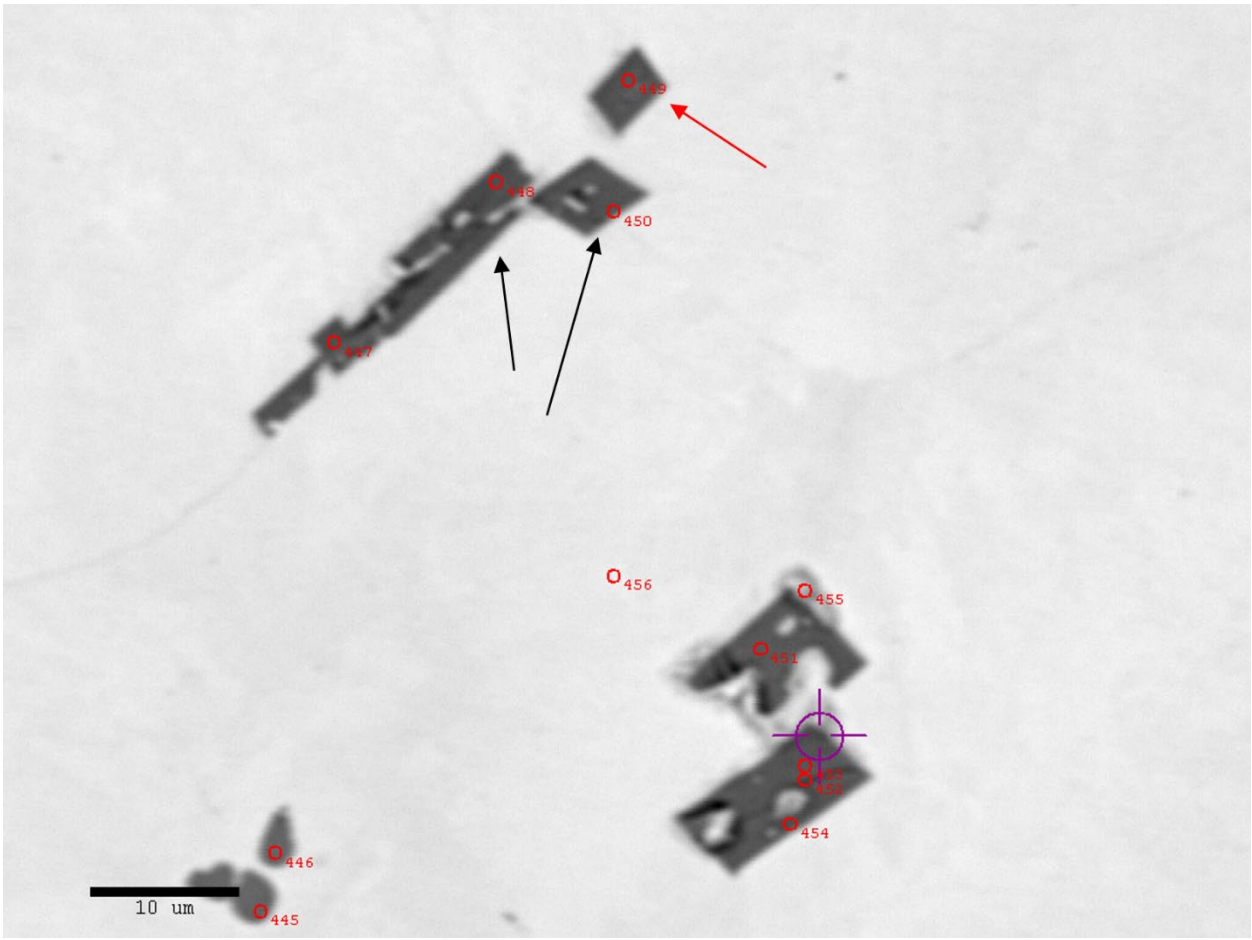

Figure 43. Ra transverse sample showing euhedral crystals composed of Zr_2Si with skeletal texture growing along apparent grain boundaries (black arrows) and within grains (red arrow). Analyzed locations are indicated by number. Analyses appear in Table 14.

Table 14. Quantitative analyses of spots shown in Figure 43.

Spot	Si at%	U at%	Zr at%	C at%	Possible Phase ID
445	0.00	0.58	88.8	10.6	—
446	0.01	1.96	88.4	9.63	—
447	29.9	0.40	62.8	6.91	Zr_2Si
448	29.2	0.51	63.5	6.84	Zr_2Si
449	26.2	4.40	55.8	13.6	Zr_2Si
450	28.8	1.17	63.4	6.64	Zr_2Si
451	29.8	0.61	62.8	6.83	Zr_2Si

452	29.3	0.33	63.1	7.21	Zr_2Si
453	29.4	0.23	62.6	7.80	Zr_2Si
454	11.2	26.7	20.3	41.8	—
455	1.38	76.7	15.3	6.61	—
456	0.00	75.5	16.3	8.21	—

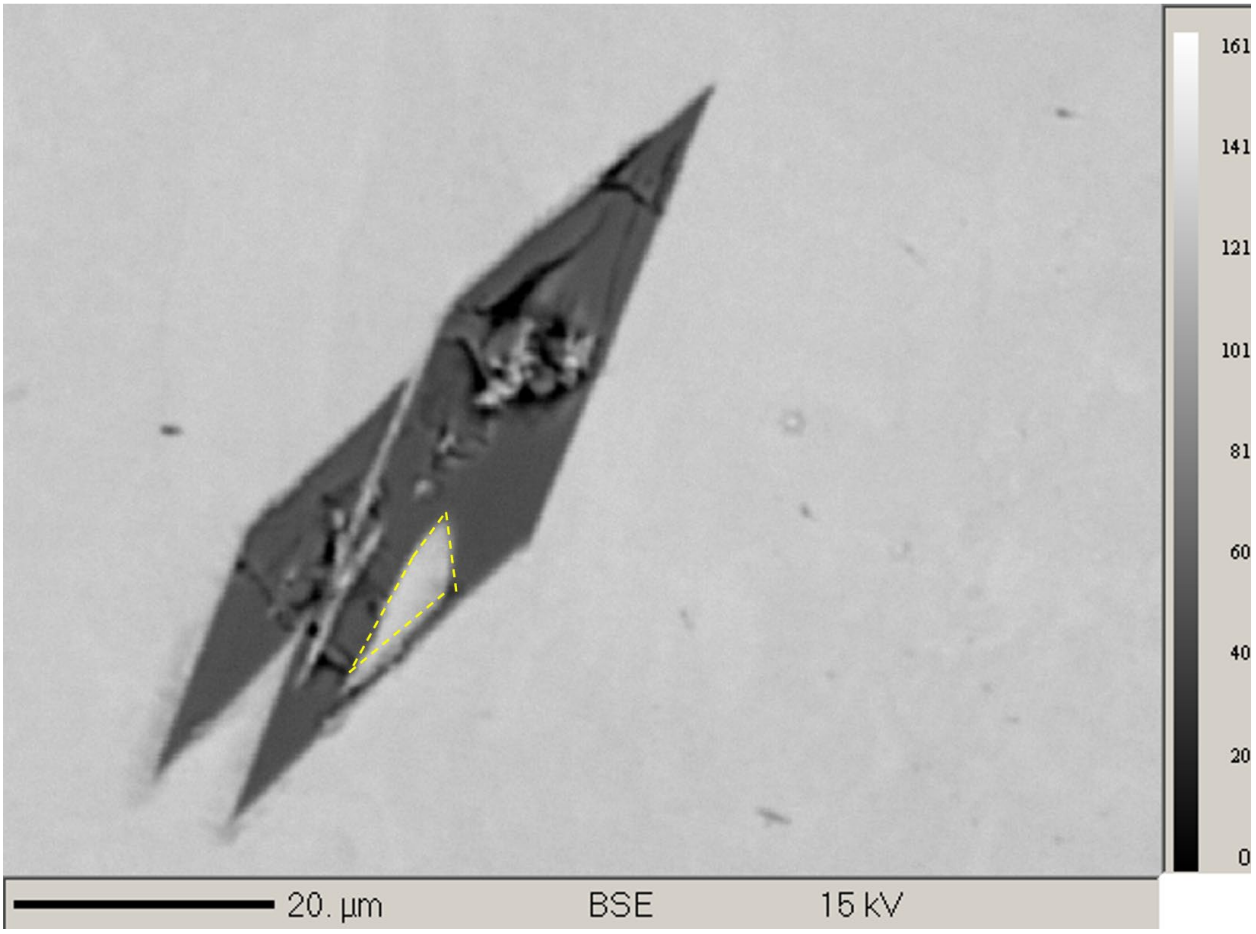

Figure 44. Ra round euhedral crystal approximately 70 mm in longest dimension. Dashed yellow outline shows skeletal growth with void faces subparallel to crystal faces.

Subhedral to anhedral (semifaceted to unfaceted) crystals occur in all samples. In general, these phases are <20 µm in the longest dimension but tend to be increasingly smaller with increasing distance from the spade. Several examples are shown in Figure 45 through Figure 47. Figure 45 shows equiaxed and acicular crystals present in sample Rb (transverse mount). In general, the equiaxed grains compositionally resemble ZrC, while the acicular grains are silicon-rich (see Table 15). Due to their small size, an accurate analysis with microprobe is not possible.

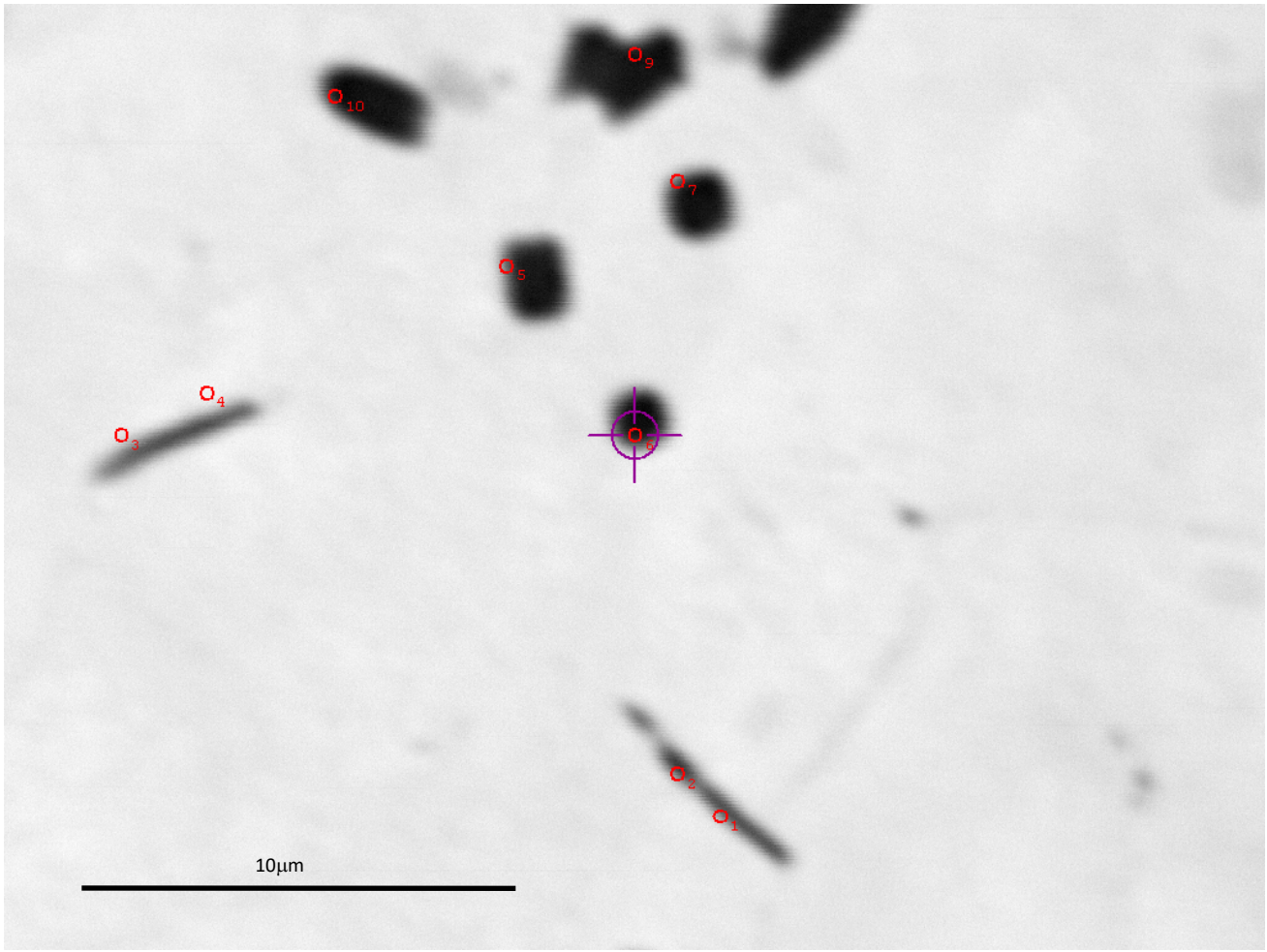

Figure 45. Rb transverse acicular and equiaxed phases. Analyses shown in Table 15.

Table 15. Quantitative analyses of spots shown in Figure 45.

Spot	U at%	Zr at%	Si at%	C at%	Possible Phase ID
1	25.7	35.6	12.1	26.6	—
2	20.1	40.5	15.2	24.2	—
3	28.8	36.0	14.8	20.4	—
4	24.8	32.8	13.6	28.8	—
5	13.2	43.7	0.00	43.3	—
6	5.33	44.3	0.01	50.3	ZrC
7	1.59	44.4	0.00	54.0	ZrC
8	7.55	42.0	0.00	50.5	ZrC
9	4.42	42.2	0.03	53.4	ZrC
10	5.97	45.9	0.00	48.2	ZrC

Figure 46 (a–e) shows an extended linear feature in sample Rb (transverse). While this was not analyzed with quantitative spots, x-ray maps suggest it consists of ZrC (see Appendix A). Additional anhedral, equiaxed grains can

be seen in sample Rc (transverse) in Figure 47. Quantitative analyses show that these grains are compositionally consistent with ZrC (see Table 16).

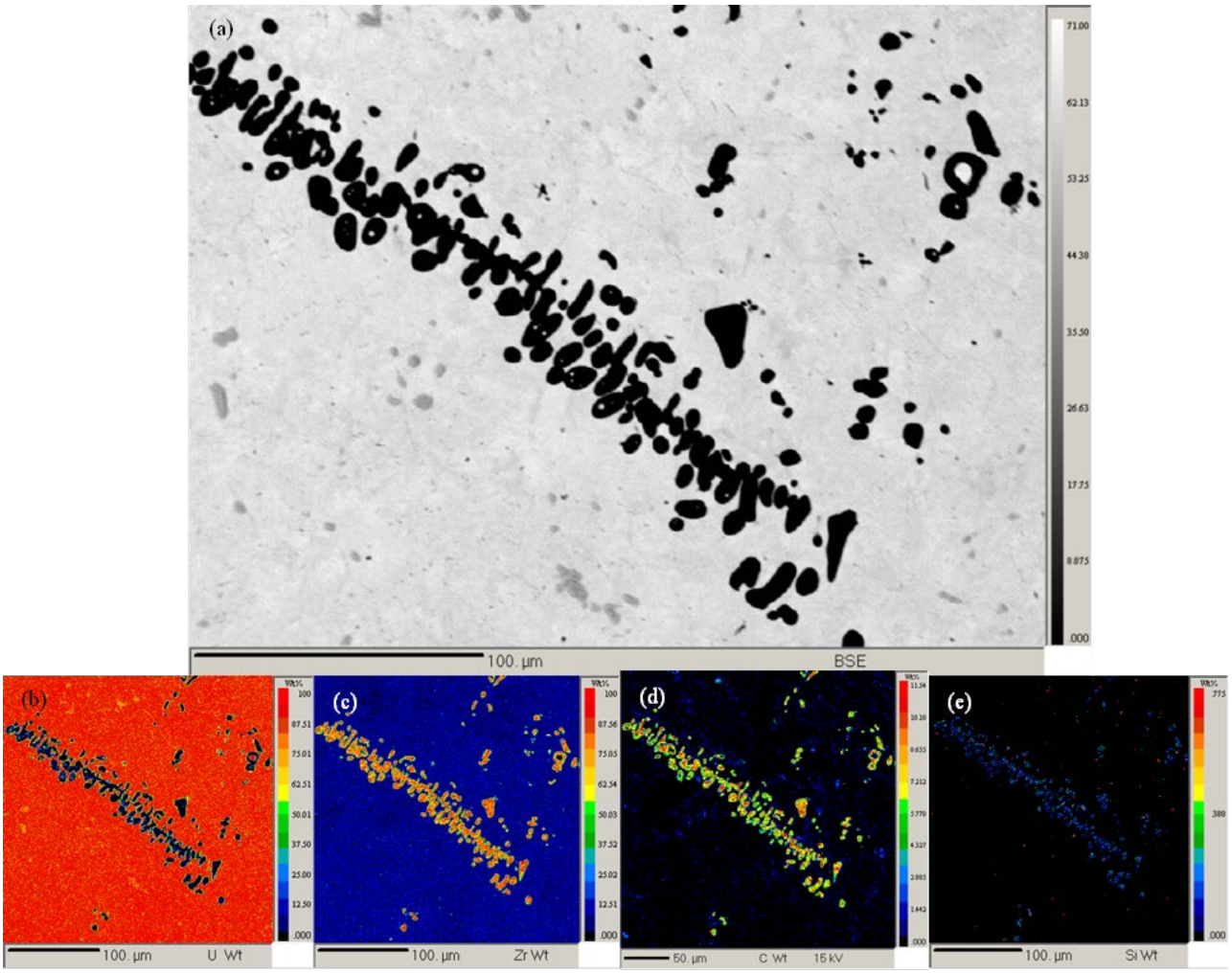

Figure 46. (a) Backscattered electron image showing lineation in Rb (transverse), (b–e) x-ray maps of the image shown in (a).

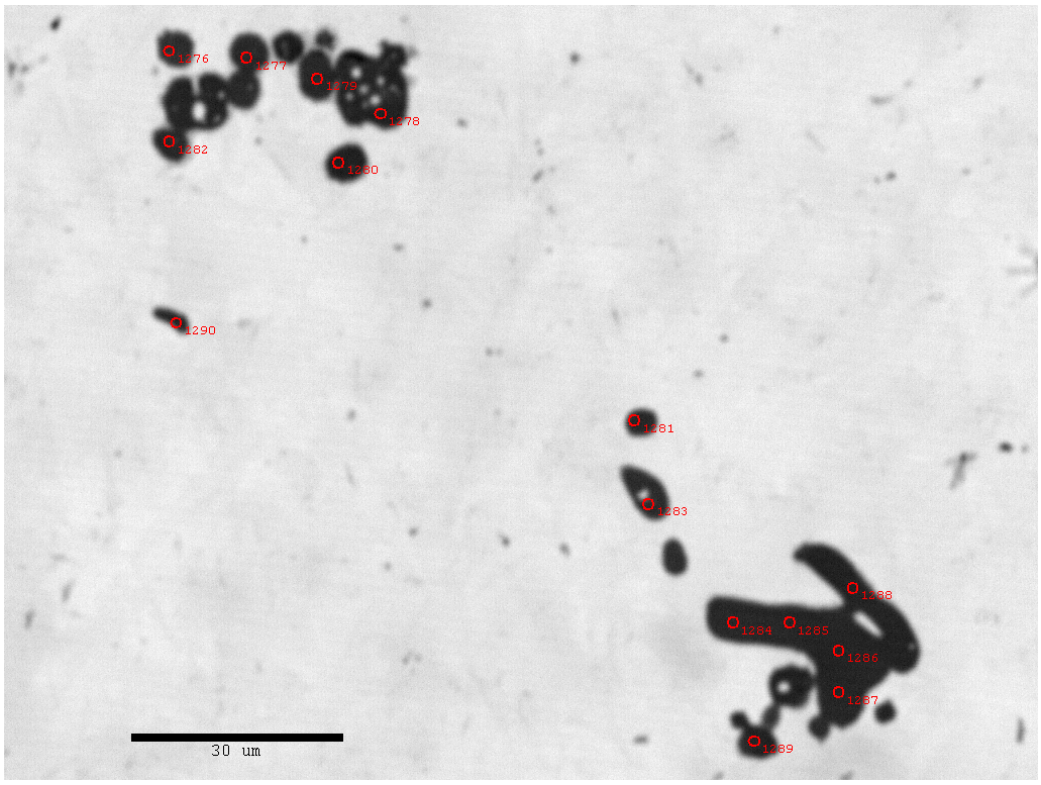

Figure 47. Phase shapes and analysis locations for an area in Rc (transverse). Results are shown in Table 16.

Table 16. Quantitative analyses of locations shown in Figure 47.

Spot	Si at%	U at%	Zr at%	C at%	Possible Phase ID
1276	0.08	69.8	22.6	7.5	—
1277	0.20	6.81	47.0	46.0	ZrC
1278	0.02	0.36	52.3	47.3	ZrC
1279	0.03	0.12	52.7	47.2	ZrC
1280	0.03	0.93	50.9	48.1	ZrC
1281	0.14	2.53	52.2	45.1	ZrC
1282	0.03	0.43	51.2	48.3	ZrC
1283	0.00	0.37	51.7	47.9	ZrC
1284	0.01	0.07	52.4	47.5	ZrC
1285	0.00	0.05	52.6	47.4	ZrC
1286	0.01	0.08	52.1	47.8	ZrC
1287	0.01	0.05	52.1	47.8	ZrC
1288	0.02	0.20	51.7	48.1	ZrC
1289	0.00	0.35	52.7	47.0	ZrC
1290	0.09	52.5	30.0	17.4	—

One remarkable feature particularly common in sample Ra (transverse and longitudinal) is the complex inclusions. As seen in Figure 48, the dark-colored anhedral phases are commonly enclosed by lighter-colored phases. These phases in turn reside either in the U-10Zr fuel matrix or are adhered to the rim. In some cases, the dark-colored phases

are enclosed within the rim (see Figure 49). Finally, within the dark-colored phases there are often circular, bright-colored phases (e.g., Point 754 in Figure 49).

Compositionally, the dark-colored phases most closely resemble ZrC (see Table 17), while the lighter gray phase contains relatively less carbon and appears to resemble Zr_xC, where X is approximately 5. The light-colored circular phase enclosed within the ZrC appears to be a bubble with a very high uranium content—in some cases exceeding 99 at% (Figure 49, Table 18).

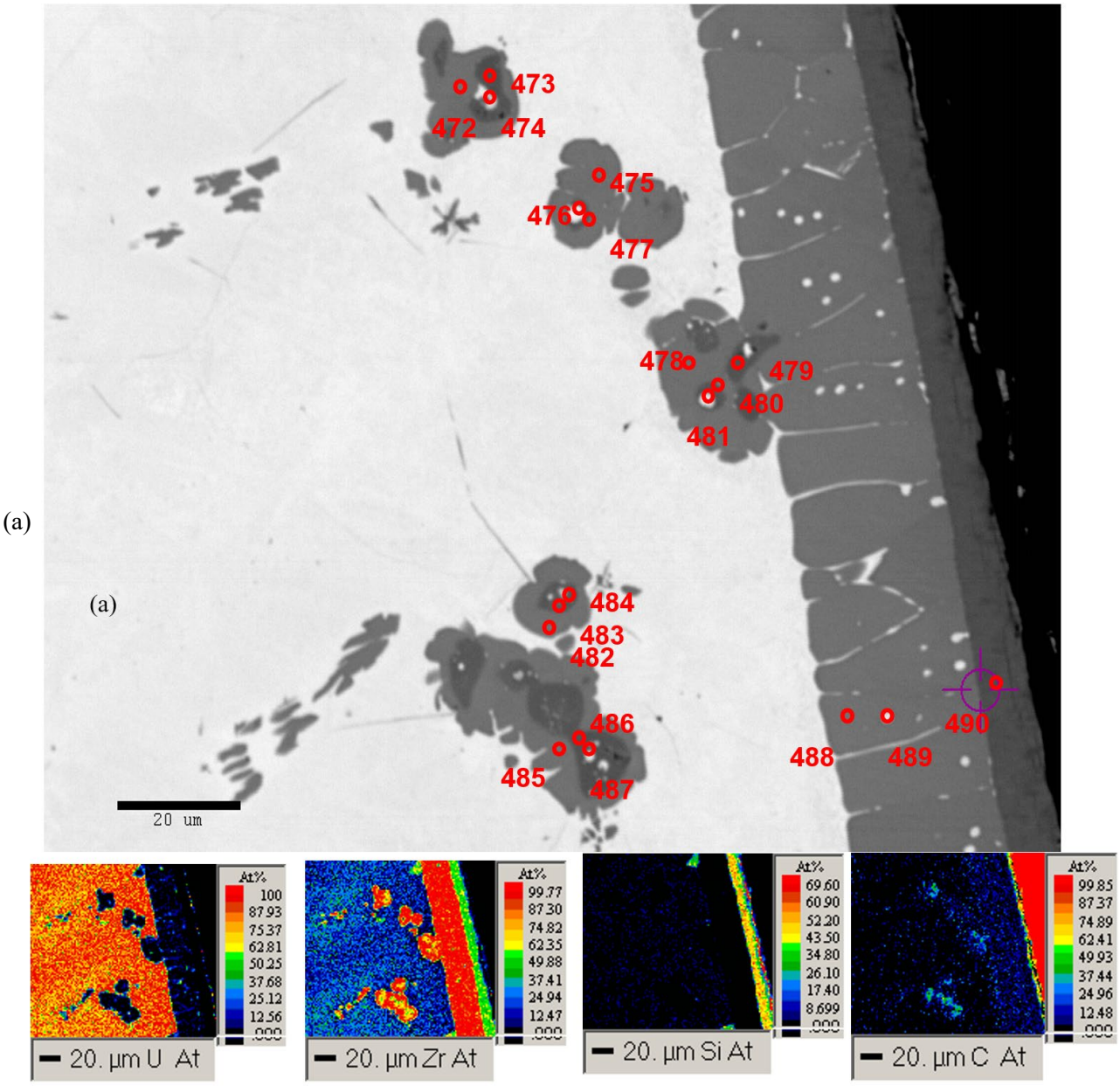

Figure 48. (a) Backscattered electron image showing complex inclusions with analyses locations for sample Ra (transverse) and (b–e) x-ray maps for image shown in (a).

Table 17. Quantitative analyses for locations shown in Figure 48.

Spot	Si at%	U at%	Zr at%	C at%	Possible Phase ID
472	0.03	1.13	86.0	12.8	—
473	0.01	0.09	54.4	45.5	ZrC
474	0.11	65.3	15.5	19.1	—
475	0.03	1.06	86.1	12.8	—
476	0.03	0.89	59.0	40.1	ZrC
477	0.05	94.8	4.45	0.7	—
478	0.01	1.17	85.6	13.2	—
479	0.01	0.53	54.8	44.6	ZrC
480	0.00	0.13	55.4	44.5	ZrC
481	0.18	92.2	4.80	2.85	—
482	0.03	1.19	85.2	13.6	—
483	0.03	1.47	54.3	44.2	ZrC
484	0.06	0.26	55.5	44.2	ZrC
485	0.05	1.00	85.0	13.9	—
486	0.00	0.09	53.6	46.3	ZrC
487	0.10	64.2	16.7	19.0	—
488	0.02	1.32	85.4	13.2	—
489	0.23	72.3	13.8	13.7	—
490	46.9	0.40	45.8	6.91	ZrSi

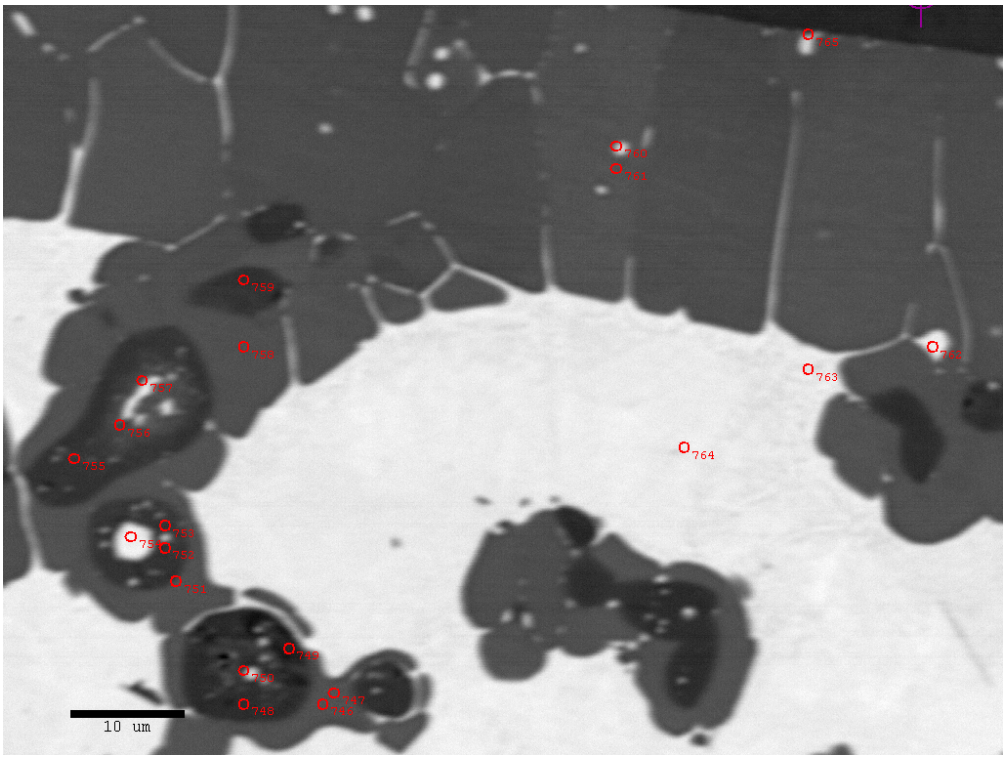

Figure 49. Backscattered electron image showing complex inclusions with analysis locations for the edge of sample Ra (longitudinal).

Table 18. Quantitative analyses of locations shown in Figure 49.

Spot	Si at%	U at%	Zr at%	C at%	Possible Phase ID
747	0.03	1.01	82.9	16.1	—
748	0.00	0.24	50.4	49.4	ZrC
749	0.00	0.22	51.4	48.3	ZrC
750	0.04	38.8	24.8	36.3	—
751	0.00	1.11	83.0	15.9	—
752	0.04	0.13	51.6	48.2	ZrC
753	0.08	11.0	39.7	49.2	—
754	0.01	99.8	0.96	0.0	—
755	0.04	0.42	48.8	50.8	ZrC
756	0.00	2.49	43.1	54.4	—
757	0.14	48.8	19.5	31.5	—
758	0.00	1.03	84.3	14.7	—
759	0.03	0.06	50.9	49.0	ZrC
760	0.05	29.0	38.0	32.9	—
761	0.00	1.23	84.2	14.5	—
762	0.06	80.5	8.61	10.9	—
763	2.06	83.4	7.70	6.8	—
764	0.17	83.6	10.4	5.9	—

765	0.09	46.9	27.7	25.3	—
766	37.7	0.51	49.0	12.8	—

6. HT9 CLADDING

6.1. Density

Table 19. Room temperature density of the HT9 cladding material.

Sample ID	Density (g/mL^3)
EBR Fuel Section	7.7414
EBR Fuel Sect 1	7.7234
EBR Fuel Sect 2	7.6856
EBR Fuel Sect 3	7.7866
EBR Plenum Section	8.0139
EBR Plenum Extra 1	7.7261
EBR Plenum Extra 2	7.7714
EBR Plenum Extra 3	7.7916
EBR Plenum Extra 4	7.8054
Average	7.7830
SD	0.0950
95% CI	0.0730

6.2. HT9 Cladding Hardness

Ten Vicker's hardness tests were performed on each of the tubing cladding using the LECO M-400-H1 hardness tester at spots uniformly distributed throughout the sample. The load used was 100 g. Table 20 shows the average HV as well as the relevant statistics. Measurements were consistent throughout the samples. Many hardness tests were also performed related to welds and the heat-affected zones (HAZ). This hardness information is presented in Section 7 (Weld Characterization).

Table 20. Microhardness data for HT9 cladding sectioned from EBR-II fuel element.

Sample ID	Average HV	SD	95% CI	Relative Accuracy % (RA)
Fuel Transverse	312	3.8	4.8	2
Fuel Longitudinal	309	2.9	3.6	1
Plenum Longitudinal	314	4.0	4.9	2

6.3. HT9 Microstructure

6.3.1. Sample Preparation

Three HT9 cladding samples were evaluated for microstructure: two longitudinal and one transverse cuts. These samples were sectioned from the fuel element after the fuel and Na bond was removed. They were then mounted in epo-heat epoxy and polished to a finish of 0.04 μm with colloidal silica. Beraha's reagent, a tint etchant, was used as an etchant to resolve features and make clear distinctions between ferrite and martensite. Each of the samples showed some pitting from this procedure. The two longitudinal samples were pitted enough that an additional treatment was necessary to remove the pitting. These two samples were repolished to 0.03 μm with an alumina suspension and re-etched with a modified Beraha's reagent.

6.3.2. Optical Microscopy Procedure

Prior to examining the sample, the Zeiss Axio Obersver.Z1m microscope was calibrated using a National Institute of Standard and Technology Standard Reference Material 2800 Microscope Magnification Standard in accordance with ASTM Standard E 1951-02 *Standard Guide for Calibrating Reticles and Light Microscope Magnifications*. The entirety of the sample was examined using the 5× objective then the 20× objective. Polarized light was used as the contrast as it creates easy identification of ferrite grains or other potential phases. Images were taken using an AxioCam MRc5 digital camera controlled by the AxioVision software version 4.8. One mosaic of the entire sample was created using the MosaiX Acquisition module for the AxioVision software version. Images were taken under polarized light using the 10× objective. The mosaics were stitched together using the AxioVision software.

6.3.2.1. Cladding at 50% of Fuel Length (transverse)

The direction for which the labeling inscribed on the back of the sample was upright was designated as 0°. Beginning with the area located at the 0° on the sample, a series of images were taken in a clockwise direction at 0°, 90°, 180°, and 270° for mosaic purposes. After the mosaic was created, a series of images was taken at each quarter location using bright field and polarized lighting with both the 10× and 20× objective lenses. Based upon the mosaic in Figure 50, the sample appears to be uniform throughout. Some staining from the etching procedure is evident along the sample edge, especially at the 180° and 270° positions and should be disregarded. Figure 51 shows an example of the sample microstructure, which consisted of a lath martensite. Careful examination can make out the presence of a small, rounded phase, likely carbides, in the structure. These phases were examined further using the scanning electron microscope (SEM). This microstructure of lath martensite with carbides was consistent throughout the sample and for both walls of the tube. Based on the defined martensite structure in both bright field (Figure 51) and polarized light (Figure 52), this sample has been quenched and tempered as evidenced by the difference in hardness from the bulk tube through the weld (see Section 6.2). No significant difference could be discerned between areas near the inner and outer diameters of the sample and those in the interior (see Figure 53 and Figure 54). There did not appear to be any significant influence from the fuel. Viewed optically, the sample appears to be relatively uniform.

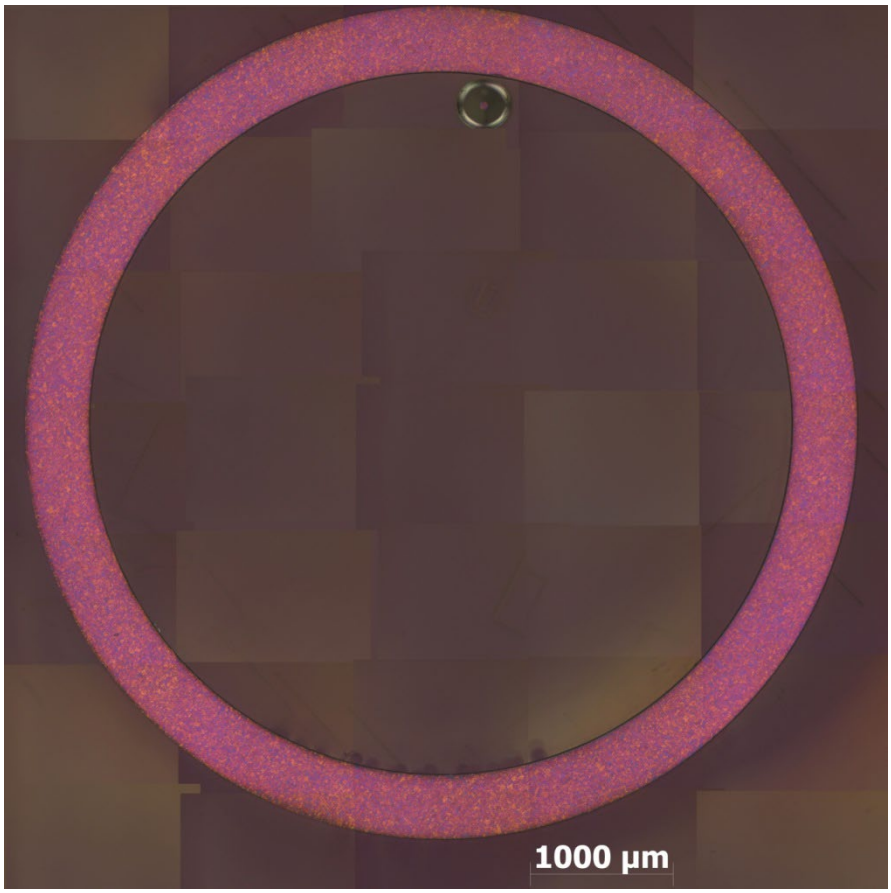

Figure 50. Mosaic of the EBR-II transverse sample taken under polarized light.

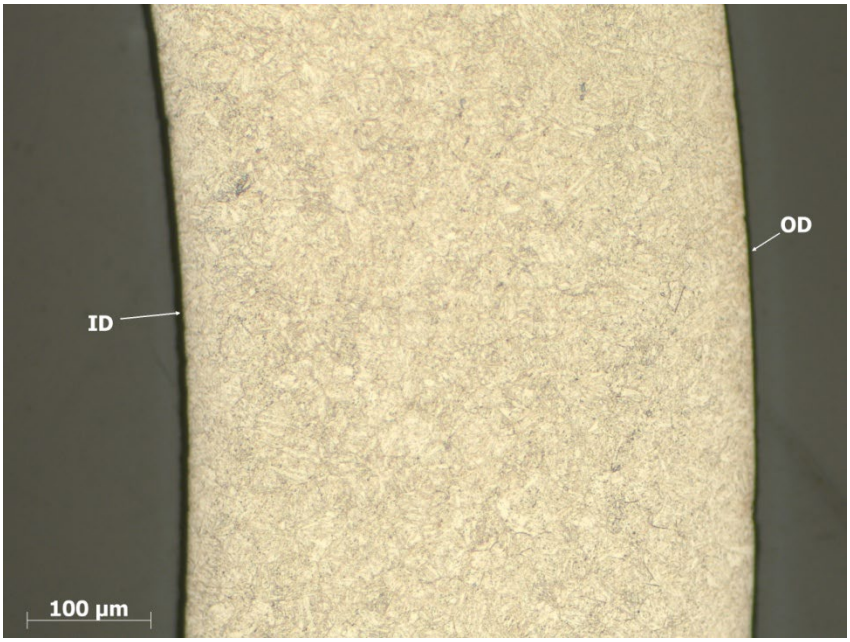

Figure 51. Lath martensite structure under bright field near the 90° point of the EBR-II transverse sample.

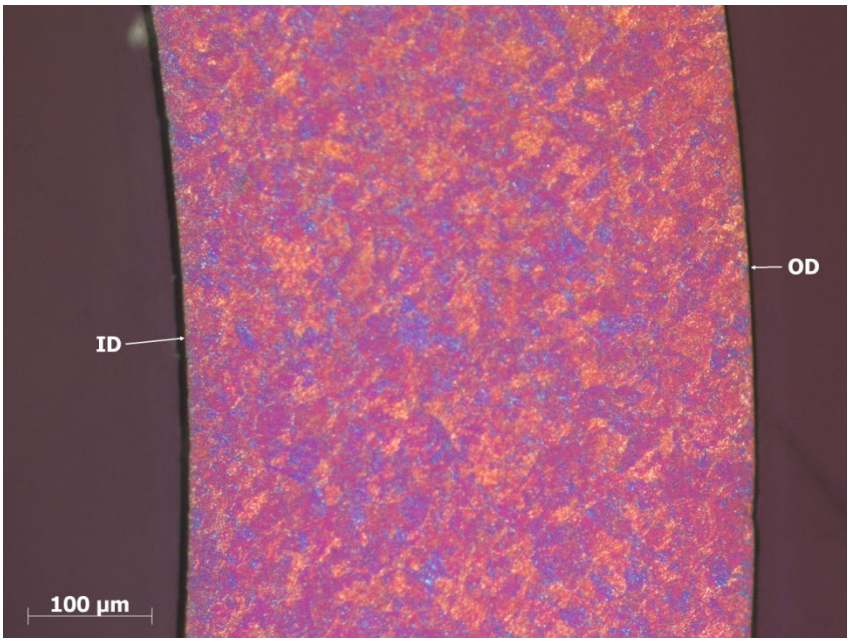

Figure 52. Lath martensite structure under polarized light near the 90° point of the EBR-II transverse sample.

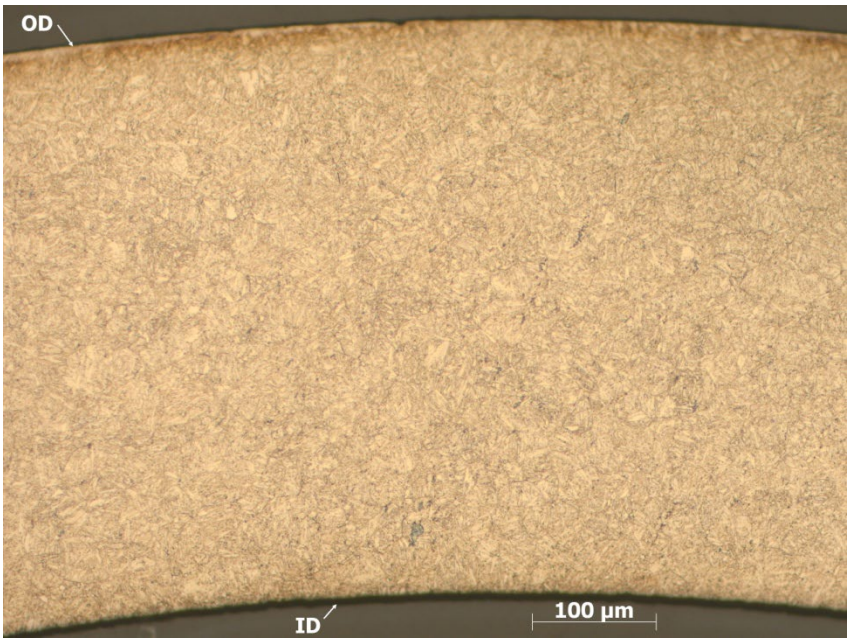

Figure 53. Area near 0° point of EBR-II transverse under bright field.

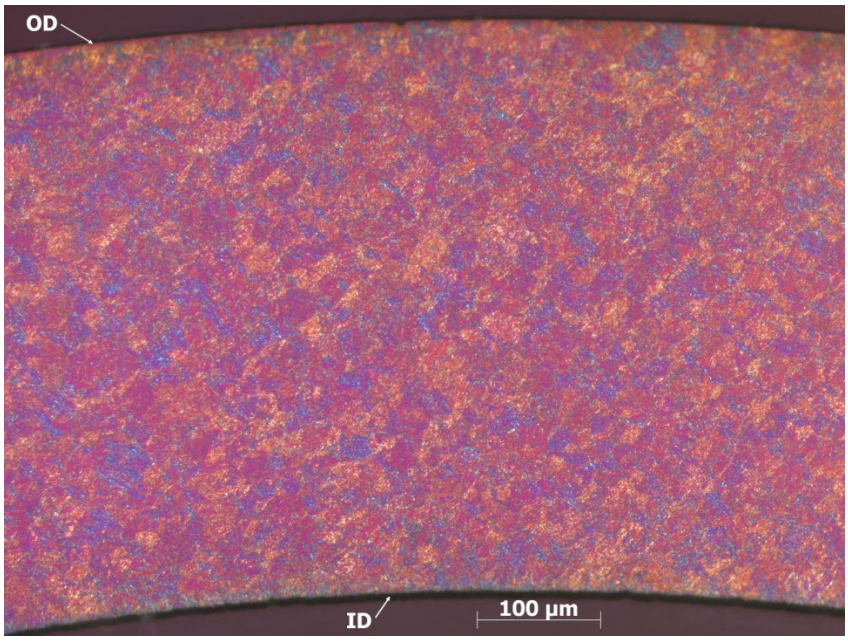

Figure 54. Area near 0° point of EBR-II transverse sample under polarized light.

6.3.2.2. Cladding at 50% of Fuel Length (longitudinal)

The direction for which the labeling inscribed on the back of the sample was upright was designated as 0°. The upper wall in this direction was designated the 0° wall, while the lower wall was designated the 180° wall. The 0° wall was imaged first. After the mosaics were created, a series of images was taken. For each wall, areas near the left and right edges were imaged as well as a region in the center. At each location, images were taken using bright field and polarized lighting with both the 10× and 20× objective lenses. Based on the mosaics in Figure 55 and Figure 56, the sample appears to be uniform throughout. Figure 57 shows an example of the sample microstructure, which consisted of a lath martensite. Careful examination shows the presence of a small, rounded phase, likely carbides, in the structure. These phases were examined further using the SEM. This microstructure of lath martensite with carbides was consistent throughout the sample and for both walls of the tube. Based on the defined martensite structure in both bright field (Figure 57) and polarized light (Figure 58), this sample has been quenched and tempered as evidenced by the difference in hardness from the bulk tube through the weld (see Section 6.2). The lack of slip lines (see Figure 59) and elongated or deformed grains (see Figure 60) near the surfaces indicates that the sample was re-austenized and quenched after being formed into the tube. This likely occurred as part of a precipitation hardening process. No significant difference could be discerned between areas near the inner and outer diameters of the sample and those in the interior. There did not appear to be any significant influence from the fuel. Viewed optically the sample appears to be relatively uniform.

Figure 55. Mosaic of the EBR-II longitudinal 0° wall.

Figure 56. Mosaic of the EBR-II longitudinal 180° wall.

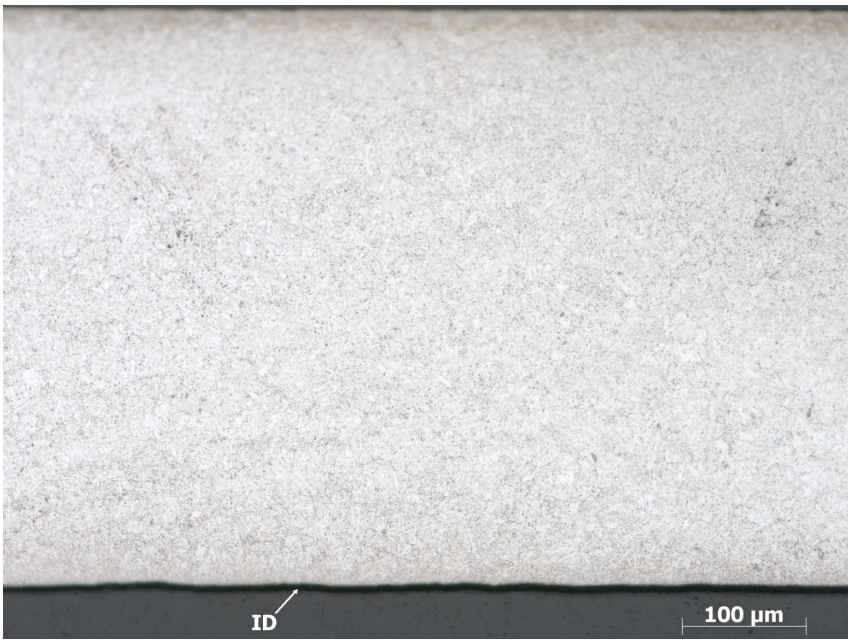

Figure 57. Lath martensite in area on the left section of the 0° wall on the EBR-II longitudinal sample.

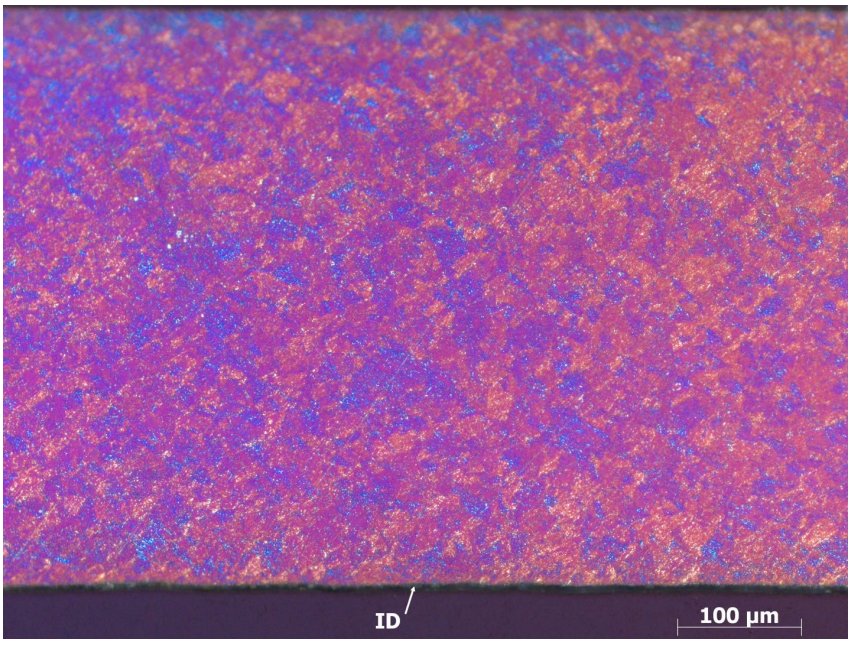

Figure 58. Lath martensite in area on the left section of the 0° wall on the EBR-II longitudinal sample under polarized light.

Figure 59. Area near the center of the 180° wall showing typical microstructure.

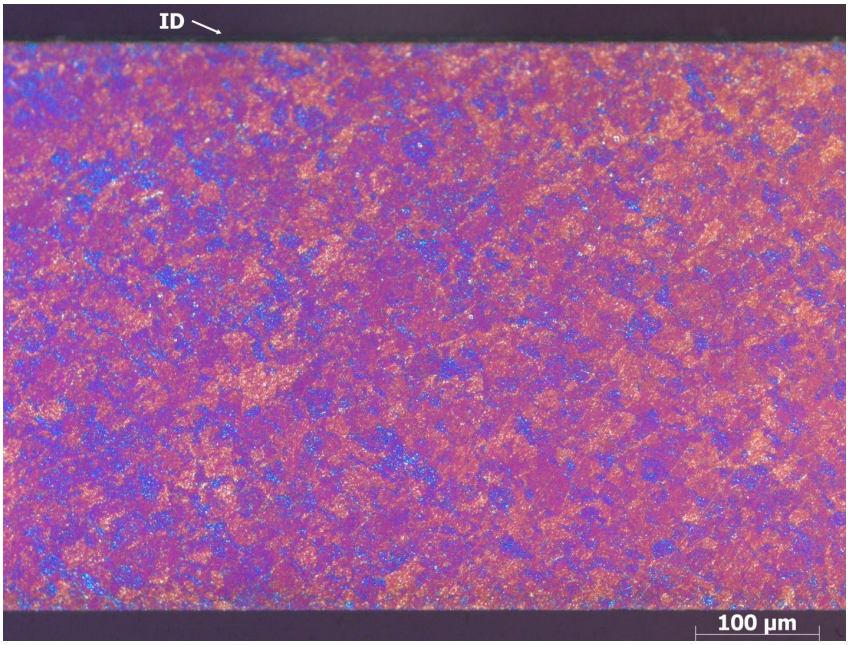

Figure 60. Area near the center of the 180° wall showing typical microstructure under polarized light.

6.3.2.3. Cladding at 50% of Plenum Length (longitudinal)

The direction for which the labeling inscribed on the back of the sample was upright was designated as 0°. The upper wall in this direction was designated the 0° wall, while the lower wall was designated the 180° wall. The 0° wall was imaged first. After the mosaics were created, a series of images was taken. For each wall, areas near the left and right edges were imaged as well as a region in the center. At each location, images were taken using bright field and polarized lighting with both the 10× and 20× objective lenses. Based on the mosaics in Figure 61 and Figure 62, the sample appears to be uniform throughout. Figure 63 shows an example of the sample microstructure, which consisted of a lath martensite. Careful examination can make out the presence of small, rounded phase, likely carbides, in the

structure. These phases were examined further using SEM. This microstructure of lath martensite with carbides was consistent throughout the sample and for both walls of the tube. Based on the defined martensite structure in both bright field (Figure 63) and polarized light (Figure 64), this sample has been quenched and tempered. The lack of slip lines (see Figure 65) and elongated or deformed grains (see Figure 66) near the surfaces indicates that the sample was re-austenitized and quenched after being formed into the tube. This likely occurred as part of a precipitation hardening process. No significant difference could be discerned between areas near the inner and outer diameters of the sample and those in the interior. There did not appear to be any significant influence from the fuel. Viewed optically, the sample appears to be relatively uniform.

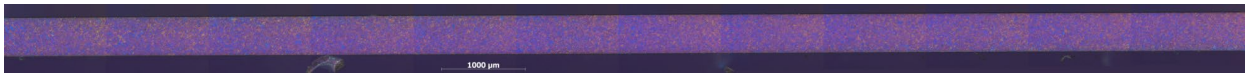

Figure 61. Mosaic of the EBR-II plenum section 0° wall under polarized light.

Figure 62. Mosaic of the EBR-II plenum section 180° wall under polarized light.

Figure 63. Lath martensite in area on the left section of the 0° wall on the EBR-II plenum section sample.

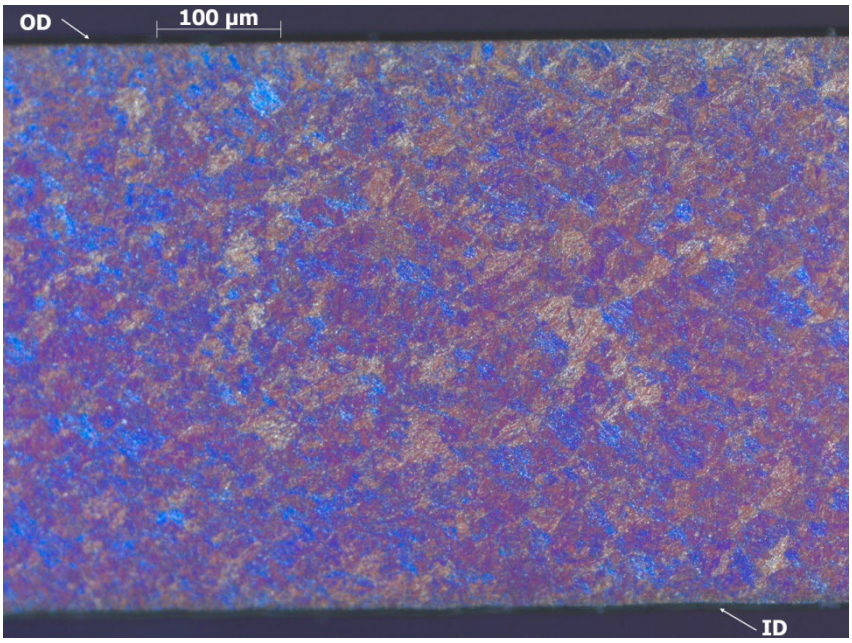

Figure 64. Lath martensite in area on the left section of the 0° wall on the EBR-II plenum section sample under polarized light.

Figure 65. Area on the left section of the 180° wall showing typical microstructure.

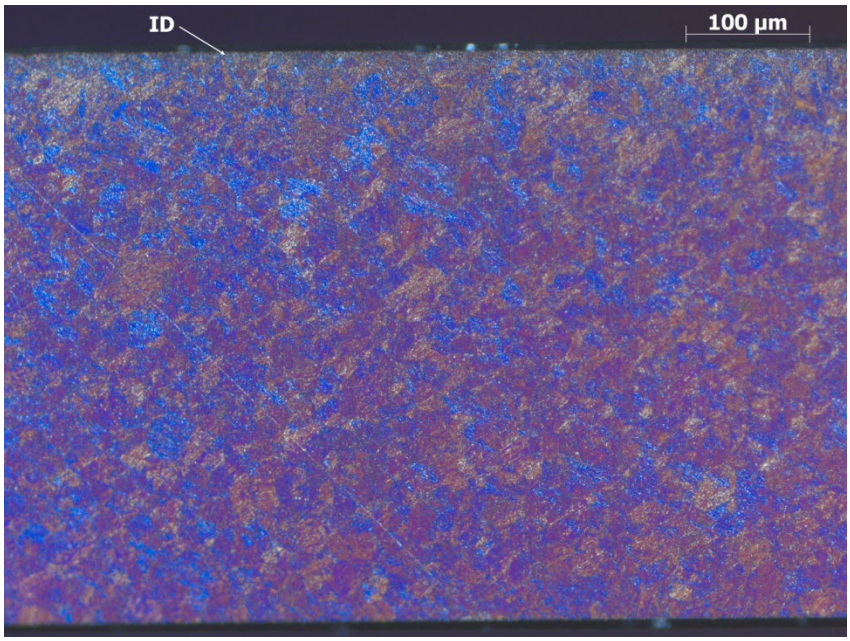

Figure 66. Area on the left section of the 180° wall showing typical microstructure under polarized light.

6.3.3. Scanning Electron Microscopy Procedure

The SEM used was a Quanta 650 FEG SEM configured with an EDAX Triton package v5.1. All images were captured in high vacuum mode with a thin coating of carbon deposited for conductivity over the sample. The sample was examined at the 0° and ±90° positions for the transverse and along the 0° length at 250× to look for sample uniformity as well as unusual phases or features. Images were then taken at 250×, 1,000×, 2,000×, 4,000× and 10,000× in a representative area of the sample to show general structure and precipitate count. The 10,000× image was also used to document the EDS collection areas of the precipitates and the bulk material. With the same Beraha's etch in place, five random areas along the 0° position of the material were imaged with high contrast and low brightness to document the larger carbide precipitates present in the material in backscatter imaging mode. The sample was then mechanically aligned to perform electron backscatter diffraction (EBSD) and orientation imaging microscopy on two areas of the material. The first scan acquired via EBSD was a random location from the 0° position of the material while the second scan was obtained from the 180° position. After completion of the EBSD scans, the samples were metallographically prepared to emphasize the denuded phases suspected of being ferrite as well as the fine precipitates that were present in high count number throughout the sample. These samples were prepared by first removing the features present from the Beraha's etch by polishing to a 0.03 µm with an alumina suspension. Next, a potassium hydroxide (KOH) electrolytic etch was used to highlight the suspected ferrite phases and the minor precipitates. Samples were again coated with a thin layer of carbon to ensure conductivity. Samples were reintroduced into the SEM, and five random images in backscatter imaging mode at 1,000× were taken along the sample entirety to document the suspected ferrite phase. Five additional images were taken at 5,000× to enhance the ultrafine precipitate phase in backscatter imaging mode.

6.3.3.1. Cladding at 50% of Fuel Length (transverse)

Examination confirmed the presence of carbides in the sample. The sample height differences made them appear white in backscatter imaging, as can be seen in Figure 67 due to effect of etch used in sample preparation. EDS found that the carbides were rich in molybdenum and chromium. The majority of these carbides were quite small at ~1–5 microns. Another rounded phase was present in the sample. No significant compositional difference could be obtained using EDS, but these areas clearly reacted differently to the etchant than the martensitic areas and were often outlined with carbides while the structure of the secondary phase was vacant of any carbide form. These regions are most likely delta ferrite, but that cannot be confirmed. These areas are identified with the arrows in Figure 67. Figure 68 (a and b)

show examples of the EDS spectra contrasting the chromium and molybdenum content between the base material and precipitate, respectively.

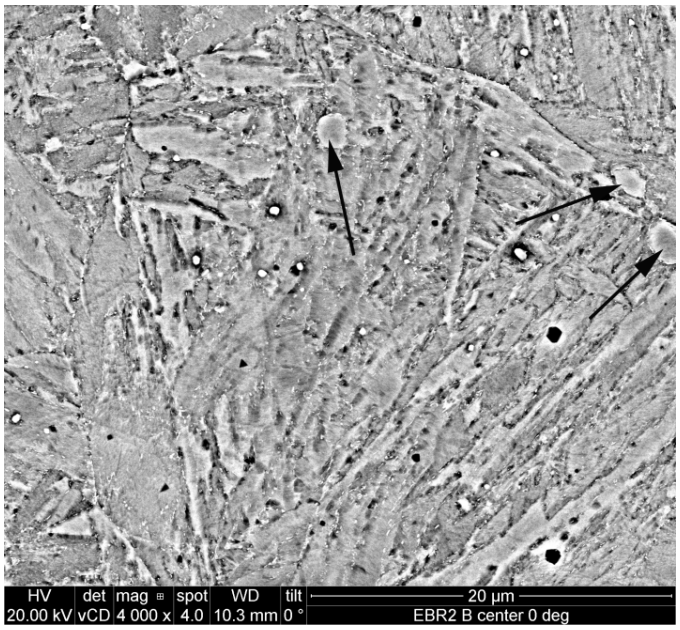

Figure 67. SEM image of 0° wall of EBR-II transverse section. White areas are carbides and arrows point to potential delta ferrite.

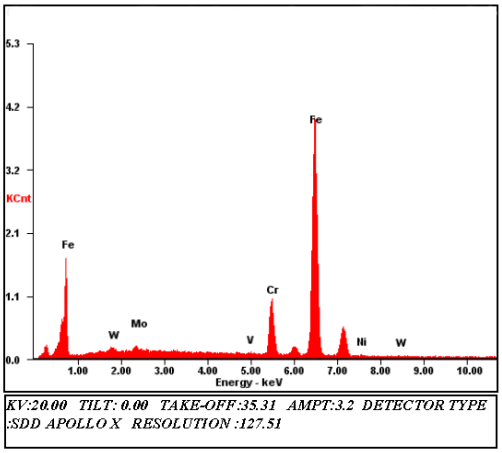

Element	Wt %	At %
MoL	01.43	00.84
V K	00.51	00.56
CrK	11.82	12.84
FeK	83.25	84.24
NiK	00.91	00.87
W L	02.09	00.64

a.

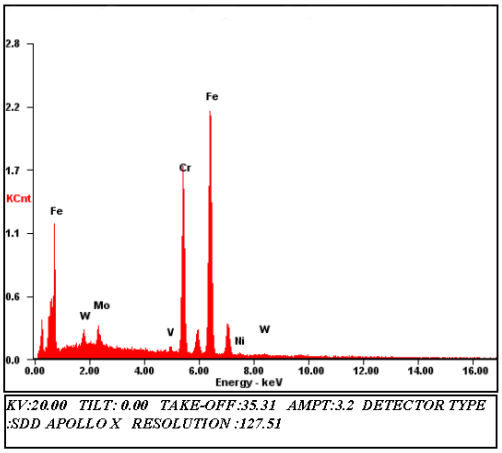

Element	Wt %	At %
MoL	03.00	01.77
V K	00.93	01.03
CrK	29.13	31.73
FeK	62.71	63.60
NiK	00.85	00.82
W L	03.38	01.04

b.

Figure 68. (a) EDS of steel matrix and (b) EDS of carbide precipitate.

SEM images were taken to estimate the volume fraction of carbides. Image analysis was performed using the AxioVision software. Backscatter electron imaging was used to create contrast between the carbides and steel. The image contrast was then adjusted to an extreme value so the carbides would be extremely bright and the matrix gray, as shown in Figure 69. This made it easy for the AxioVision software to perform an automated image analysis. To refine the image, a sigma filter to reduce noisiness and an edge enhancement to define the boundaries were employed.

As these images were imported from a different system, precise measurements were not taken and the measurement markers were removed so they would not be included in the analysis. Area fractions were measured from five images. The average area fraction (AAF), SD, 95% CI, and RA were calculated from the results. Based on this estimate, the EBR-II transverse sample has approximately 0.48 ± 0.07 vol% of carbides present with a 0.06 SD, 0.07 CI at 95%, and a RA of 15%.

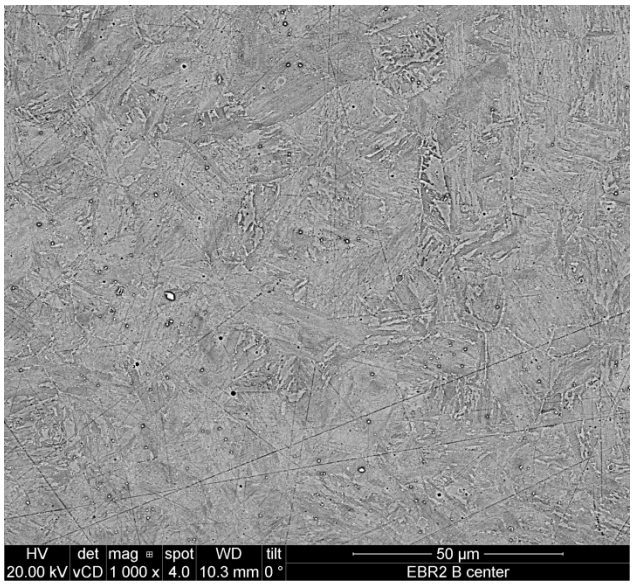

Figure 69. High-contrast BSE image of EBR-II transverse section showing carbides as bright points.

6.3.3.1.1. Grain Size Estimate

The Beraha's etchant failed to bring out the grain boundaries distinctly enough to measure using any ASTM method. As an alternative, two EBSD scans were performed on different areas of the sample in the SEM. The EBSD reveals features of the crystallographic orientation of the material, and by careful examination of the pattern, it is possible to make a rough estimate of the grain sizes. Figure 70 shows an example of the image generated by the EBSD. These images were transferred to the AxioVision software, where the scale bar on the images was used to calibrate the measurements. As Figure 70 shows, each image was divided into thirds to cover the ID, outer diameter (OD), and center (CT). Each image was oriented such that the ID was the top of the image. From each section, a minimum of 20 measurements was taken. The longest perceivable diameter was measured when possible, but when uncertainty was present, preference was given to the more distinct grain boundaries. Once all measurements were taken, average grain sizes per section and the total were calculated. Table 21 shows the results of this estimate. It should be noted that these measurements should be considered a rough estimate only. Proper measurement of grain sizes requires the grain boundaries to be clearly visible. Alternate etches attempted failed to reveal the grain boundaries. This method was only employed as a last resort. The average grain size was estimated at ~30 µm.

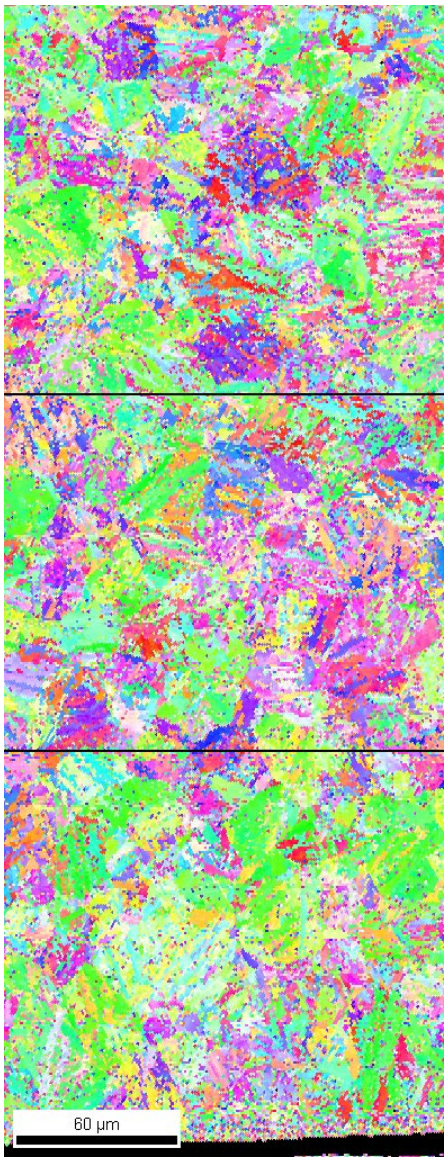

Figure 70. EBSD showing differences in crystallographic orientation. It is possible to roughly make out the grains of the material.

Table 21. Grain size estimates via EBSD for EBR-II transverse sample.

Section	ID	CT	OD	Total
Average Size	30.1 µm	28.8 µm	29.6 µm	29.5 µm
SD	8.8	8.0	11.0	9.3
95% CI	2.6	2.5	3.5	1.6
% RA	8.5%	8.6%	11.9%	5.4%

6.3.3.1.2. Delta Ferrite Estimate

As mentioned previously, rounded phases were observed that may be delta ferrite. The Volume 9 ASTM handbook indicated that the electrolytic KOH etch would stain delta ferrite. The optical microscope showed some potentially stained areas, but they were too small to clearly see with the 20× objective. Due to the small size of the sample mounts relative to the microscope, the higher magnification objectives could not be used. When viewed at higher magnifications in the SEM, this etch did bring out both the potential delta ferrite phases and the carbides. This etch also revealed that the carbides observed previously were only a small fraction of those present. There were numerous other small carbides throughout the sample. The five images taken of random areas of the sample at 1,000× magnification were used to estimate delta ferrite, while the five images at 5,000× magnification were used to re-estimate carbide content.

The contrast on the SEM was adjusted such that the carbides appeared black, while the rest of the steel was light gray to make it easy for the AxioVision software to perform an image analysis. Figure 71 shows an example of the high magnification images of the carbides. Because the potential delta ferrite phases were the same color as the martensitic areas of the steel, each of ferrite phases identified in the 1,000× images were shaded red using Adobe Photoshop. This created a color contrast for the AxioVision software to work with. Figure 72 shows an example image altered in this manner. The only image enhancement performed for the analyses was a sigma filter of 32 and an edge enhancement with a threshold of 25 and size of 3. The results of the estimate are presented in Table 22. It was estimated that the volume fraction of delta ferrite was 0.31% ± 0.13%. Due to the uncertainty in the RA, the confidence that this estimate is correct is low. At higher magnifications, the carbides were estimated to be 11 vol% ± 1.2%. This is much higher than the previous estimate and suggests that there are numerous small carbides present in the martensitic structure, as would be expected to occur in a tempering process.

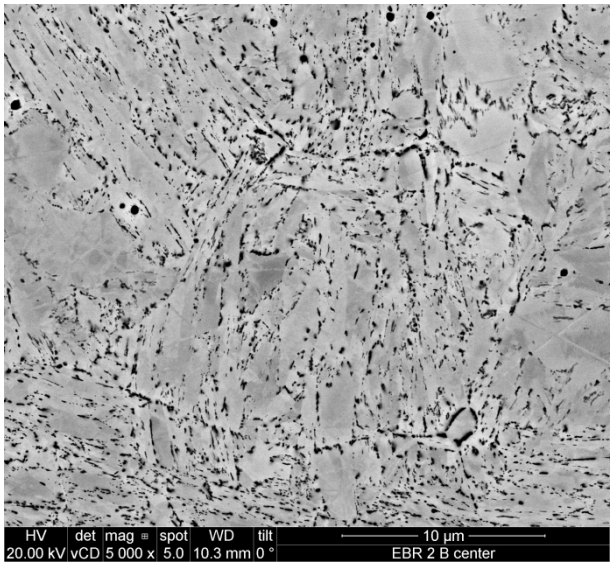

Figure 71. High-magnification image of carbides revealed by electrolytic KOH etch.

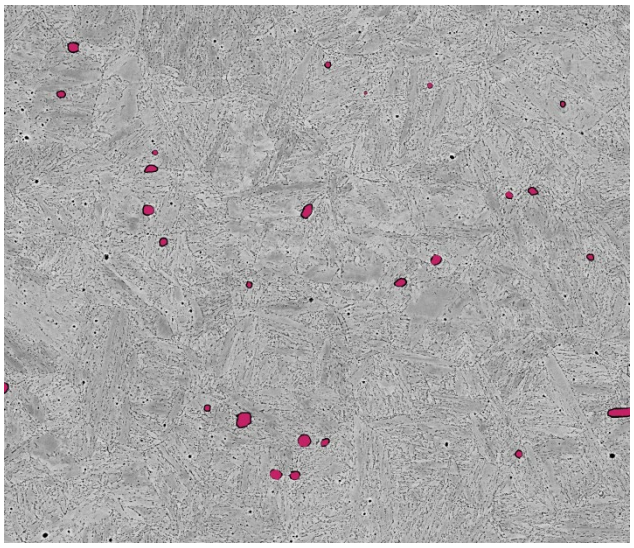

Figure 72. SEM image with delta ferrite phases marked in red.

Table 22. Delta ferrite and high-magnification carbide estimates on EBR-II transverse sample.

Phase	Delta Ferrite	Carbides
AAF	0.31%	11%
SD	0.11	1.0
95% CI	0.13	1.2
% RA	42%	11%

6.3.3.2. Cladding at 50% of Fuel Length (longitudinal)

Examination confirmed the presence of carbides in the sample. The sample height differences made them appear white in backscatter imaging, as can be seen in Figure 73 due to effect of the etch used in sample preparation. EDS found that the carbides were rich in molybdenum and chromium. The majority of these carbides were quite small at ~1–5 microns. Another rounded phase was present in the sample. No significant compositional difference could be obtained using EDS, but these areas clearly reacted differently to the etchant than the martensitic areas and were often outlined with carbides while the structure of the secondary phase was vacant of any carbide forms. These regions are most likely delta ferrite but that cannot be confirmed. These areas are identified with the arrows in Figure 73. Figure 74 (a and b) shows examples of the EDS spectra contrasting the chromium and molybdenum content between the base material and precipitate, respectively.

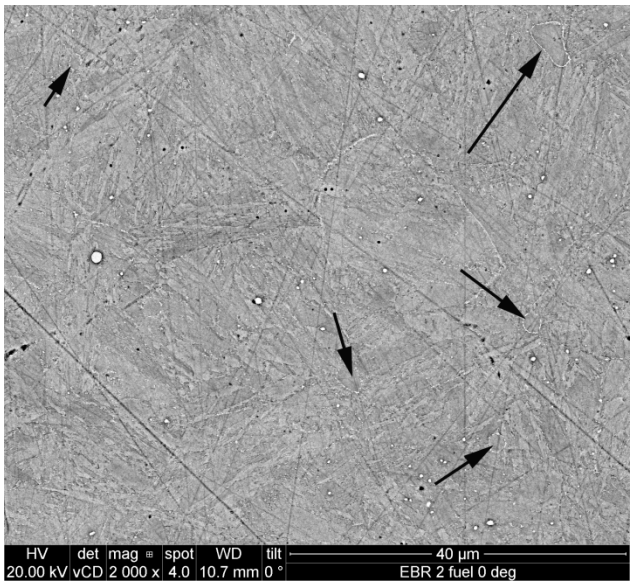

Figure 73. SEM image of 0° wall of EBR-II longitudinal fuel section. White areas are carbides. Arrows point to potential delta ferrite.

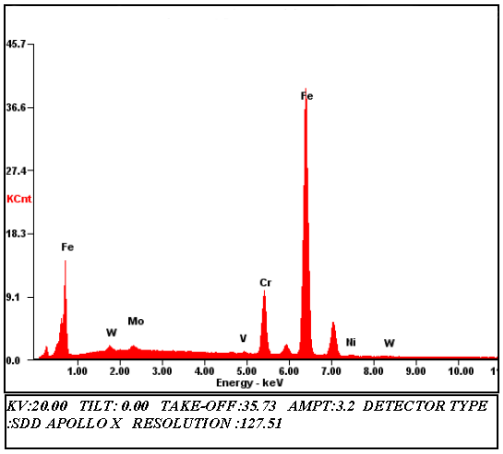

a.

Element	Wt %	At %
MoL	01.03	00.60
V K	00.26	00.29
CrK	12.11	12.98
FeK	85.91	85.70
NiK	00.35	00.34
W L	00.34	00.10

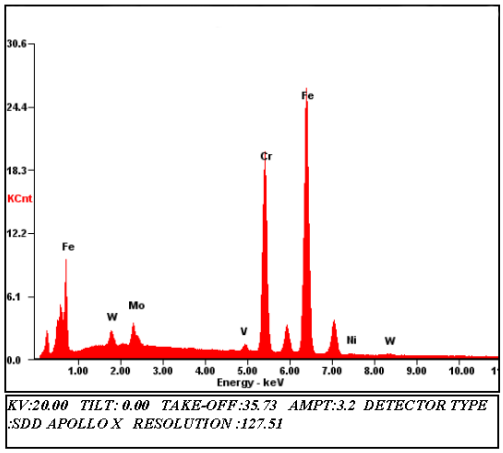

b.

Element	Wt %	At %
MoL	03.38	01.98
V K	00.91	01.00
CrK	29.99	32.45
FeK	63.07	63.53
NiK	00.34	00.32
W L	02.31	00.71

Figure 74. (a) EDS of the steel matrix and (b) EDS of carbide precipitate.

SEM images were taken to estimate the volume fraction of carbides. Image analysis was performed using the AxioVision software. Backscatter electron imaging was used to create contrast between the carbides and steel. The image contrast was then adjusted to an extreme value so the carbides would be extremely bright and the matrix black, as shown in Figure 75. This made it easy for the AxioVision software to perform an automated image analysis. To refine the image, a sigma filter to reduce noisiness and an edge enhancement to define the boundaries were employed.

As these images were imported from a different system, precise measurements were not taken and the measurement markers were removed so they would not be included in the analysis. Area fractions were measured from five images. The AAF, SD, 95% CI, and RA were calculated from the results. Based on this estimate, the EBR-II fuel sample has approximately 1.9 ± 0.34 vol% of carbides with 0.27 SD, an 0.34 CI at 95%, and a RA of 18%.

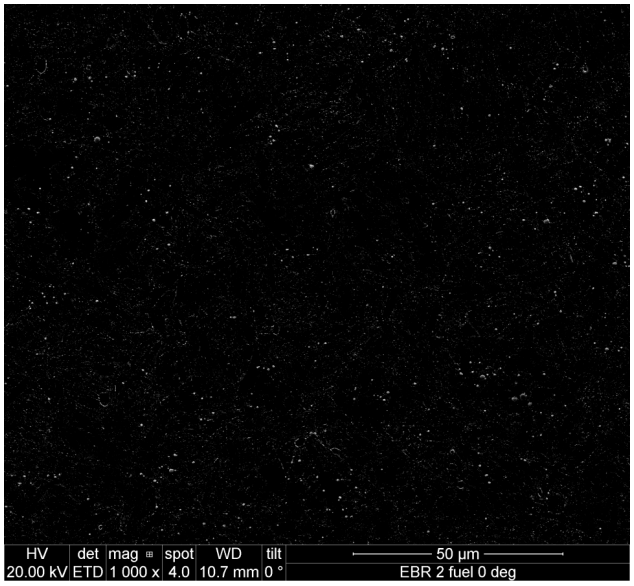

Figure 75. High-contrast BSE image of EBR-II longitudinal fuel section showing the carbides as bright points.

6.3.3.2.1. Grain Size Estimate

The Beraha's etchant failed to bring out the grain boundaries distinctly enough to measure using any ASTM method. As an alternative, two EBSD scans were performed on different areas of the sample in the SEM. The EBSD reveals features of the crystallographic orientation of the material, and by careful examination of the pattern, it is possible to make a rough estimate of the grain sizes. Figure 76 shows an example of the image generated by the EBSD. These images were transferred to the AxioVision software, where the scale bar on the images was used to calibrate the measurements. Each image was divided into thirds to cover the ID, OD, and CT. Each image was oriented such that the ID was the top of the image. From each section a minimum of 20 measurements was taken. The longest perceivable diameter was measured when possible, but when uncertainty was present, preference was given to the more distinct grain boundaries. Once all measurements were taken, average grain sizes per section and total average were calculated. Table 23 shows the results of this estimate. It should be noted that these measurements should be considered a rough estimate only. Proper measurement of grain sizes requires the grain boundaries to be clearly visible. Alternate etches attempted failed to reveal the grain boundaries. This method was only employed as a last resort. The average grain size was estimated at ~26 µm.

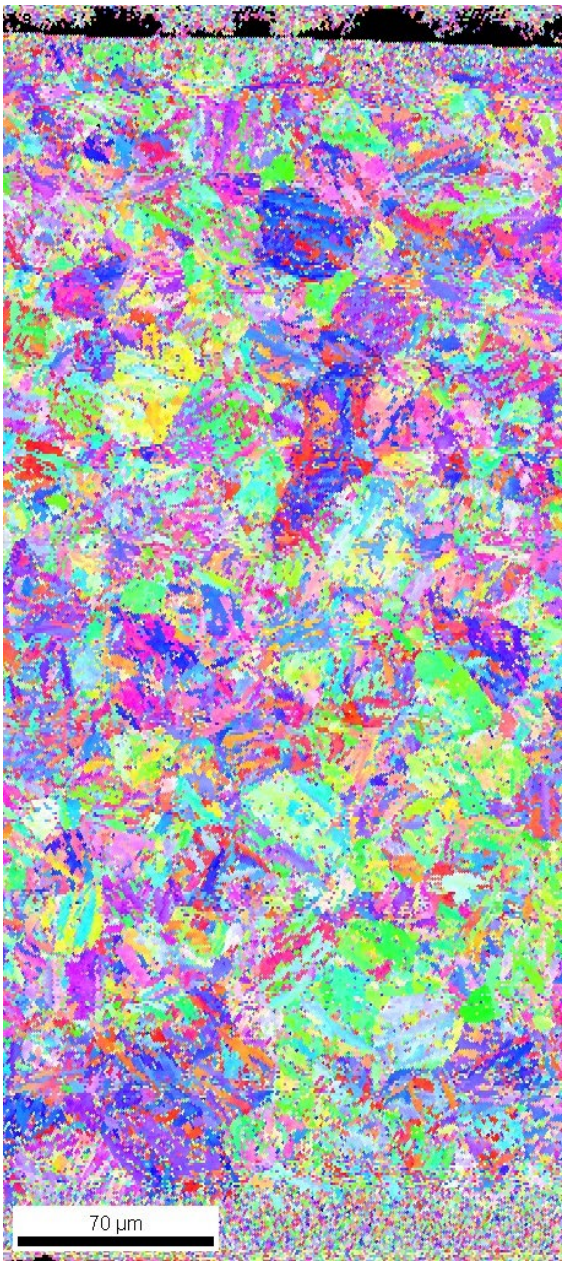

Figure 76. EBSD showing differences in crystallographic orientation. It is possible to roughly make out the grains of the material.

Table 23. Grain size estimates via EBSD for EBR-II longitudinal fuel section.

Section	ID	CT	OD	Total
Average Size	27.1 µm	24.7 µm	26.1 µm	25.9 µm
SD	4.5	4.4	5.3	4.8
95% CI	1.4	1.3	1.6	0.8
% RA	5.2%	5.2%	6.2%	3.1%

6.3.3.2.2. Delta Ferrite Estimate

As mentioned previously, rounded phases were observed that may be delta ferrite. The Volume 9 ASTM handbook indicated that the electrolytic KOH etch would stain delta ferrite. The optical microscope showed some potentially stained areas, but they were too small to clearly see with the 20× objective. Due to the small size of the sample mounts relative to the microscope, the higher magnification objectives could not be used. When viewed at higher magnifications in the SEM, this etch did bring out both the potential delta ferrite phases as well as the carbides. This etch also revealed that the carbides observed previously were only a small fraction of those present. There were numerous other small carbides throughout the sample. The five images taken of random areas of the sample at 1,000× magnification were used to estimate delta ferrite, while the five images at 5,000× magnification were used to re-estimate carbide content.

The contrast on the SEM was adjusted such that the carbides appeared black, while the rest of the steel was light gray to make it easy for the AxioVision software to perform image analysis. Figure 77 shows an example of the high-magnification images of the carbides. Because the potential delta ferrite phases were the same color as the martensitic areas of the steel, each of ferrite phases identified in the 1000× images were shaded red using Adobe Photoshop. This created a color contrast for the AxioVision software to work with. Figure 78 shows an example image altered in this manner. The only image enhancement performed for the analyses was a sigma filter of 32 and an edge enhancement with a threshold of 25 and size of 3. The results of the estimate are presented in Table 24. It was estimated that the volume fraction of delta ferrite was 0.38% ± 0.17%. Due to the uncertainty in the RA, the confidence in this estimate is low. At higher magnifications the carbides were estimated to be 14 vol.% ± 2.3%. This is much higher than the previous estimate and suggests that there are numerous small carbides present in the martensitic structure.

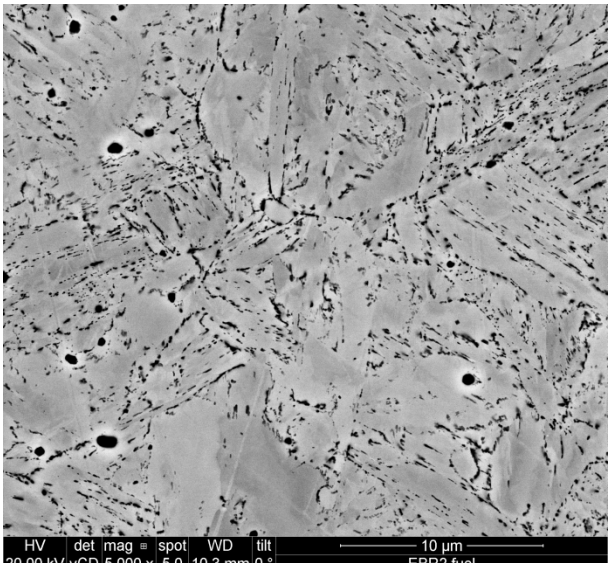

Figure 77. High-magnification image of carbides reveled by electrolytic KOH etch on EBR-II longitudinal fuel section.

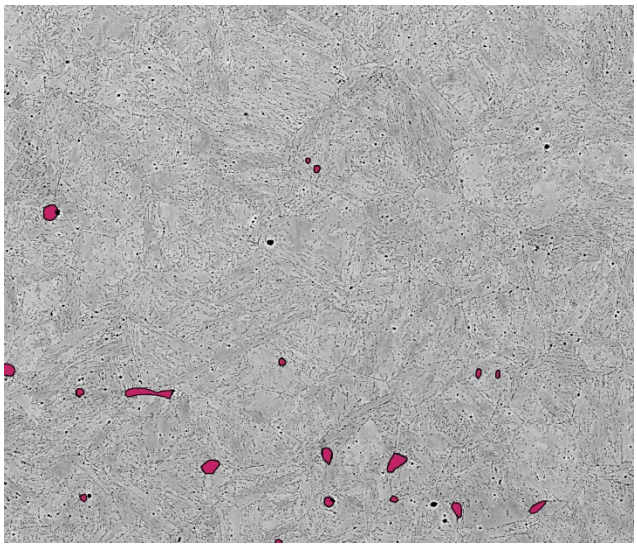

Figure 78. SEM image with the delta ferrite phases marked in red.

Table 24. Delta ferrite and high-magnification carbide estimates for EBR-II longitudinal fuel section.

Phase	Delta Ferrite	Carbides
AAF	0.38%	14%
SD	0.14	1.9
95% CI	0.17	2.3
% RA	44%	16%

6.3.3.3. Cladding at 50% of Plenum Length (longitudinal)

Examination confirmed the presence of carbides in the sample. The sample height differences made them appear white in backscatter imaging, as can be seen in Figure 79, due to the effect of the etch used in sample preparation. EDS found that the carbides were rich in molybdenum and chromium. The majority of these carbides were quite small at ~1–5 microns. Another rounded phase was present in the sample. No significant compositional difference could be obtained using EDS, but these areas clearly reacted differently to the etchant than the martensitic areas and were often outlined with carbides while the structure of the secondary phase was vacant of any carbide forms. These regions are most likely delta ferrite, but that cannot be confirmed. These areas are identified with the arrows in Figure 79. Figure 80 (a and b) shows examples of the EDS spectra contrasting the chromium and molybdenum content between the base material and precipitate, respectively.

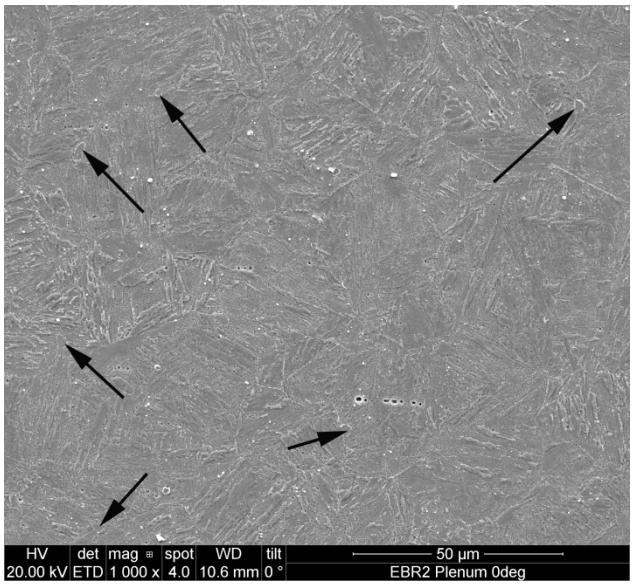

Figure 79. SEM image of 0° wall of EBR-II plenum section. White areas are carbides. Arrows point to potential delta ferrite.

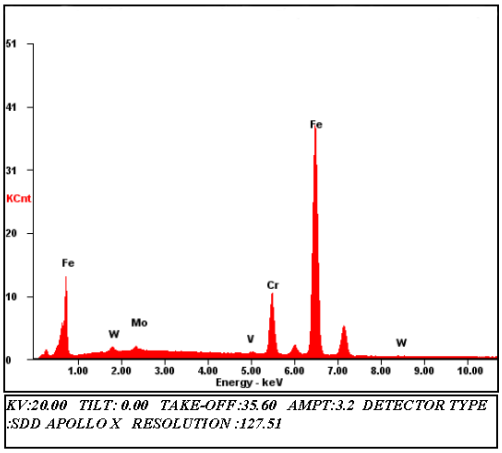

Element	Wt %	At %
MoL	01.13	00.66
V K	00.41	00.45
CrK	12.99	13.97
FeK	84.50	84.62
W L	00.97	00.30

a.

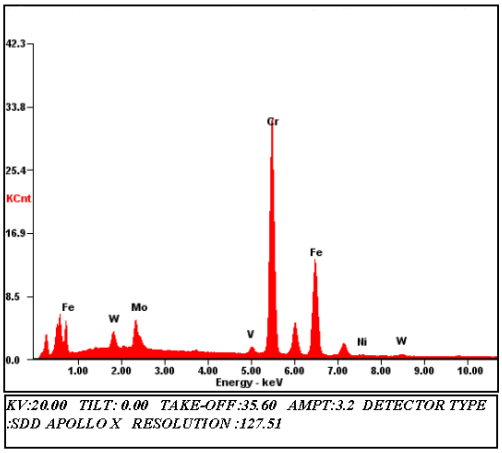

Element	Wt %	At %
MoL	06.16	03.63
V K	01.33	01.48
CrK	53.69	58.33
FeK	34.57	34.97
NiK	00.43	00.41
W L	03.82	01.17

b.

Figure 80. (a) EDS of steel matrix and (b) EDS of carbide precipitate.

SEM images were taken to estimate for the volume fraction of carbides. Image analysis was performed using the AxioVision software. Backscatter electron imaging was used to create contrast between the carbides and steel. The image contrast was then adjusted to an extreme value so the carbides would be extremely bright and the matrix black, as shown in Figure 81. This made it easy for the AxioVision software to perform an automated image analysis. To refine the image, a sigma filter to reduce noisiness and an edge enhancement to define the boundaries were employed.

As these images were imported from a different system, precise measurements were not taken and the measurement markers were removed so they would not be included in the analysis. Area fractions were measured from five images. The AAF, SD, 95% CI, and RA were calculated from the results. Based on this estimate, the EBR-II plenum sample has approximately 0.11 ± 0.02 vol.% of carbides with 0.02 SD, an 0.02 CI at 95%, and an RA of 22%.

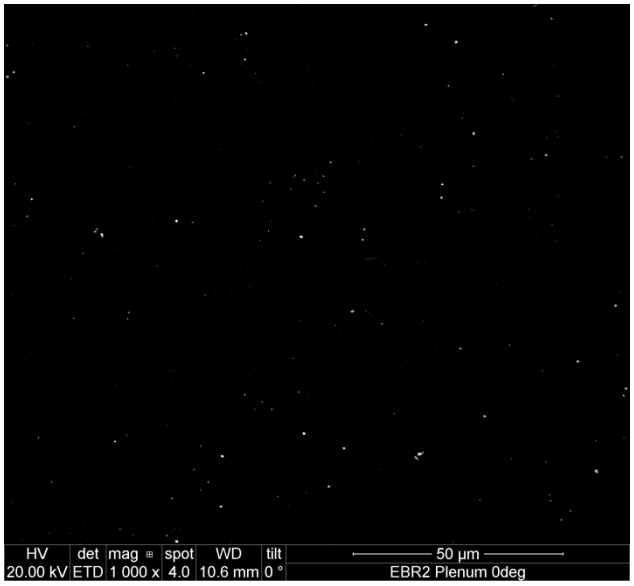

Figure 81. High-contrast BSE image of EBR-II plenum section showing the carbides as bright points.

6.3.3.3.1. Grain Size Estimate

The Beraha's etchant failed to bring out the grain boundaries distinctly enough to measure using any ASTM method. As an alternative, two EBSD scans were performed on different areas of the sample in the SEM. The EBSD reveals features of the crystallographic orientation of the material, and by careful examination of the pattern, it is possible to make a rough estimate of the grain sizes. Figure 82 shows an example of the image generated by the EBSD. These images were transferred to the AxioVision software, where the scale bar on the images was used to calibrate the measurements. As Figure 82 shows, each image was divided into thirds to cover the ID, OD, and CT. Each image was oriented such that the ID was the top of the image. From each section, a minimum of 20 measurements was taken. The longest perceivable diameter was measured when possible, but when uncertainty was present, preference was given to the more distinct grain boundaries. Once all measurements were taken, average grain sizes per section and total were calculated. Table 25 shows the results of this estimate. It should be noted that these measurements should be considered a rough estimate only. Proper measurement of grain sizes requires the grain boundaries to be clearly visible. Alternate etches attempted failed to reveal the grain boundaries. The average grain size was estimated at ~26 µm.

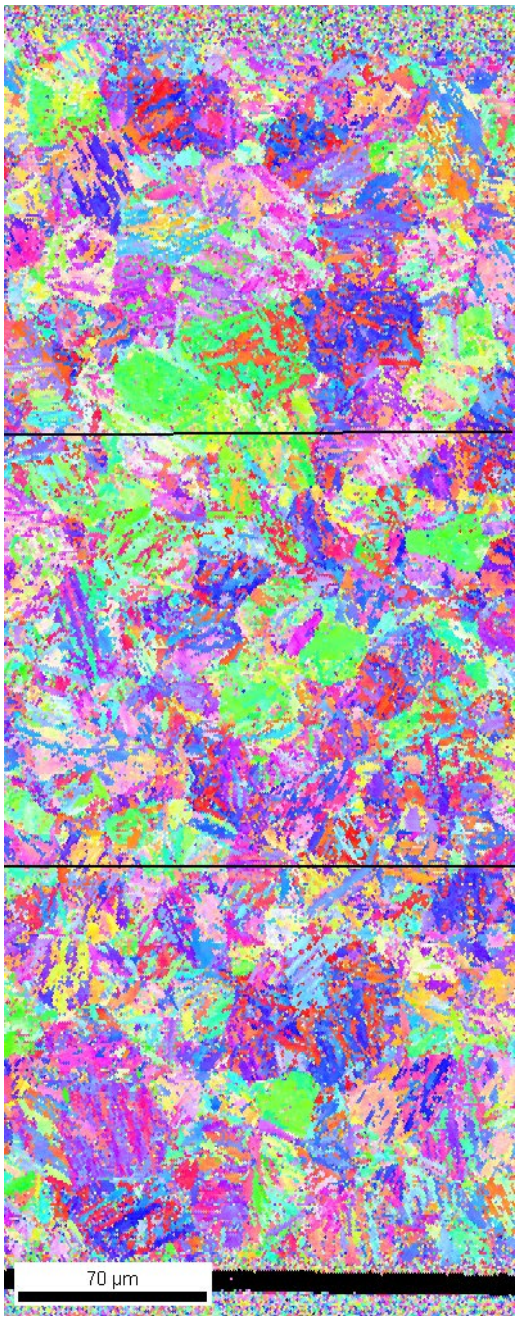

Figure 82. EBSD showing differences in crystallographic orientation. It is possible to roughly make out the grains of the material.

Table 25. Grain size estimates via EBSD for EBR-II plenum section.

Section	ID	CT	OD	Total
Average Size	29.0 µm	23.4 µm	25.3 µm	25.9 µm
SD	8.0	4.3	5.4	6.5
95% CI	2.4	1.3	1.7	1.1
% RA	8.4%	5.6%	6.6%	4.3%

6.3.3.3.2. Delta Ferrite Estimate

As mentioned previously, rounded phases were observed that may be delta ferrite. The Volume 9 ASTM handbook indicated that the electrolytic KOH etch would stain delta ferrite. The optical microscope shows some potentially stained areas, but they were too small to clearly see with the 20× objective. Due to the small size of the sample mounts relative to the microscope, the higher magnification objectives could not be used. When viewed at higher magnifications in the SEM, this etch did bring out both the potential delta ferrite phases as well as the carbides. This etch also revealed that the carbides observed previously were only a small fraction of those present. There were numerous other small carbides throughout the sample. The five images taken of random areas of the sample at 1,000× magnification were used to estimate delta ferrite, while the five images at 5,000× magnification were used to re-estimate carbide content.

The contrast on the SEM was adjusted such that the carbides appeared black, while the rest of the steel was light gray to make it easy for the AxioVision software to perform image analysis. Figure 83 shows an example of the high-magnification images of the carbides. Because the potential delta ferrite phases were the same color as the martensitic areas of the steel, each of ferrite phases identified in the 1,000× images was shaded red using Adobe Photoshop. This created a color contrast for the AxioVision software to work with. Figure 84 shows an example image altered in this manner. The only image enhancement performed for the analyses was a sigma filter of 32 and an edge enhancement with a threshold of 25 and size of 3. The results of the estimate are presented in Table 26. It was estimated that the volume fraction of delta ferrite was 0.30% ± 0.11%. Due to the uncertainty in the RA, the confidence this estimate is correct is low. At higher magnifications, the carbides were estimated to be 5.8 vol% ± 2.5%. This is much higher than the previous estimate and suggests that there are numerous small carbides present in the martensitic structure.

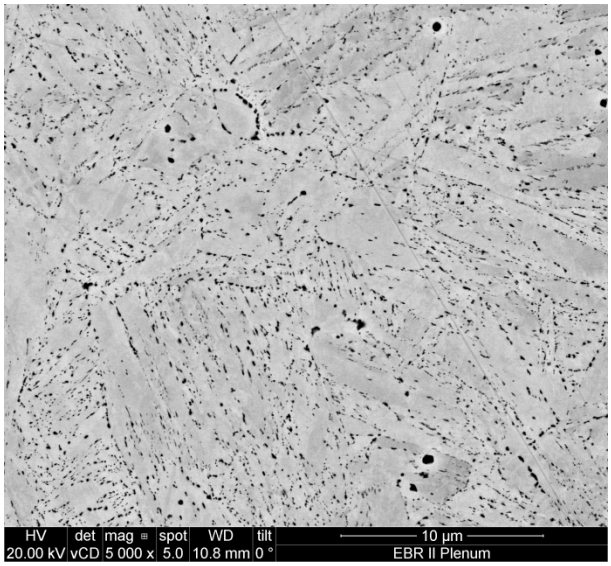

Figure 83. High-magnification image of carbides revealed by electrolytic KOH etch.

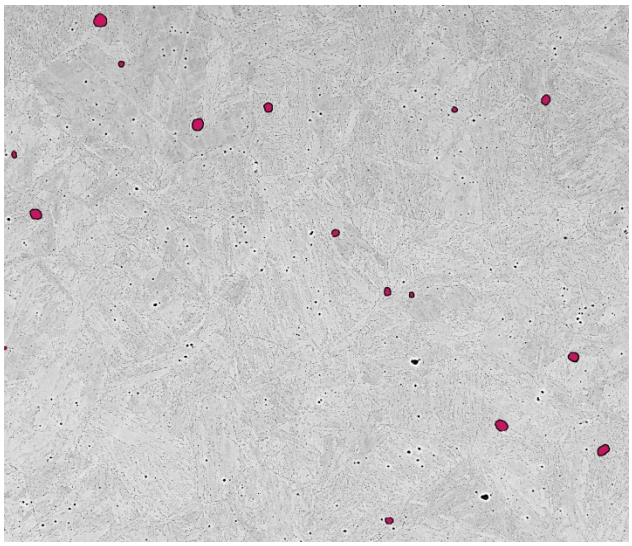

Figure 84. SEM image with delta ferrite phases marked in red.

Table 26. Delta ferrite and high-magnification carbide estimates for EBR-II plenum section.

Phase	Delta Ferrite	Carbides
AAF	0.30%	5.8%
SD	0.09	0.20
95% CI	0.11	2.5
% RA	36%	4%

7. WELD CHARACTERIZATION

7.1. Microstructure

7.1.1. Sample Preparation

Two weld samples were evaluated for microstructure: bisecting cuts from the top end weld and the spade end weld. These samples were sectioned from the fuel element after the fuel and Na bond was removed. They were then mounted in epo-heat epoxy and polished to a finish of 0.04 µm with colloidal silica. Beraha's reagent, a tint etchant, was used as an etchant to resolve features and make clear distinctions between ferrite and martensite. Each of the samples showed some pitting from this procedure. These samples were pitted enough from the original etching that an additional treatment was necessary to remove the pitting. These samples were re-polished to 0.03 µm with an alumina suspension and re-etched with a modified Beraha's reagent.

7.1.2. Optical Microscopy Procedure

Prior to beginning the examination of the samples, the Zeiss Axio Observer.Z1m microscope was calibrated using a National Institute of Standard and Technology Standard Reference Material 2800 Microscope Magnification Standard in accordance with ASTM Standard E 1951-02 Standard Guide for Calibrating Reticles and Light Microscope Magnifications. The entirety of the sample was examined looking for unusual phases or areas using the 5× objective and then the 10× objective. Polarized light was used as the contrast it creates enables the easy identification of ferrite grains or other potential phases. Images were taken using an AxioCam MRc5 digital camera controlled by the AxioVision software version 4.8. The area containing the plug and weld was imaged in a mosaic using polarized light using the 10× objective lens and the MosaiX Acquisition module for the AxioVision software. The mosaic consisted of a 7×7 matrix stitched together using the AxioVision software. A weight was used to hold the sample in position and

limit shifting during acquisition. The direction for which the labeling inscribed on the back of the sample was upright was designated as 0°. The upper area in this direction was designated 0°, while the lower area was designated 180°. Images of the weld at both 0° and 180° were taken in both bright field and polarized light using the 5× objective lens. The HAZ in both the tube and the plug were imaged using both the 5× and 10× objective lenses in bright field and polarized light. Some distance away from the weld, representative pictures were taken of the tube wall and plug using first the 10× and then 20× objective lens in both bright field and polarized light.

7.1.3. Top End Weld

Figure 85 makes it apparent that the weld in this sample was placed as a "cap" over the tube and plug. The heat source was applied to the head of the plug causing it to melt and fuse with the tube. It then recrystallized into the coarse microstructure seen in Figure 86. The microstructure in the bulk of the weld is coarser (last to solidify) than the material closer to the weld boundary. There is an unetched area in the 0° direction (top of the image) near where the plug and tube connect. The majority of the tube material away from the plug appears to be a tempered lath martensite perhaps over-tempered near the weld. The plug and tube microstructure are contrasted in Figure 87 and Figure 88. Compared to the tube, the structure of the lath martensite in the plug is not quite as defined and has a gray appearance. Its coarser appearance indicates the prior austenite grain size may have been larger. The end plugs were machined from 1/4 or 3/8 inch rod stock that was drawn and heat treated from the original billet material. The tubing had gone through more drawing operations with intermittent and final heat treatments. It would be expected that the tubing heat treatments would be more closely controlled as the tubing forms the barrier to fuel pin breach. Further away from the weld, the microstructure in the plug and the tubes appears to be quenched lath martensite consistent with what is observed in un-welded samples.

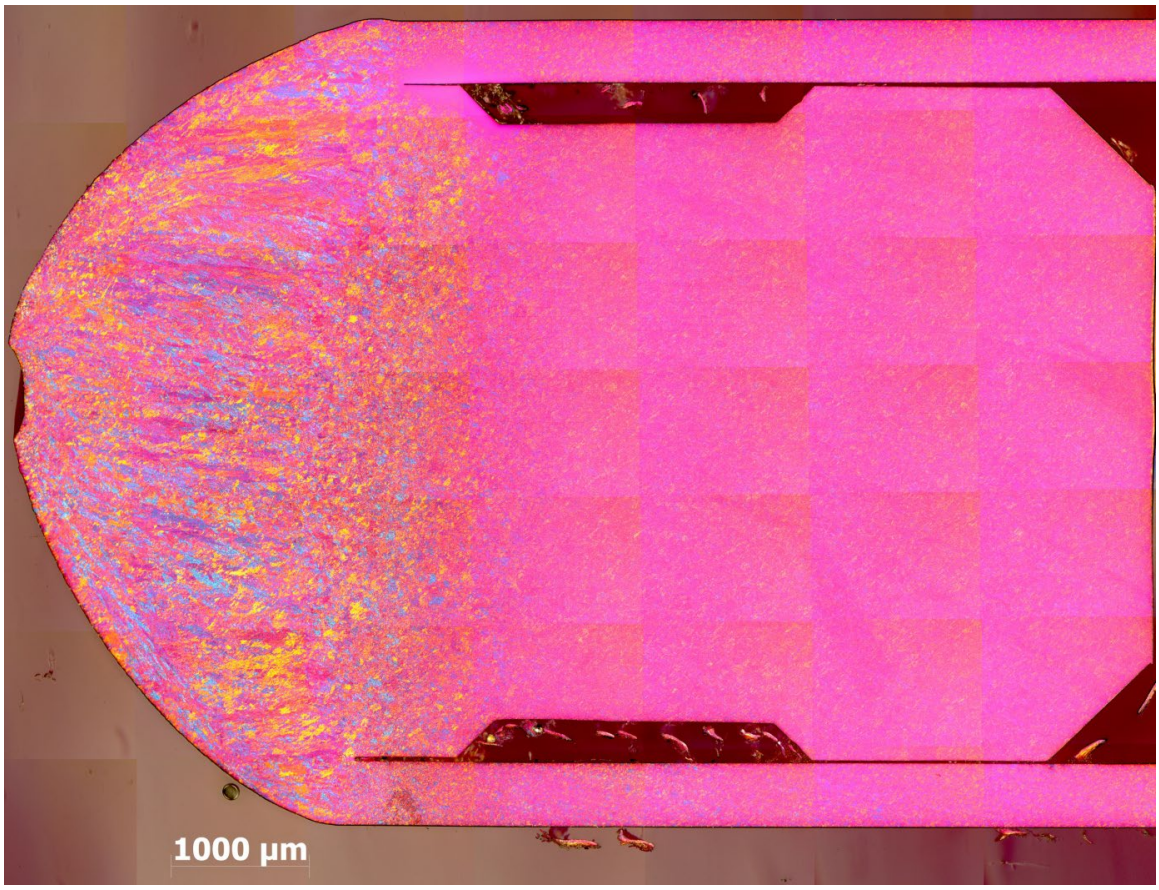

Figure 85. Mosaic of the weld and plug of the top end weld.

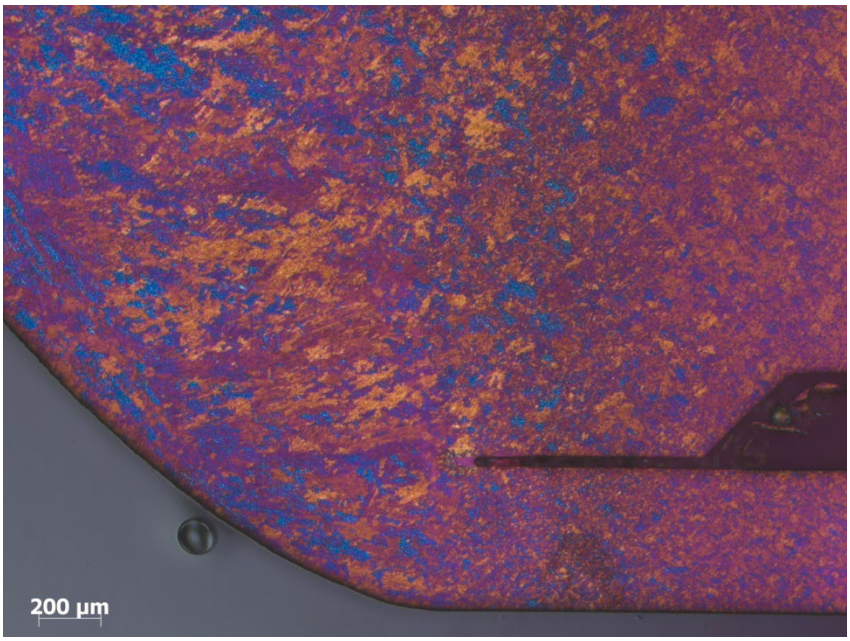

Figure 86. 180° weld boundary under polarized light.

Figure 87. Area in 180° direction. Plug (top) shows gray tempered martensite while tube shows a different coloration as the initial as-drawn material or the temper conditions may have been different.

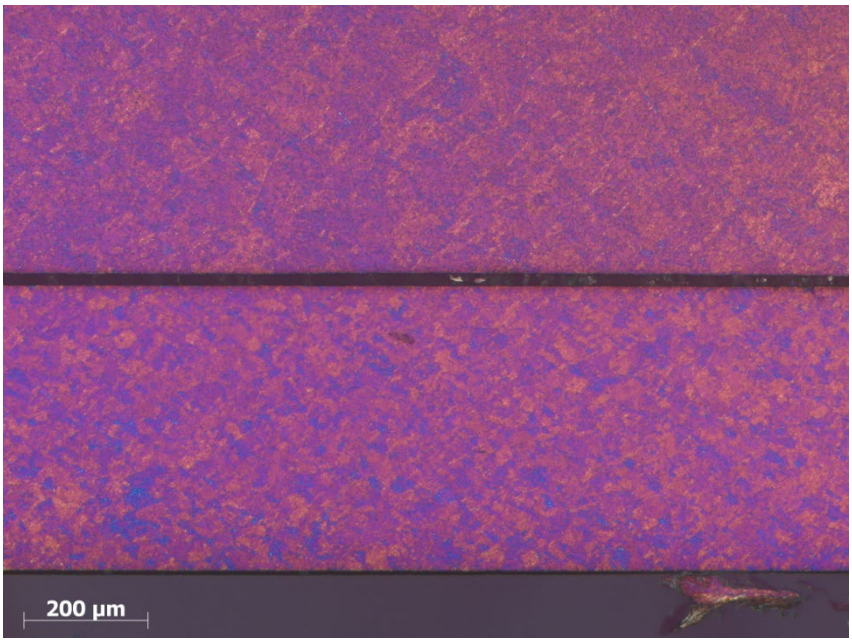

Figure 88. Area in 180° direction showing the tempered plug (top) and the tube (bottom) martensite under polarized light.

The images of the area where the weld meets the tube taken at 50× using bright field light were used to estimate the HAZ. Images were taken at both the 0° wall, center of the plug, and the 180° wall. Measurements were taken on each image using the AxioVision software. The main priority was obtaining five measurements of the length from where the weld ended to the point where the tube reverted to the original tempered lath martensite seen in un-welded samples. Figure 89 shows one of the images used to make these measurements. As this is not a definite border there is some uncertainty involved in the measurement. Table 27 presents the results obtained. Comparison of the two sets of measurements using the student t-test revealed they are significantly different with greater than 99% confidence. Why the 0° wall has a more extensive HAZ is unknown.

Figure 89. Measurement of the HAZ at the 0° wall.

Table 27. Measurement of HAZ on top end weld.

Wall	0°	180°
Average Measurement	1310 µm	1130 µm
SD	22	34
95% CI	27	42
RA %	2%	4%

7.1.4. Spade End Weld

The locations where the tube was welded to the plug are apparent in Figure 90. The heat source (arc using tungsten electrode) was rotated around the tube and end plug interface, the electrode perpendicular to the tube wall. The tube wall and part of the end plug are melted, and the joint is made. The molten material solidified and then recrystallized into the coarse microstructure seen in Figure 91. The majority of the material appears to be a lath martensite, but the heat from the weld had an influence. The material in the plug and tube closest to the weld appears to have a coarser microstructure, perhaps due to grain growth as the material was heated. As seen in Figure 92, the structure of the lath martensite is not quite as well defined, and the microstructure has a gray appearance. Further away from the weld, the microstructure is the as-received tempered lath martensite. Figure 93 and Figure 94 provide examples of this microstructure as observed in both bright field and polarized light. Again, the plug material appears to have a coarser prior austenite grain structure.

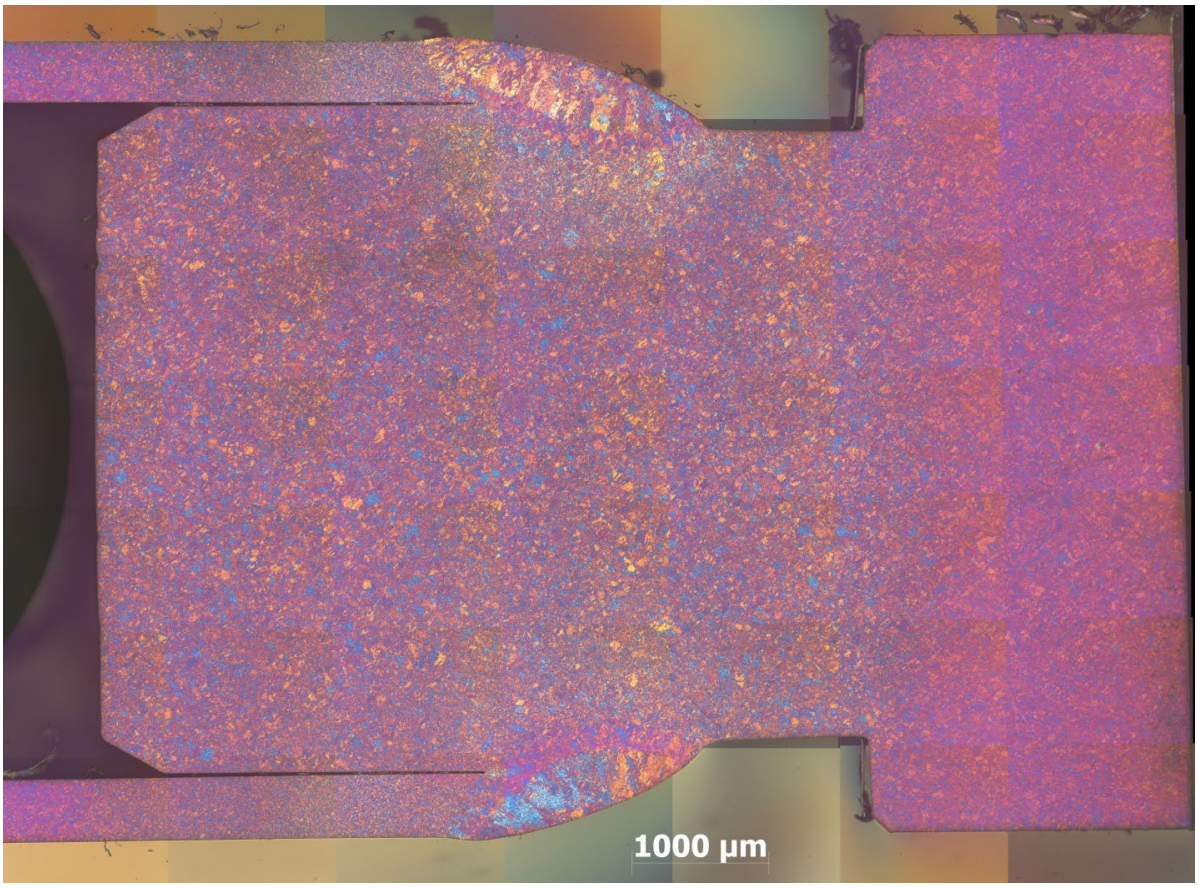

Figure 90. Mosaic of weld and plug of the spade end weld.

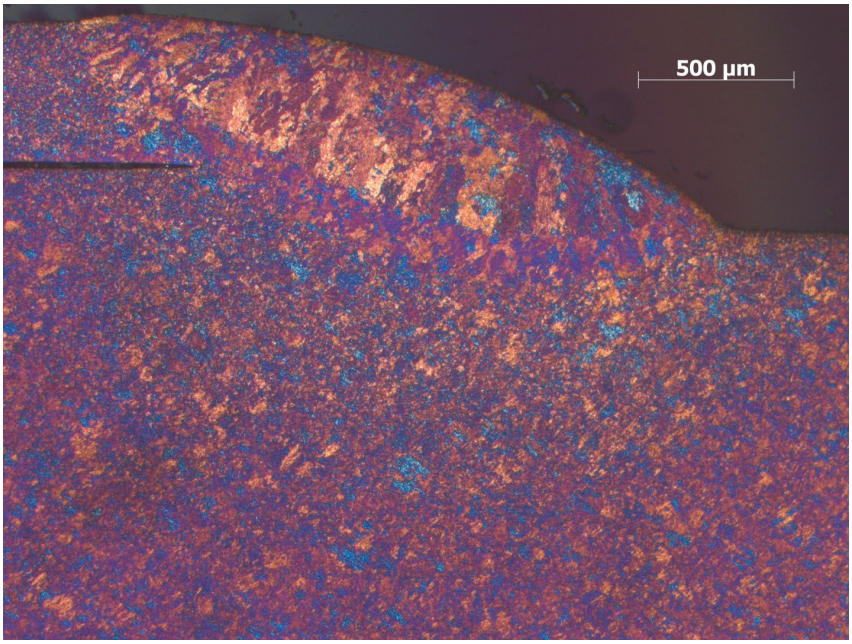

Figure 91. Weld at 0° viewed under polarized light.

Figure 92. 180° weld showing gray tempered microstructure.

Figure 93. 0° in bright field showing lath martensite consistent with un-welded samples.

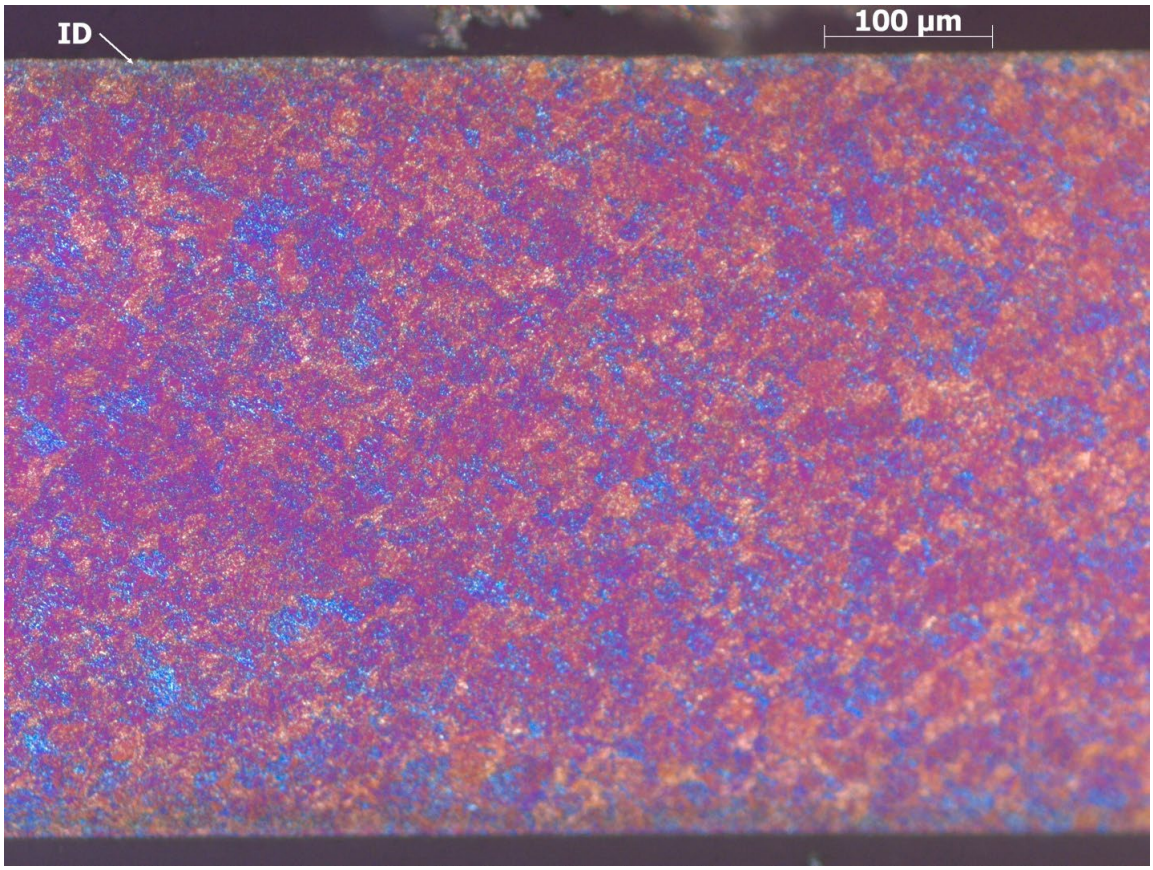

Figure 94. 180° tube in polarized light showing lath martensite structure.

The images of the area where the weld meets the tube taken at 50× using polarized light were used to estimate the HAZ. For this sample, polarized images were most suited to performing the estimate. Images were taken at both the 0° wall and the 180° wall. Five measurements were taken on each image using the AxioVision software. The measured length was the distance from where the weld ended to the point where the tube microstructure reverted back to the fine, tempered lath martensite as seen in unwelded samples. Figure 95 shows one of the images used to make these measurements. As this is not a definite border, there is some uncertainty involved in the measurement. Table 28 presents the results obtained. Comparison of the two sets of measurements using the t-test revealed they are significantly different with greater than 99% confidence. The 0° wall has a slightly more extensive HAZ, not unusual as the electrode rotates around the tube and plug to overlap, so more heat may have been applied to the overlapped portion of the circumference.

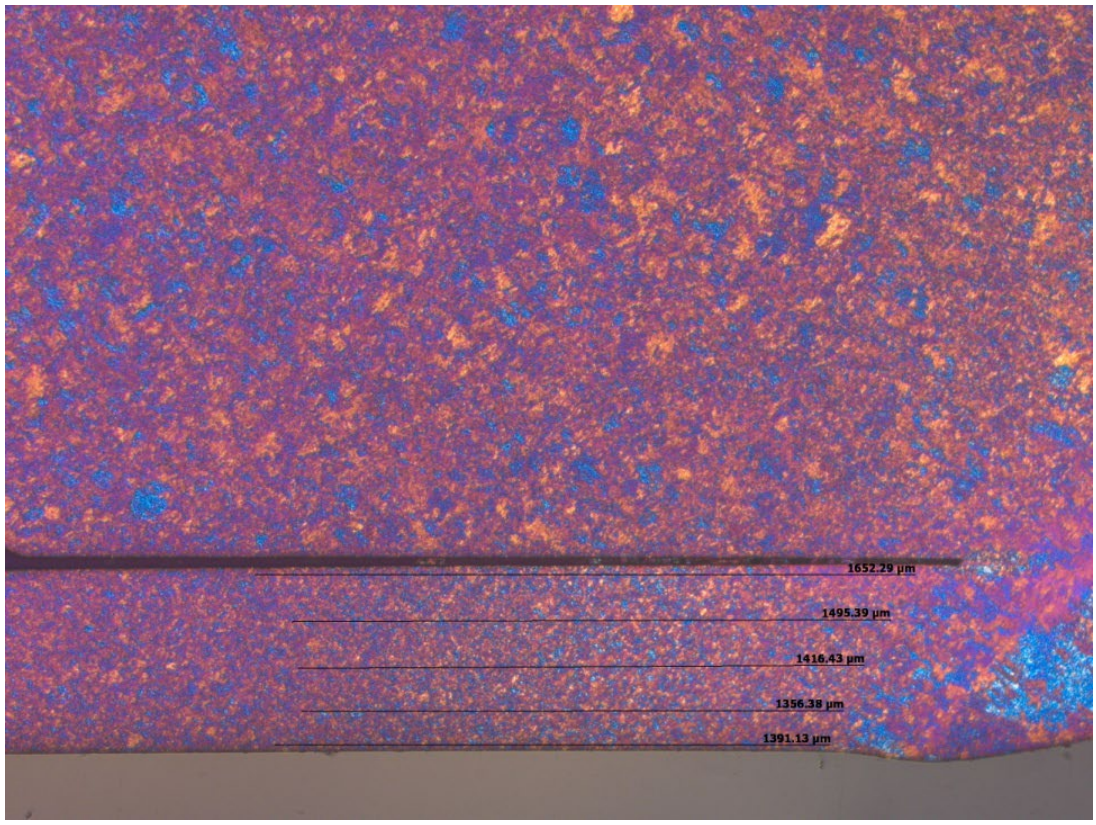

Figure 95. Measurement of the HAZ at the 180° wall.

Table 28. Measurement of HAZ of the spade end weld.

Wall	0°	180°
Average Measurement	2240 µm	1460 µm
SD	29	118
95% CI	36	146
RA %	2%	10%

7.2. Microhardness

7.2.1. Top End Weld

A series of Vicker's hardness tests using a 100 g load were performed using a LECO M-400-H1 hardness tester at spots over the plug, across the weld, and out into the HAZ. This data is presented in Table 29. The first data point begins in the plug; the last is within the tube past the plug and into the martensitic microstructure typical of the as-received tubing material. In addition to Table 29, a mosaic of the hardness tests with data attached is presented in Figure 96. The mosaic was created using the MosaiX Acquisition module for the AxioVision software version. Images were taken under polarized light using the 10× objective lens and consisted of eight columns with two rows and was stitched together using the AxioVision software. As can be seen in Figure 96, hardness is greatest in the weld material and initial part of HAZ, decreasing somewhat in the HAZ, and lowest in the base tube material. It is highest at the end plug and at the weld boundary. Much of the carbon would be redissolved in the molten weld material or hottest part of the HAZ, and as it cooled quickly, hard, untempered martensite resulted.

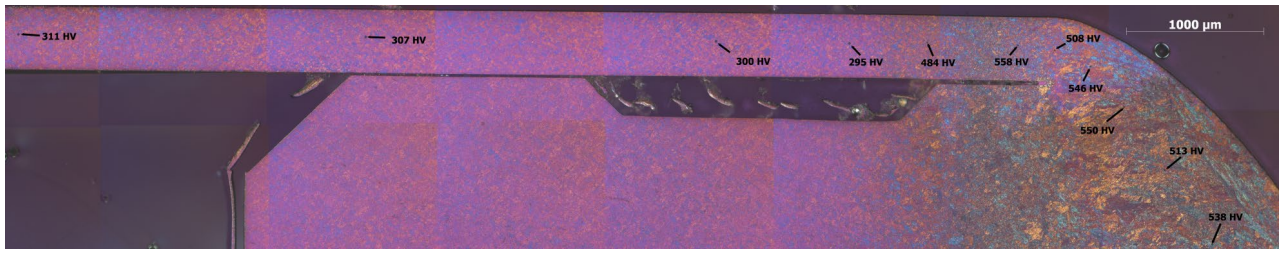

Figure 96. Mosaic of HAZ with hardness measurements of top end weld.

7.2.2. Spade End Weld

A series of Vicker's hardness tests using a 100 g load were performed using a LECO M-400-H1 hardness tester at spots over the plug, across the weld, and out into the HAZ. This data is presented in Table 29. The first data point begins in the plug; the last is within the tube past the plug and into the more typical martensitic microstructure. In addition to Table 29, a mosaic of the hardness tests with data attached is presented in Figure 97. The mosaic was created using the MosaiX Acquisition module for the AxioVision software version. Images were taken under polarized light using the 10× objective lens and consisted of nine columns with two rows and was stitched together using the AxioVision software. As can be seen in Figure 97, hardness is greater in the HAZ and reaches a peak in the weld. The martensite present in the weld may be harder due to the rapid cooling.

Table 29. Hardness measurements on HAZ in weld areas of EBR-II fuel element.

Top End Weld		Spade End Weld	
Point number	Hardness	Point number	Hardness
1	538	1	300
2	513	2	380
3	550	3	441
4	546	4	502
5	508	5	506
6	558	6	490
7	484	7	527
8	295	8	531
9	300	9	522
10	307	10	526
11	311	11	529
—	—	12	493
—	—	13	487
—	—	14	486
—	—	15	342
—	—	16	303

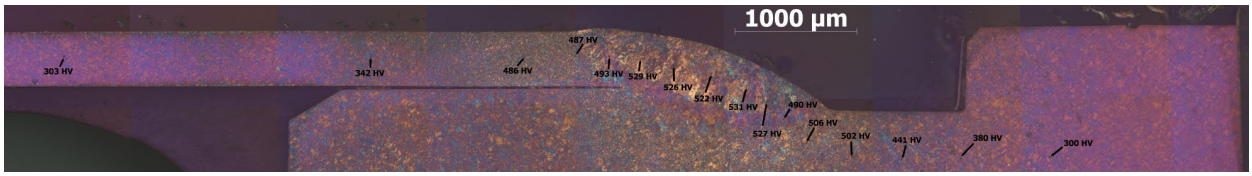

Figure 97. Mosaic of HAZ with hardness measurements of spade end weld.

8. DISCUSSION

The discussion here relates primarily to the fuel slug and the differences exhibited between sample Ra and the other two, Rb and Rc. Analysis of the EBR-II fuel rod suggests that this rod exhibits varying degrees of homogeneity that is likely a function of the injection casting and rapid cooling of the rod.

Sample Ra shows greater U and Zr variation along its radial traverses than do samples Rb and Rc, likely as a result of the large number of secondary phases present along the traverse path. In addition, sample Ra contains larger euhedral crystals, while samples Rb and Rc contain subhedral to anhedral crystals, most of which are considerably smaller than those in Rb and Rc. Sample Ra has a large and chemically complex outer rind, while Rb and Rc have virtually no rind. Finally, on average, U concentration is higher is Ra and lower in Rc, while the reverse is true for Zr.

These observations suggest a complex casting and cooling history that can account for these features.

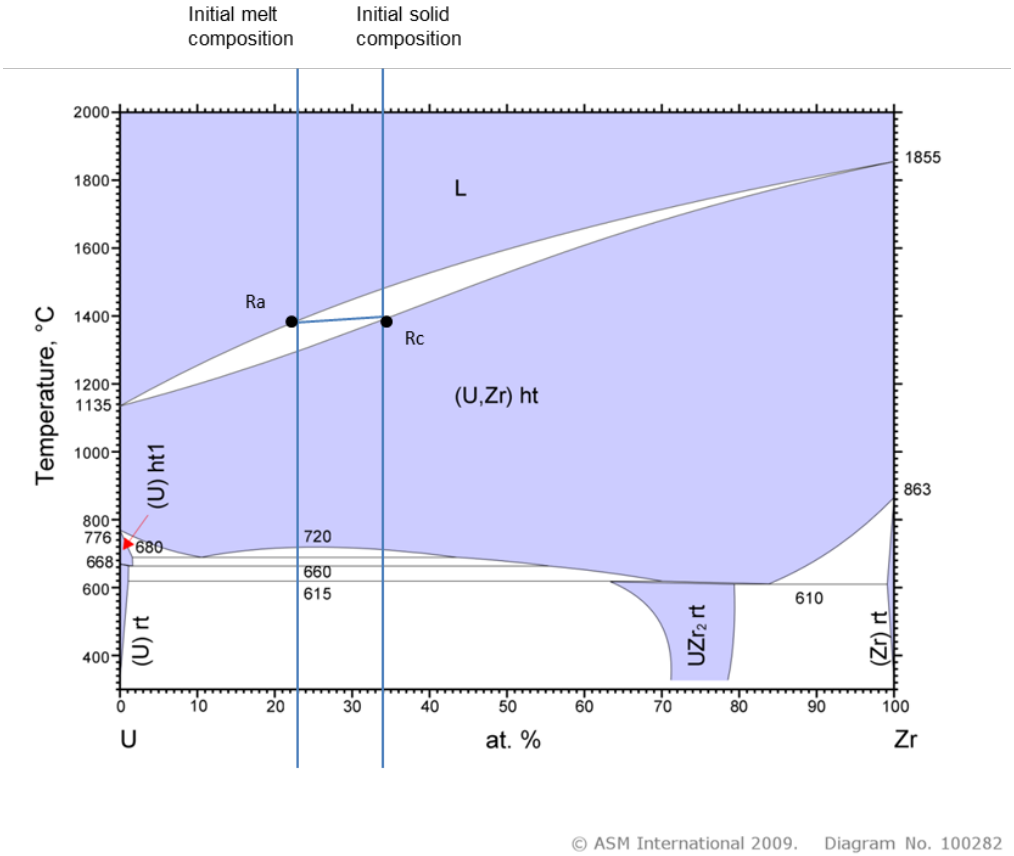

Figure 98. Binary U-Zr phase diagram (Kurata, 1998) showing initial melt and solid compositions for EBR-II cast fuel rod.

If we momentarily assume that the system under discussion is binary (U-Zr), Figure 98 shows the initial melt composition at 77 at% U. The first solid to precipitate will have a uranium composition of 66 at%, which is very close

to the observed average U content of sample Rc (longitudinal) at 65.3 at%. Continued cooling will result in solids that are relatively enriched in U relative to the initial precipitate, which is confirmed by the average U content of Ra (longitudinal) at 69.7 at%. Given the fact that the injection occurs in less than 1 second but that the mold is left in the crucible for additional time to allow sufficient solidification to prevent dripping (Wilkes et al., 1987), it is likely that the melt at the top of the mold solidified far more quickly than the melt in the bottom, which remains in contact with the crucible.

Additional lines of evidence supporting this hypothesis include the phase size and morphology. Phases in sample Rc tend to consist of anhedral crystals of ZrC that often contain what appear to be bubbles or nearly pure uranium melt inclusions. Small crystals (in this case, generally <5 μm) tend to result from rapid cooling, as would be expected at the top of the mold.

In contrast, sample Ra exhibits large euhedral crystals and crystals with complex inclusion and overgrowth structures and chemistry. The origin of phases such as the euhedral Zr_2Si is uncertain; however, the practice of incorporating the heel of previous castings into the melt suggests a possible mechanism. The heel contains material that has had time to react somewhat with the molds immersed into it. It would contain some Si. In fact, remelt was often limited (50-60%) because of contamination.

Finally, sample Ra has an extensive and complex rind, the outer portion of which consists of ZrSi. This suggests extensive interaction with the mold at temperatures high enough to permit sufficient diffusion of Si into the melt material or interaction with the zirconia wash. This type of mechanism is more likely to occur at the bottom of the mold where cooling rates were slower and where the mold was kept in contact with the melt and crucible until solidification was complete.

8.1. Zr_xC Phases

An abundance of apparent phases with the approximate composition Zr_5C exists, particularly in sample Ra. It comprises the inner rim region and exists as overgrowths around ZrC (Figure 49, Table 18, Spots 747, 758, 761). If the small amount of uranium present is ignored, the apparent phase can be understood by considering the Zr-C binary phase diagram (Figure 99), which shows the compositional region describing this apparent phase. The diagram suggests that this apparent phase is actually a mixture of two phases, Zr and ZrC, with approximate proportions of 55:45.

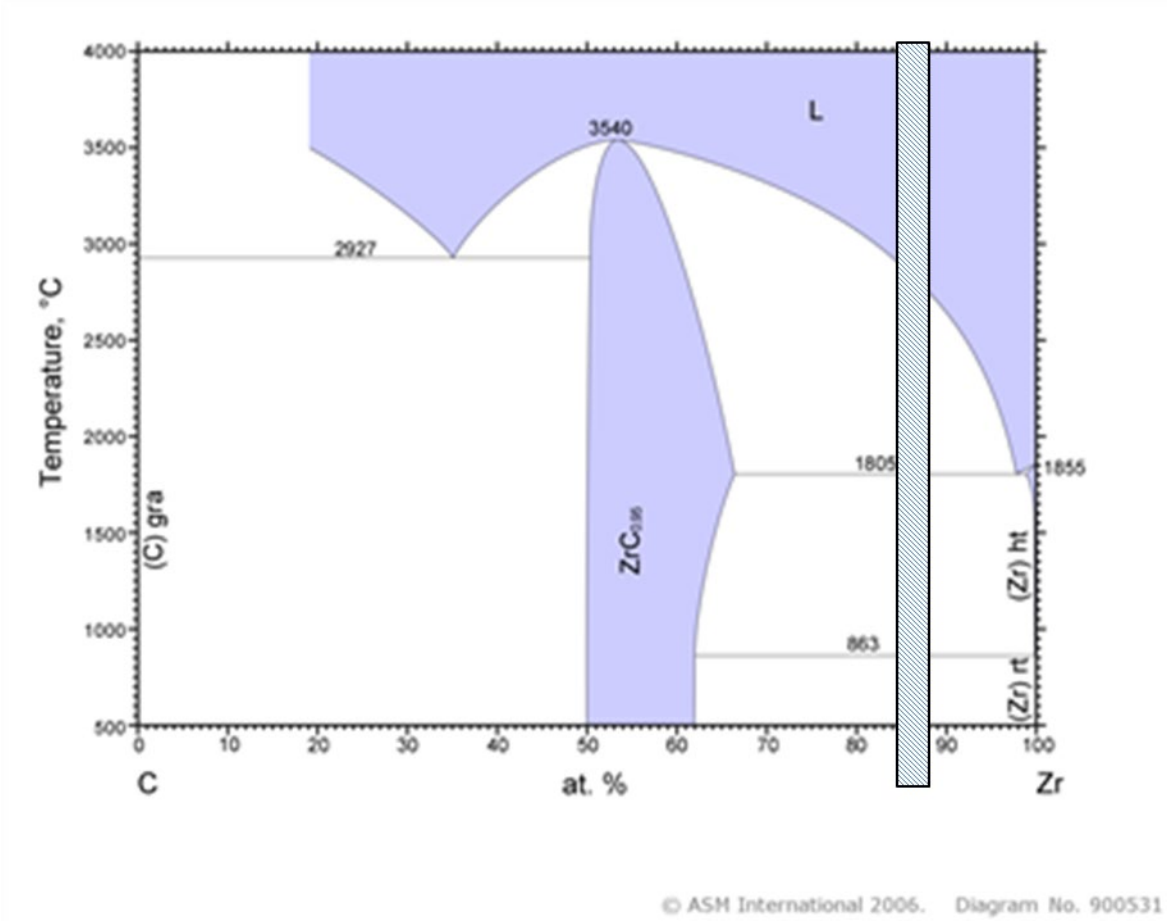

Figure 99. Zr-C phase diagram (Okamoto, 1990) showing compositional region (stippled) of Zr_xC phases found in the rim region and as overgrowths around ZrC.

The extensive zirconium-rich rim development and large size of high-zirconium inclusions present in Ra and likely facilitated by interaction with silicon and carbon suggests that this end of the rod could exhibit more, or less interactions with cladding, if operating conditions were axially homogenous. Excess silicon and carbon decreases zirconium solubility, resulting in the precipitation of Zr-C and Zr-Si phases. These in turn remove Zr from the solid solution, which lowers the melting temperature and increases fuel cladding chemical interactions (Burkes et al., 2009). The fuel specifications limited the amount of Si, O, C, and N impurities for this reason. Conversely, the resultant 'rim' may decrease interaction.

Note again, that the ends of the cast and sheared fuel slugs are not marked as to which end was closest to the melt, so it is these features that lead us to believe that Ra was closest to the melt and therefore solidified less quickly. Other elements may have had the Ra characteristics in the upper end of the element.

9. CONCLUSIONS

Both chemical concentrations and phase assemblies vary with distance from the spade, which is a likely consequence of the casting and cooling process of the fuel slug. A temperature gradient of up to 780°C exists along the length of the casting mold. This results in chemical zonation consistent with the U-Zr binary phases diagram. Incorporation of portions of heels may also contribute to insoluble Zr-rich phases at the crucible end of the cast rod. The measurement of carbon and silicon in each casting help to minimize that effect and lower waste. Long residence times in the crucible likely allow the interaction of melt with the silica (quartz) mold, creating a rind in that region of the cast rod.

10. REFERENCES

Burkes, D. E., R. D. Fielding, D. L. Porter, D. C. Crawford, and M. K. Meyer, 2009, "A US perspective on fast reactor fuel fabrication technology and experience part I: metal fuels and assembly design," Journal of Nuclear Materials (389): 458–469

Chantler, C. T., K. Olsen, R. A. Dragoset, J. Chang, A. R. Kishore, S. A. Kotochigova, and D. S. Zucker, 2005, "X-Ray Form Factor, Attenuation and Scattering Tables" (version 2.1). [Online] Available: http://physics.nist.gov/ffast [Thursday, 07-Feb-2013 13:36:10 EST]. National Institute of Standards and Technology, Gaithersburg, MD.

Kurata, M., T. Ogata, K. Nakamura, and T. Ogawa, 1998, "Thermodynamic assessment of the Fe-U, U-Zr and Fe-U-Zr systems, ASM Alloy Phase Diagrams Center," P. Villars, editor-in-chief; H. Okamoto and K. Cenzual, section editors;
http://www1.asminternational.org/AsmEnterprise/APD, ASM International, Materials Park, OH, USA, 2006–2013

Love, G. and V. D. Scott, 1078, "Evaluation of a new correction procedure for quantitative electron-probe microanalysis," Journal of Physics D-Applied Physics, 11(10): 1369–1376

Okamoto, H. 1990, "Binary Alloy Phase Diagrams," ASM Alloy Phase Diagrams Center, P. Villars, editor-in-chief; H. Okamoto and K. Cenzual, section editors;
http://www1.asminternational.org/AsmEnterprise/APD, ASM International, Materials Park, OH, USA, 2006–2013

Rough, Frank, 1955, "An Evaluation of Data on Zirconium-Uranium Alloys", Battelle Memorial Institute.

Sturcken, E. F., Walter, C.M., (1974), "Texture and Irradiation Growth in EBR-II Driver Fuel," Journal of Nuclear Materials (50): 69–82

Wilkes, C. W., G. L. Batte, D. B. Tracy, and V. Griffiths, 1987, "EBR-II Fuel Slug Casting Experience, Argonne National Laboratory," ANL-IFR-73.